Master's thesis

NTNU
Norwegian University of Science and Technology
Faculty of Natural Sciences
Department of Physics

Johan Magnus Krosby

Design and Construction of Mueller Matrix Scatterometer for Use in Metasurface Characterisation

Master's thesis in Physics
Supervisor: Morten Kildemo
June 2022

NTNU
Norwegian University of
Science and Technology

Johan Magnus Krosby

Design and Construction of Mueller Matrix Scatterometer for Use in Metasurface Characterisation

Master's thesis in Physics
Supervisor: Morten Kildemo
June 2022

Norwegian University of Science and Technology
Faculty of Natural Sciences
Department of Physics

NTNU
Norwegian University of
Science and Technology

Acknowledgements

I would like to thank my supervisor Morten Kildemo for giving me the opportunity to partake in this challenging but rewarding project, as well as supporting and giving advice where needed.

Furthermore I would like to thank Per Magnus Walmsnes who was there to answer my every question, no matter how stupid, despite being pressed for time himself, as well as making the general plan and blueprints for the project.

I would also like to thank the department engineer Vedran Furtula, who has provided me with a lot of help during the instrumentation parts of the projects as well as providing technical expertise whenever needed.

Lastly, I would like to thank everybody else that has been there to support me during the writing of this thesis, be it for discussions on the topic or more general support. Chief among these is my girlfriend and companion Elisabeth Savitri Thrane providing ample support on the days when the project seemed endlessly daunting and unachievable. Furthermore, a special thanks has to be extended to well as my dear friends Daniel Huseby Solheim, Celiné Angonin and Victoria Bjelland for generously giving me continual feedback on the thesis as it was written.

Abstract

The construction of a complete Mueller matrix scatterometer is presented in this thesis. A supercontinuum laser source was utilized in combination with acusto-optical filters as a source of illumination. Several aspects of the source have been explored, including its spectral range, stability, and spectral power density. Two methods for measuring the transmittance of a sample are presented, tested and discussed. A dual rotating retarder Mueller matrix ellipsometer was constructed based on the findings in these tests. Two calibration for the ellipsometer methods were tested to ensure an optimal result. The ellipsometer displayed good results for a wavelength range of 440 to 660 nm and 670 to 1060 nmwith a deviation from the expected values in the Mueller matrix elements of less than 1%. The gap in the spectrum was due to the design of the wavelength selection mechanism of the source. Finally, the ellipsometer was then attached to the scatterometer and tested by measuring a beam splitting polarizer.

Sammendrag

Konstruksjonen av et komplett Mueller matrise scatterometer er presentert i denne avhandlingen. Til dette formålet har en supercontinuum laserkilde i kombinasjon med akusto-optiske filetere blitt brukt som en strålingskilde. Ulike aspekter ved denne kilden har blitt utforsket, inkludert den spektrale rekkevidden, stabiliteten så vel som den spektrale effekttettheten. To metoder for å måle transmisjon gjennom en prøve er testet og diskutert. Basert på funnene under disse testene ble et Mueller-matrise ellipsometer konstruert. For å forsikre gunstige resultater ble to kalibreringsmetoder utforsket for ellipsometeret. Ellipsometeret viste gode resultater for bølgelengder i spennet 440 til 660 nm og 670 til 1060 nm med avvik fra forventede verdier i Mueller matrise elementene på mindre enn 1%. Hullet i spekteret var en uunngåelig konsekvens av til bølgelengdeselleksjonsmekanismen. Scatterometeret var så bygd for så å bli testet ved å måle en strålesplittende polarisator.

Contents

Part I:

Introduction and Theory

Section 1:

Introduction

The phenomenon of light has been the subject of much discussion and pondering since the dawn of civilisation, and likely before that. The earliest known theories of light were concurrently described in ancient Greece and India[1, 2]. Even though several of these theories came surprisingly close to the modern understanding of electromagnetic (EM) radiation, it was not until 1669 when Erasmus Bartholinus by accident observed double refraction in calcite crystals that one of the most central aspects of light was discovered, polarization[3]. Polarization has since been identified to be present in many phenomena, e.g. in rainbows[4], in the reflections of shells of certain beetles[5], and in the blue light in the sky[6]. This knowledge has also been used for practical purposes and everyday applications, e.g. in polaroid sunglasses which are used to reduce glare from water puddles when driving.

The revelation that light is an electromagnetic wave did, however, not occur until the 19th century, when Michal Faraday discovered in 1845 that linearly polarized light may be rotated when propagating through a transparent dielectric with an external magnetic field[7]. This later inspired James Clerk Maxwell, who went on to create his, now well known, framework for EM-waves[8].

With the stage now set with a fundamental theory for EM-waves, the field of optics exploded. In the late 1880s to early 1890s Paul Drude took special interest in the polarization changes occurring due to reflection from plane surfaces[9]. These investigations lead to the first description of what is now called an ellipsometer. These devices turned out to be quite useful, not only for determining the change of polarization, but also for an easy and relatively cheap way to characterize materials made from deposits of thin films, which have become more and more popular in recent years[10].

The connection between light and electromagnetism has also in recent times opened the door for exploration of more complex interactions between EM-waves and materials beyond the more traditional optical materials like lenses, retarders, and diattenuators. This has paved the way for metamaterials, a new generation of optical components. Metamaterials have a broad array of meanings, depending upon who is asked. One useful definition provided by Shivola is that a metamaterial is a structure with more than one constituent, whose electric and optical properties are not found in nature or in the individual constituents[11]. Reducing the thickness of these materials to that of the wavelength of an incoming EM-wave results in a metasurface. These are capable of inducing changes of the incoming wavefront despite being several orders of magnitude smaller than traditional optical components[12].

In recent years, optical metasurfaces have become more and more interesting, as designs keep evolving and improving. Due to the metasurfaces potential for customization as well as their small size, it has become more and more clear that they may be capable of competing with traditional optical components[13].

Many metasurfaces work on the basis of scattering at specific angles[12]. As is pointed out by Boren and Huffman, the scattering of light implies changes in polarization[14]. To measure these changes in polarization, an ellipsometer that works for several angles is necessary. Such an instrument is called a Mueller matrix scatterometer and the construction of such a device has been the goal of this thesis.

In section 2 the necessary theory to understand the physics and the mathematics of the Mueller matrix scatterometer is presented. This includes a rudimentary theory of polarization, and how to express this with both the Stokes and Jones formalism. Furthermore, other general theory and mathematics that has been utilized as a part of the thesis has also been provided. The function of several common

optical components have also been explained.

Part II and subsequently section 3 describes the components, hardware and software used in the thesis. An overlook of the practical work done in the thesis is provided in section 4.

Part III contains the results in addition to a discussion of these. This part is split into three sections, each one describing and discussing the results from various tests done in the run-up to, and construction of, the ellipsometer. Section 5 describes the various tests of the source of the scatterometer, while section 6 describes the testing of different measurement techniques and how these tests worked with the pulsed source that was used. For the final results concerning the instrument as a whole, section 7 explores the various strengths and weaknesses of the final product. Finally, Part IV contains the conclusion and the final statements of the thesis

Section 2:

Theory

2.1 Polarized Light

The nature of electromagnetic waves is described classically by Maxwell's equations in differential form as[15]

$$\begin{aligned} \boldsymbol{\nabla} \cdot \vec{E} &= \frac{1}{\epsilon_0}\rho, & \boldsymbol{\nabla} \cdot \vec{B} &= 0, \\ \boldsymbol{\nabla} \times \vec{E} &= -\frac{\partial}{\partial \vec{B} t}, & \boldsymbol{\nabla} \times \vec{B} &= \mu_0 \vec{J} + \mu_0 \epsilon_0 \frac{\partial \vec{E}}{\partial t}. \end{aligned} \tag{2.1}$$

Solving these equations with respect to $\vec{E}$ is possible by eliminating the $\vec{B}$-field by substitution. Assuming a plane wave propagating in the $\hat{z}$-direction, the total field is found to be on the form

$$\vec{E} = \mathfrak{Re}\left\{ E_{0X} \mathrm{e}^{i(\omega t - kz + \delta_x)} \hat{x} + E_{0Y} \mathrm{e}^{i(\omega t - kz + \delta_y)} \hat{y} \right\}, \tag{2.2}$$

as $\vec{E}_z = 0$[16]. Here, ω, k and δ are the angular velocity, the wave vector and the phase of the EM-wave respectively, while E_{0X} and E_{0Y} are the complex amplitudes of the fields. From Eq. (2.2), it is clear that the real fields can be expressed as

$$\begin{aligned} E_x &= E_{0X} \cos(\omega t - kz + \delta_x), \\ E_y &= E_{0Y} \cos(\omega t - kz + \delta_y). \end{aligned} \tag{2.3}$$

Using the the geometric identity,

$$\cos\alpha \pm \beta = \cos\alpha \cos\beta \mp \sin\beta \sin\alpha,$$

Eqs. (2.3) may be combined to find

$$\frac{E_x^2}{E_{0X}^2} + \frac{E_y^2}{E_{0Y}^2} - 2\frac{E_x}{E_{0X}}\frac{E_y}{E_{0Y}} \cos\delta = \sin^2\delta, \tag{2.4}$$

with $\delta = \delta_y - \delta_x$. One may recognize this formula to be that of an ellipse[17]. This means that, in the general case, the electrical field traces an ellipse while propagating, commonly called the *Polarization Ellipse*.

As seen in Figure 1, the angles θ, $\psi = \arctan\left(\frac{E_{0X}}{E_{0Y}}\right)$ and ϵ naturally arise, and are a useful alternative way to the E-fields to completely describe the polarization ellipse.

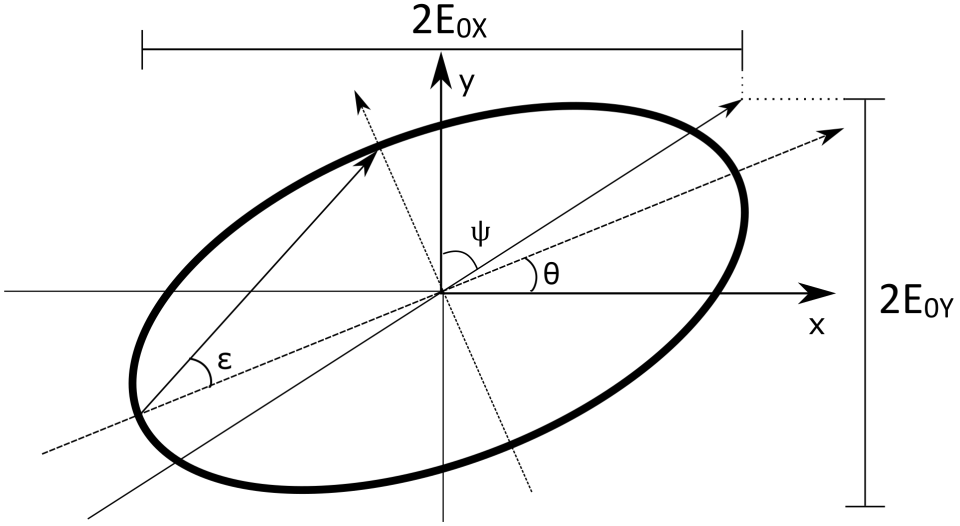

Figure 1: A trace of a general polarization ellipse with magnitudes E_{oX} and E_{0Y} tilted at an angle θ, and with an ellipticity angle ϵ and the absolute angle between E_{0X} and E_{0Y}, ψ.

For the special cases of $\delta = \frac{\pi}{2} + n\pi$, where $n = 0, 1, 2, ...$, we find that Eq. (2.4) reduces to

$$\frac{E_x^2}{E_{0X}^2} + \frac{E_y^2}{E_{0Y}^2} = 1, \tag{2.5}$$

or that of an non rotated ellipse with semi major and minor axis corresponding to E_{0X} and E_{0Y} respectively. In the special case of $E_{0X} = E_{0Y}$, Eq. (2.5) is reduced to a circle, producing circularly polarized light. If $\sin\delta > 0$, the state is referred to as *right circularly polarized*, and conversely $\sin\delta < 0$ is referred to as *left circularly polarized*[18].

In the case where δ is any multiple of π, Eq. (2.4) is reduced to

$$\frac{E_x^2}{E_{0X}^2} + \frac{E_y^2}{E_{0Y}^2} \pm 2\frac{E_x}{E_{0X}}\frac{E_y}{E_{0Y}} = 0, \tag{2.6}$$

which may be further reduced to

$$\left(\frac{E_x}{E_{0X}} \pm \frac{E_y}{E_{0Y}}\right)^2 = 0, \tag{2.7}$$

that may written as

$$E_x = \pm\frac{E_{0X}}{E_{0Y}}E_y. \tag{2.8}$$

It is clear that Eq. (2.8) represents a line with slope $\pm\frac{E_{0X}}{E_{0Y}}$, which is why this state is called *linear polarization*. If $E_{0Y} = 0$, the state is referred to as *horizontal linear polarization* while $E_{0X} = 0$ is referred to as *vertical linear polarization*. In the case of $E_{0Y} = \pm E_{0X}$, the state is called *linear* $+45°$ or *linear* $-45°$ respectively.

2.1.1 Jones Formalism

An efficient way to describe the polarization state of a fully polarized electromagnetic wave is to consider the electric field components and their relative phase. Such a formalism based on linear algebra was devised by R. Clark Jones[19]. He had the idea to let Eq. (2.2) can be written on the form

$$\vec{E} = \begin{bmatrix} E_{0X} e^{i\delta_x} \\ E_{0Y} e^{i\delta_y} \end{bmatrix}. \tag{2.9}$$

To represent a non-depolarizing optical component one may use a 2×2 matrix $\mathbf{J}$, called the Jones matrix. This matrix links the incoming polarization state $\vec{E}$ with the outgoing polarization state $\vec{E}'$ of an electromagnetic wave as

$$\vec{E}' = \mathbf{J}\vec{E}. \tag{2.10}$$

Here $\mathbf{J}$ is a 2×2 matrix on the form

$$\mathbf{E} = \begin{bmatrix} j_{11} & j_{12} \\ j_{21} & j_{22} \end{bmatrix}. \tag{2.11}$$

In the case of multiple optical components in order $\mathbf{J_1}, \mathbf{J_2}, ...\mathbf{J_N}$, the total system may be represented with

$$\vec{E}' = \mathbf{J_N J_{N-1}} \cdots \mathbf{J_2 J_1} \vec{E}, \tag{2.12}$$

due to the fact that Eq. (2.11) is a square matrix. It is important that the optical components work on the Jones vector in the same order as the beam interacts with the optical components they represent, due to the non-commutative natures of both these operations. From Eq. (2.12) it is natural to combine the N Jones matrices into a total system matrix

$$\mathbf{J_{sys}} = \mathbf{J_N J_{N-1}} \cdots \mathbf{J_2 J_1}. \tag{2.13}$$

Any Jones matrix may be rotated by an angle α using the standard 2D-rotation matrix

$$\mathbf{R}(\alpha) = \begin{bmatrix} \cos\alpha & \sin\alpha \\ -\sin\alpha & \cos\alpha \end{bmatrix}, \tag{2.14}$$

so that

$$\mathbf{J}(\alpha) = \mathbf{R}(-\alpha)\mathbf{J}\mathbf{R}(\alpha) \tag{2.15}$$

2.1.2 Stokes Formalism

Despite Jones matrices being intuitive, compact and simple to work with, it is not complete in the sense that it can not be used to described partially polarized or depolarized electromagnetic waves. What is more, in practice the electric field amplitudes and the phases between them are difficult to measure directly. It is therefore useful to construct a formalism that can describe electromagnetic waves that are partially polarized with real, easily measurable quantities. Such a formalism was first defined by George Gabrielle Stokes[20]. Following his work, it is possible to time average Eq. (2.4), indicated by $\langle ... \rangle$,

$$\frac{\langle E_x^2 \rangle}{E_{0X}^2} + \frac{\langle E_y^2 \rangle}{E_{0Y}^2} - 2\frac{\langle E_x E_y \rangle}{E_{0X} E_{0Y}} \cos\delta = \sin^2\delta. \tag{2.16}$$

The time averaged quantities in Eq. (2.16) may be found using the expressions in Eqs. (2.3) to be

$$\begin{aligned} \langle E_x^2 \rangle &= \frac{1}{2} E_{0X}^2, \\ \langle E_y^2 \rangle &= \frac{1}{2} E_{0Y}^2, \\ \langle E_x E_y \rangle &= \frac{1}{2} E_{0X} E_{0Y} \cos\delta. \end{aligned} \tag{2.17}$$

Inserting Eqs. (2.17) into Eq. (2.16), while multiplying with $4E_{0X}E_{0Y}$ before adding and subtracting $E_{0X}^2 + E_{0Y}^2$ results in

$$(E_{0X}^2 + E_{0Y}^2)^2 - (E_{0X}^2 - E_{0Y}^2) - (2E_{0X}E_{0Y}\cos\delta)^2 = (2E_{0X}E_{0Y}\sin\delta)^2, \tag{2.18}$$

which may be rewritten as

$$(I_x + I_y)^2 - (I_x - I_y) - (I_{45^\circ} - I_{-45^\circ})^2 = (I_R - I_L)^2, \tag{2.19}$$

naturally giving rise to the four Stokes parameters

$$S_0 = I_x + I_y, \tag{2.20}$$

$$S_1 = I_x - I_y, \tag{2.21}$$

$$S_2 = I_{45^\circ} - I_{-45^\circ}, \tag{2.22}$$

$$S_3 = I_R - I_L. \tag{2.23}$$

S_0 is the total irradiance, S_1 is the difference in irradiance between the x- and y- polarizations, S_2 the difference between $+45^\circ$ and -45° directions, and S_3 the difference in irradiance between right and left circularly polarized light. Inserting these four parameters into a vector, one obtains the stokes vector

$$\vec{S} = \begin{bmatrix} S_0 \\ S_1 \\ S_2 \\ S_3 \end{bmatrix} = \begin{bmatrix} I_x + I_y \\ I_x - I_y \\ I_{45^\circ} - I_{-45^\circ} \\ I_R - I_L \end{bmatrix} = \begin{bmatrix} E_{0X}^2 + E_{0Y}^2 \\ E_{0X}^2 - E_{0Y}^2 \\ 2E_{0X}E_{0Y}\cos\delta \\ 2E_{0X}E_{0Y}\sin\delta \end{bmatrix} = A^2 \begin{bmatrix} 1 \\ \cos 2\epsilon \cos 2\theta \\ \sin 2\epsilon \cos 2\theta \\ \sin 2\epsilon \end{bmatrix}. \tag{2.24}$$

It is common to normalize Eq. (2.24) with respect to the total intensity, as this is easier to work with, and does not detract any information from the formalism.

Using the previously defined Stokes parameters, Eq. (2.18) can be written as

$$1 = \frac{\sqrt{S_1^2 + S_2^2 + S_3^2}}{S_0}, \tag{2.25}$$

in the assumed case of a completely polarized wave. In the more general case of a partially polarized wave, Eq. (2.25) naturally gives rise to the *degree of polarization*

$$P = \frac{\sqrt{S_1^2 + S_2^2 + S_3^2}}{S_0} = \frac{I_{pol}}{I_{tot}}, \tag{2.26}$$

providing a measure for how polarized a given electromagnetic wave is. The stokes formalism is therefore, unlike the Jones formalism, compatible with unpolarized and partially polarized light. This generalization makes the Stokes formalism more difficult to work with than the Jones formalism, as there are more elements to take into consideration when making calculations. It also has the disadvantage of not being able to properly describe coherence and interference phenomenon, which the Jones formalism is capable of. The advent of computers coupled with the limitations of the Jones formalism has however lead the Stokes formalism to be the preferred one in many situations, despite these shortcomings.

Looking closer at Eq. (2.24), it is clear that S_1, S_2 and S_3 represents the transformation from spherical coordinates to a three dimensional Cartesian system when normalized. Plotting all possible values for completely polarized light reveals a sphere of unit length. This construct was first introduced by Henri Poincaré, thereby giving it its name the *Poincaré sphere*. Any points within the sphere represents a partially polarized state, while outside represents unphysical states. One may readily observe from Figure 2 that the north and south poles corresponds to left- and right-circular polarized light respectively, the equator represents various linearly polarized states while everything else is some form of elliptically polarized state.

2.1.3 Mueller Marices

It has been shown that a 4×4 matrix is sufficient to relate the incoming and outgoing Stokes vectors, $\vec{S}$ and $\vec{S}'$. Such a matrix was first formulated by H. Mueller in the 1940s, and was being promoted in his lectures during the same time. The findings were not well documented beyond this until they were published in a now declassified report[22, 23].

A general Mueller matrix is on the form

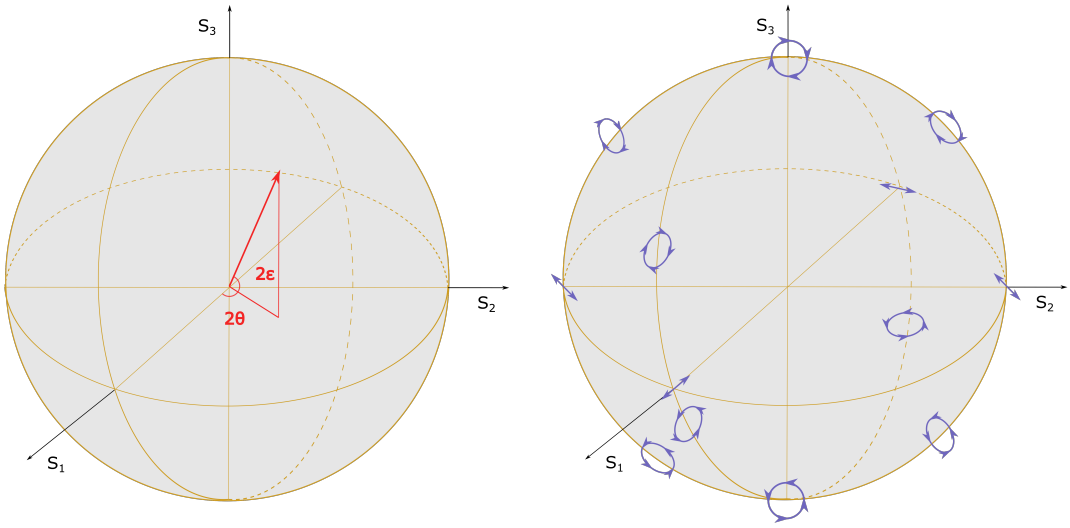

Figure 2: Illustration of the Pointcaré sphere with coordinates, and a selection of states of polarization on the Pointcaré sphere. Adapted from[21].

$$\mathbf{M} = \begin{bmatrix} M_{00} & M_{01} & M_{02} & M_{03} \\ M_{10} & M_{11} & M_{12} & M_{13} \\ M_{20} & M_{21} & M_{22} & M_{23} \\ M_{30} & M_{31} & M_{32} & M_{33} \end{bmatrix}, \tag{2.27}$$

and connect the two Stokes Vectors

$$\vec{S'} = \mathbf{M}\vec{S}. \tag{2.28}$$

If the Mueller matrix is normalized with respect to M_{00}, each element $m_{ij} = \frac{M_{ij}}{M_{00}}$ in Eq. (2.27) may take a value between -1 and 1, and may also describe any depolarization that may occur due to the system. If a system contains more than one optical component, it is possible to stack the Mueller Matrices in the same way as was done for Jones Matrices in (2.13). Mueller matrices may also be rotated similar to how Jones matrices are in Eq. (2.15) with

$$\mathbf{R}(\alpha) = \begin{bmatrix} 1 & 0 & 0 & 0 \\ 0 & \cos 2\alpha & \sin 2\alpha & 0 \\ 0 & -\sin 2\alpha & \cos 2\alpha & 0 \\ 0 & 0 & 0 & 1 \end{bmatrix}. \tag{2.29}$$

Systems with no depolarization may be described with both Jones and Mueller matrices. To transform between the two, one needs only use the relation

$$\mathbf{M} = \mathbf{A}(\mathbf{J} \otimes \mathbf{J}^*)\mathbf{A}^{-1}, \tag{2.30}$$

where $\otimes$ is the Kronecker product and $\mathbf{A}$ is the conversion matrix

$$\mathbf{A} = \begin{bmatrix} 1 & 0 & 0 & 1 \\ 1 & 0 & 0 & -1 \\ 0 & 1 & 1 & 0 \\ 0 & i & -i & 0 \end{bmatrix}. \tag{2.31}$$

2.1.4 Diattenuators

A diattenuator is an optical element that attenuates EM waves differently along the x and y axis while not affecting their relative phase[5, 16]. If the object completely attenuates the electric field along one direction while not affecting the orthogonal field, the diattenuator is called an ideal linear polarizer. Such a diattenuator along the x-direction may be described as

$$\mathbf{M} = \begin{bmatrix} 1 & 1 & 0 & 0 \\ 1 & 1 & 0 & 0 \\ 0 & 0 & 0 & 0 \\ 0 & 0 & 0 & 0 \end{bmatrix} \quad \text{or} \quad \mathbf{J} = \begin{bmatrix} 1 & 0 \\ 0 & 0 \end{bmatrix}. \tag{2.32}$$

When the linear polarizer is rotated with with an azimuthal angle of α, Eq. (2.32) transforms to

$$\mathbf{M} = \frac{1}{2} \begin{bmatrix} 1 & \cos 2\alpha & \sin 2\alpha & 0 \\ \cos 2\alpha & \cos^2 2\alpha & \sin 2\alpha \cos 2\alpha & 0 \\ \sin 2\alpha & \sin 2\alpha \cos 2\alpha & \sin^2 2\alpha & 0 \\ 0 & 0 & 0 & 0 \end{bmatrix} \quad \text{or} \quad \mathbf{J} = \begin{bmatrix} \cos^2 \alpha & \sin \alpha \cos \alpha \\ \sin \alpha \cos \alpha & \sin^2 \alpha \end{bmatrix} \tag{2.33}$$

There are several types of linear polarizers, utilizing distinct phenomena. Perhaps the simplest is the wire grid polarizer, where thin parallel metal wires reflect back one polarization and transmit the orthogonal polarization. In sheet polarizers, the polarization is absorbed rather than reflected back. Lastly, many prism polarizers work not by attenuating one polarization, but splitting the orthogonal polarizations, making them travel in different directions. There are many types of prism polarizers, but Glan-Thomson and Rochon polarizers are common ones.

2.1.5 Retarders

Retarders are the complement to diattenuators as they influence the phase difference of the fields of the EM waves propagating through them, while not attenuating their field amplitude. An accumulation of phase shift is induced due to the crystal which the EM-wave propagates through being an electrically anisotropic, or *birefringent* material.

There are two main categories of birefringent crystals, *biaxial* and *uniaxial*. In the case where all the perpendicular axes have unique electrical properties, the crystal is said to be biaxial, while if only one of the axed differs from the other two, it is said to be uniaxial. It is common to refer to the unique axis in a uniaxial crysal as the *optical axis* or the *extraordinary axis*. The other axes is the appropriately called the *ordinary axes*. These axes correspond to the extraordinary and ordinary refractive indices n_e and n_o respectively. The axis which permits EM waves to propagate the fastest is also often referred to as the *fast axis*, while the *slow axis* corresponds to the axis along which the propagation is slower.

Allowing EM waves of wavelength λ propagate through a uniaxial material with the optical axis in the x-direcion and the ordinary axis in the y-direction leads to a Jones matrix on the form

$$\mathbf{J} = \begin{bmatrix} e^{\frac{i2\pi dn_e}{\lambda}} & 0 \\ 0 & e^{\frac{i2\pi dn_o}{\lambda}} \end{bmatrix} = e^{\frac{i2\pi dn_e}{\lambda}} \begin{bmatrix} 1 & 0 \\ 0 & e^{i\Delta} \end{bmatrix}, \tag{2.34}$$

where $\Delta = \frac{2\pi}{\lambda} d(n_o - n_e)$. Here, Δ is the *retardation* of the retarder. In the case where $\Delta = \pm 90°$ or $\Delta = \pm 180°$, one obtains what is usually referred to as a quarter-, and half-wave plate. These are given unique names as they are convenient for manipulating the polarization states of an EM-wave.

If one considers this phenomenon carefully it is possible to see that retardance may be represented by a rotation on the Poincaré sphere, leading to a general Mueller matrix on the form

$$\mathbf{M} = \begin{bmatrix} 1 & \vec{0}^T \\ \vec{0} & \mathbf{m}_R \end{bmatrix}, \tag{2.35}$$

where $\mathbf{m}_R$ is a 3×3 rotation matrix and $\vec{0}$ is the three element zero-vector[24].

2.1.6 Analyzing the Mueller Matrix

As the Mueller Matrix may represent a variety of systems, it is useful to develop methods to analytically describe its properties. There are several ways of doing this, however one of the most common is to decompose the matrix. There are several viable decomposition methods, each with its own advantages and disadvantages. One of the most common methods is polar decomposition, as described by Lu and Chipman[24]. Splitting the matrix into three matrix factors on the form

$$\mathbf{M} = \mathbf{M}_\Delta \mathbf{M}_R \mathbf{M}_D, \tag{2.36}$$

where the factors $\mathbf{M}_\Delta$, $\mathbf{M}_R$, $\mathbf{M}_D$ are the dipolarizer, retarder and diattenuator components respectively, it is possible to gain insight into the physical characteristics of both polarized and depolarized systems. It is furthermore convenient to write Eq. (2.27) on the form

$$\mathbf{M} = \begin{bmatrix} 1 & m_{01} & m_{02} & m_{03} \\ m_{10} & m_{11} & m_{12} & m_{13} \\ m_{20} & m_{21} & m_{22} & m_{23} \\ m_{30} & m_{31} & m_{32} & m_{33} \end{bmatrix} = \begin{bmatrix} 1 & \vec{D}^T \\ \vec{P} & \mathbf{m} \end{bmatrix}, \tag{2.37}$$

introducing the *polarizance vector* and *diattenuation vector* $\vec{P}$ and $\vec{D}$, where

$$\vec{P} = \begin{bmatrix} m_{10} \\ m_{20} \\ m_{30} \end{bmatrix} \quad \text{and} \quad \vec{D} = \begin{bmatrix} m_{01} \\ m_{02} \\ m_{03} \end{bmatrix}. \tag{2.38}$$

$\mathbf{M}_D$ is the first factor to be found. It may be shown that an ideal diattenuator is on the form

$$\mathbf{M}_D = T_u \begin{bmatrix} 1 & \vec{D}^T \\ \vec{D} & \mathbf{m}_D \end{bmatrix}, \tag{2.39}$$

where T_u is the transmittance for unpolarized light and

$$\mathbf{m_D} = \sqrt{1-D^2}\mathbf{I} + (1-\sqrt{1-D^2})\hat{D}\hat{D}^T, \tag{2.40}$$

where $\mathbf{I}$ is the 3×3 identity matrix, $D = \left|\vec{D}\right|$ and $\hat{D} = \frac{\vec{D}}{|\vec{D}|}$. From here, one proceeds by calculating the inverse of the diattenuation matrix, to find the remaining matrix

$$\mathbf{M}' = \mathbf{M}\mathbf{M}_D^{-1}. \tag{2.41}$$

It has also been shown that the depolarization matrix may be written as

$$\mathbf{M}_\Delta = \begin{bmatrix} 1 & \vec{0}^T \\ \vec{P}_\Delta & \mathbf{m}_\Delta \end{bmatrix}. \tag{2.42}$$

Here $\vec{P}_\Delta$ is the polerizance vector of the depolarizer and $\mathbf{m}_\Delta$ is a 3×3 matrix. Using Eqs. (2.42) and (2.35) leads to Eq. (2.41) being written as

$$\mathbf{M}' = \mathbf{M}_\Delta \mathbf{M}_R = \begin{bmatrix} 1 & \vec{0}^T \\ \vec{P}_\Delta & \mathbf{m}_\Delta \end{bmatrix} \begin{bmatrix} 1 & \vec{0}^T \\ \vec{0} & \mathbf{m}_R \end{bmatrix} = \begin{bmatrix} 1 & \vec{0}^T \\ \vec{P}_\Delta & \mathbf{m}_\Delta \mathbf{m}_D \end{bmatrix}. \tag{2.43}$$

If the Mueller matrix is non-depolorizing the decomposition is finished, as the depolarization matrix is equal to the identity matrix. In the case where the Mueller matrix is depolarizing, the depolerization matrix is found by utilizing that

$$\vec{P}_\Delta = \frac{\vec{P} - \mathbf{m}\vec{D}}{1-D^2}, \tag{2.44}$$

and

$$\begin{aligned} \mathbf{m}_\Delta = &\left[\pm\mathbf{m}'\left(\mathbf{m}'\right)^T + \left(\sqrt{\lambda_1\lambda_2} + \sqrt{\lambda_2\lambda_3} + \sqrt{\lambda_3\lambda_1}\right)\mathbf{I}\right]^{-1} \times \\ &\left[\left(\sqrt{\lambda_1} + \sqrt{\lambda_2} + \sqrt{\lambda_3}\right)\mathbf{m}'(\mathbf{m}')^T + \sqrt{\lambda_1\lambda_2\lambda_3}\mathbf{I}\right], \end{aligned} \tag{2.45}$$

where $\sqrt{\lambda_i}$ the i-th eigenvalue of $\mathbf{m}_\Delta$, and $\mathbf{m}' = \mathbf{m}_\Delta\mathbf{m}_D$. The sign in Eq. (2.45) is determined by the sign of the determinant of $\mathbf{m}'$. Inserting Eqs. (2.44) and (2.45) into Eq. (2.42) the retarder matrix is found to be

$$\mathbf{M}_R = \mathbf{M}_\Delta^{-1}\mathbf{M}'. \tag{2.46}$$

2.2 Reflectance and Transmittance

Reflection and transmittance of light at the interface of two media was first described by the *Fresnel equations of reflectance and transmittance* by their namesake Augustin-Jean Fresnel in a series of articles in the early 1800s[25]. Here, electromagnetic theory is used to derive the coefficients that relate the incoming, reflected and transmitted field strengths[1]. By defining a plane of incidence, along which the incident EM waves propagate as showcased in Figure 3, it is possible to decompose said EM-wave into two orthogonal polarizations, one where the electric field is perpendicular to the plane of incidence, and one where it is parallel to the plane of incidence.

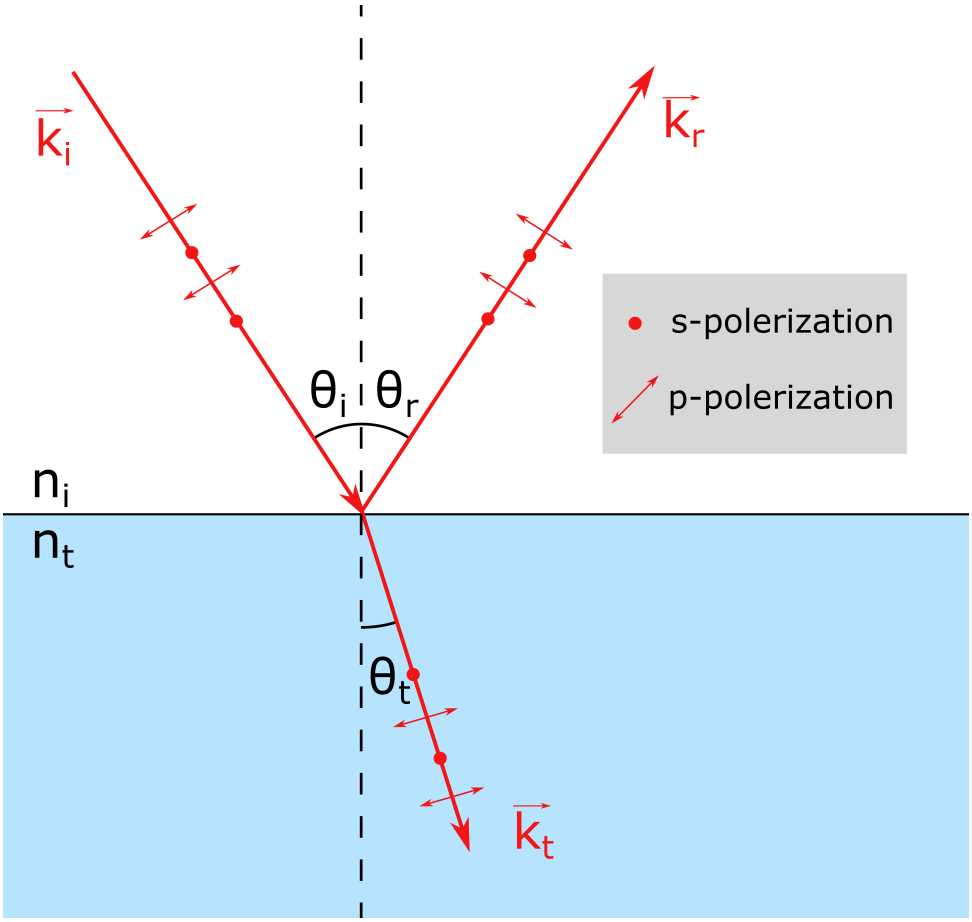

Figure 3: Illustration of the plane of incidence where EM-wave $\vec{k_i}$ propagates in a material of refractive index n_i until it reaches a material n_t. The wave is partially reflected and transmitted along $\vec{k_r}$ and k_t respectively. The p-polarization is parallel to the plane of incidence, while the s-polarization is perpendicular to the plane. Adapted from[16]

.

Observing the perpendicular polarisation with relevant boundary conditions for Maxwell's equations, one finds, if the media are isotropic

$$\vec{E}_i + \vec{E}_r = \vec{E}_t, \tag{2.47}$$

[1]The original derivation of the Fresnel equations did not utilize electromagnetic theory explicitly, as the discovery that light was an EM-wave was yet to be made at the time. Rather, general principles of wave physics were used to derive the formulas.

and

$$-B_i \cos\theta_i + B_r \cos\theta_r = B_t \cos\theta_t. \tag{2.48}$$

Here $\vec{E}_i$, $\vec{E}_r$, $\vec{E}_t$ are the incoming, reflected and transmitted electric fields respectively and θ_i, θ_r andθ_t are likewise the angles of incoming, reflected and transmitted beam. The magnetic field components used in Eq. (2.48) are the tangential components with respect to the interface. Furthermore, the magnetic permeability is assumed to be equal in the two media.

Using that $\theta_i = \theta_r$ along with the relation $B = \frac{E}{v}$, where $v = \frac{c}{n}$ is the propagation speed of the EM-wave, Eq. (2.48) may be written

$$n_i \left(E_i - E_r\right) \cos\theta_i = n_t E_t \cos\theta_t. \tag{2.49}$$

Combining Eqs. (2.49) and (2.47) leads to the sets of equations

$$\begin{aligned} r_{pp} &= \left(\frac{E_r}{E_i}\right) = \frac{n_i \cos\theta_i - n_t \cos\theta_t}{n_i \cos\theta_i + n_t \cos\theta_t}, \\ t_{pp} &= \left(\frac{E_t}{E_i}\right) = \frac{2n_i \cos\theta_i}{n_i \cos\theta_i + n_t \cos\theta_t}. \end{aligned} \tag{2.50}$$

The same procedure may be followed for the parallel polarisation leading to the equivalent equations

$$\begin{aligned} r_{ss} &= \left(\frac{E_r}{E_i}\right) = \frac{n_t \cos\theta_t - n_i \cos\theta_i}{n_i \cos\theta_i + n_t \cos\theta_t}, \\ t_{ss} &= \left(\frac{E_t}{E_i}\right) = \frac{2n_i \cos\theta_i}{n_i \cos\theta_i + n_t \cos\theta_t}. \end{aligned} \tag{2.51}$$

Based on Eq. (2.51), it is possible to define the complex ratio

$$\rho_{pp} = \frac{r_{pp}}{r_{ss}} = \frac{t_{pp}}{t_{ss}} = \tan\Psi_{pp} e^{i\Delta_{pp}}, \tag{2.52}$$

describing the change in polarization due to reflection or transmittance. The relative change in amplitude is denoted by Ψ and Δ is the relative phase change. These quantities are central in ellipsometry, as they are the quantities directly measured by a complete ellipsometer[5].

For non-isotropic samples, some cross-polarization does occur. To adequately describe the change in polarization, two additional quantities need to be measured

$$\rho_{ps} = \frac{r_{ps}}{r_{ss}} = \frac{t_{ps}}{t_{ss}} = \tan\Psi_{ps} e^{i\Delta_{ps}} \quad \text{and} \quad \rho_{sp} = \frac{r_{sp}}{r_{ss}} = \frac{t_{sp}}{t_{ss}} = \tan\Psi_{sp} e^{i\Delta_{sp}}. \tag{2.53}$$

Here r_{sp}/t_{sp} is the transfer of polarization from p- to s-polarized EM waves. The opposit is true for r_{ps}/t_{ps}. The general Jones matrix for a transmitting material is then

$$\mathbf{J_t} = \begin{bmatrix} t_{pp} & t_{ps} \\ t_{sp} & t_{ss} \end{bmatrix}. \tag{2.54}$$

Transforming Eq.(2.54) into a Mueller matrix using Eq.(2.30) results in

$$\mathbf{M}^T_{anisotropic} = \begin{bmatrix} \frac{1}{2}(|t_{pp}|^2 + |t_{sp}|^2 + |t_{ps}|^2 + |t_{ss}|^2) & \frac{1}{2}(|t_{pp}|^2|t_{sp}|^2 - |t_{ps}|^2 - |t_{ss}|^2) \\ \frac{1}{2}(|t_{pp}|^2 + |t_{sp}|^2 + |t_{ps}|^2 + |t_{ss}|^2) & \frac{1}{2}(|t_{pp}|^2 + |t_{sp}|^2 + |t_{ps}|^2 + |t_{ss}|^2) \\ \mathfrak{Re}(t_{pp}t^*_{sp} + t_{ps}t^*_{ss}) & \mathfrak{Re}(t_{pp}t^*_{sp} - t_{ps}t^*_{ss}) \\ -\mathfrak{Im}(t_{pp}t^*_{sp} + t_{ps}t^*_{ss}) & \mathfrak{Re}(t_{pp}t^*_{sp} - t_{ps}t^*_{ss}) \end{bmatrix}$$
$$\begin{bmatrix} \mathfrak{Re}(t_{pp}t^*_{ps} + t_{sp}t^*_{ss}) & \mathfrak{Im}(t_{pp}t^*_{ps} + t_{sp}t^*_{ss}) \\ \mathfrak{Re}(t_{pp}t^*_{ps} + t_{sp}t^*_{ss}) & \mathfrak{Im}(t_{pp}t^*_{ps} + t_{sp}t^*_{ss}) \\ \mathfrak{Re}(t_{pp}t^*_{ss} + t_{ps}t^*_{sp}) & \mathfrak{Im}(t_{pp}t^*_{ss} + t_{ps}t^*_{sp}) \\ -\mathfrak{Im}(t_{pp}t^*_{ss} + t_{ps}t^*_{sp}) & \mathfrak{Re}(t_{pp}t^*_{ss} + t_{ps}t^*_{sp}) \end{bmatrix}. \quad (2.55)$$

If the transmission sample is isotropic, $t_{ps} = t_{sp} = 0$. This transforms Eq.(2.55) into

$$\mathbf{M}^T_{isotropic} = \tau \begin{bmatrix} 1 & -N & 0 & 0 \\ -N & 1 & 0 & 0 \\ 0 & 0 & C & S \\ 0 & 0 & -S & C \end{bmatrix}, \quad (2.56)$$

where

$$\begin{aligned} N &= \cos 2\Psi, \\ C &= \sin 2\Psi \cos \Delta, \\ S &= \sin 2\Psi \sin \Delta, \end{aligned}$$

and the transmission coefficient

$$\tau = \frac{\|t_{pp}\|^2 + \|t_{ss}\|^2}{2}.$$

2.3 Supercontinuum Laser Sources

Supercontinuum sources are categorized as lasers sources with a broad wavelength spectra and a flat power density distribution. This makes supercontinuum sources useful in a broad range of applications, such as IR microscopy[26], particle trapping and manipulation[27, 28], as well as a tool for non invasive diagnostics of tissue[29].

The broad spectrum of the supercontinuum source starts with a pump laser which undergoes several processes that lead to spectral broadening[30].

In a low intensity regime, the dielectric polarization response describing the electric dipole moment per unit volume may be written as

$$\vec{P} = \epsilon_0 \chi \vec{E}, \quad (2.57)$$

where χ is here the electric susceptibility of the media in question. This corresponds to a model of the electron as a harmonically oscillating particle with respect to its host nucleus, inducing an electrical

dipole moment. When certain materials are exposed to EM-radiation with high intensity this model will start to break down and the polarization response diverges from the linear model as presented in Eq.(2.57). To account for this, it is necessary to consider the contributions from higher powers of $\vec{E}$ to the polarization. This can be done by simply expanding Eq. (2.57) to

$$\vec{P} = \epsilon_0 \left(\chi^{(1)} \vec{E} + \chi^{(2)} \vec{E}^2 + \chi^{(3)} \vec{E}^3 + ... \right). \tag{2.58}$$

Phenomena resulting from these higher order terms are called *non-linear effects*. If one assumes the pump laser propagates through a non-linear material with an inversion center[2], as commonly is the case, the cubic term will be the dominant non-linear term, implying

$$P = \epsilon_0 \left(\chi^{(1)} E + \chi^{(3)} E^3 \right). \tag{2.59}$$

Eq. (2.59) implies the polarisation to be proportional on the intensity $I = c\epsilon_0 n_0/2|E|^2$. This in turn creates a perturbation of the refractive index

$$n = n_0 + n_2 I, \tag{2.60}$$

here n_0 is the usual $\sqrt{\chi^{(1)}}$ while n_2 is linked to the cubic susceptibility as

$$n_2 = \frac{3\chi^{(3)}}{4\epsilon_0 c n_0^2}.$$

This perturbation of the refractive index causes a self focusing phenomena where the beam is, given high enough intensity, focusing in on itself until an equilibrium is reached due to diffraction and other beam expanding phenomena. When this equilibrium is reached, one is said to have a *soliton* wave. Since the beam does not have a uniform intensity distribution, the perturbed refractive index leads to self phase modulation according to

$$\phi_{nl}(t) = \frac{\omega_0}{c} \int_0^L I(t, z) dz, \tag{2.61}$$

This phase modulation in turn leads to a frequency change

$$\delta\omega = \frac{d\phi_{nl}(t)}{dt} \tag{2.62}$$

along the intensity distribution.

Another important effect for Supercontinuum generation is *Four-wave mixing*. Here two photons (ω_1 and ω_2) interact according to energy and momentum conservation to create two new photons (ω_3 and ω_4) called the signal and idler, causing a broadening of the spectrum according to $\omega_3 = 2\omega_1 - \omega_2$ and $\omega_4 = 2\omega_2 - \omega_1$[31]. This effect, like self phase modulation, occur due to third order non-linearity in the material. There are also other effects that play into the broadening of the wavelength spectrum like plasmon excitations that modulates the phase of the beam in a similar manner to that of the self modulation. Another prominent effect is Raman scattering, where photons interacts with

[2]A material is said to have an inversion center if there is a point where the vectors describing the positions of the atoms in the unit cell $\vec{u}_i$ may go to $-\vec{u}_i$ without changing the structure of the unit cell.

phonons in the non-linear media to further broaden the spectrum. The contribution of each type of frequency modulation is highly dependent on the original pulse length from the laser source[32]. For sub femtosecond pulses, soliton related effects (e.g. self phase modulation) are dominant, while Four-wave mixing increase in prominence as pulse widths expand.

A supercontinuum source may be made using any strongly non-linear optical medium, like that of calcite. In practice however, many supercontinuum lasers utilize non-linear optical fibers. This is due to their high non-linearity and relative low cost and power loss. Recently, *Photonic Crystal Fibers* have been shown to be of great interest for supercontinuum generation, as well as other applications like telecommunications[33, 34]. These types of optical fibers differ from the more typical arrangement of a solid, high refractive index core surrounded by a cladding of lower refractive index, by the introduction of centro-symmetric structures running along the length of the fiber. Often, these structures are simply air filled holes, as can be seen in Figure 4. The arrangements and sizes of these holes may be precise engineered for the application at hand, e.g. increasing the non-linear effects of the fiber. To achieve this, a large air-fill ratio is desirable.

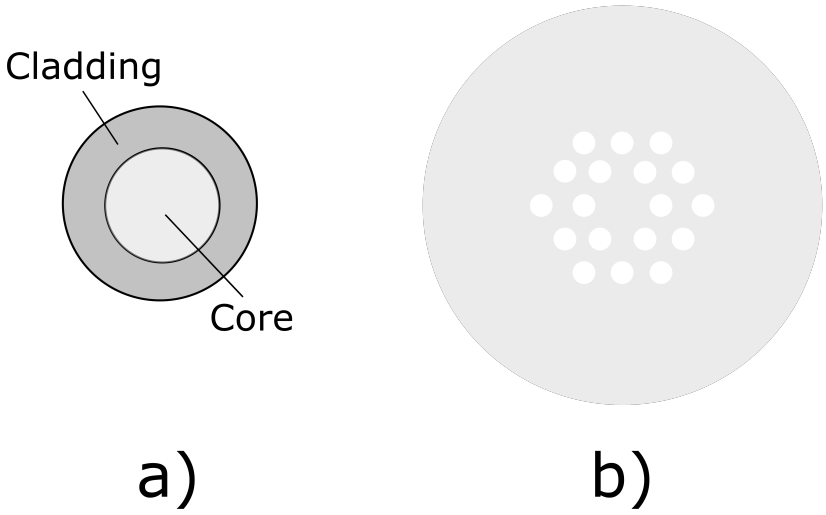

Figure 4: a) displays a basic classical fiber design with a core surrounded by cladding. b) shows a typical design for a PCF. The air holes surrounding the central core forms a hexagonal pattern. Adapted from[34].

2.4 Acusto-optic Tunable Filter

The acousto-optic tunable filter (AOTF) uses the acousto-optic (AO) effect to effectively select the desired frequency from an incident beam of EM-radiation[35]. These devices uses high-frequency vibrational stress to periodically perturb the density and refractive index. The resulting waves in the medium can be considered to be a beam of phonons, analogous to the way a beam of light may be considered to be a beam of photons.

The AOTF can be divided into two categories, collinear and non-collinear. In the collinear AOTF the incident light goes parallel to the acoustic wave and causes a shift in polarization of the diffracted light. The non-collinear AOTF is shown in Figure 5 and operates with the incident beam at an angle of the acoustic wave[36]. As a result, a difference in angle between the incident beam and the diffracted beam is also observed. This case can again be split into two scenarios, based on if the crystal in question is isotropic or anisotropic. The first case diffracts light according to Bragg's law, while the second requires some modification of this law.

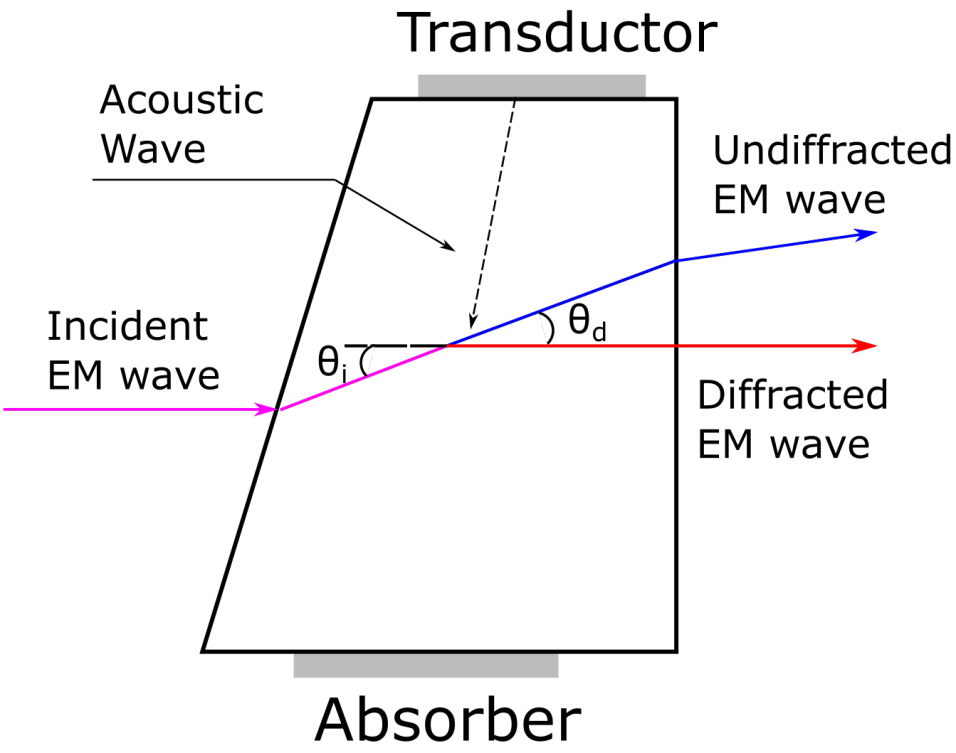

Figure 5: Schematic representation of a non-collinear AOTF. Pink incident light enters the AOTF and is refracted. Photons forming the acoustic beam traveling from the transductor to the absorber interacts with the the photons in the light beam and red light is diffracted out, while the rest of the beam continious along the same path.

The basis of the AO-effect is the interaction between the incoming photons and the phonons in the media. Considering energy and momentum conservation

$$\vec{k_i} = \vec{k_d} + \vec{k_a}, \tag{2.63}$$

and

$$\nu_i = \nu_d \pm f_0, \tag{2.64}$$

it is possible to derive the angle of the diffracted beam. Here, $\vec{k_i}$,$\vec{k_d}$, and $\vec{k_a}$ are the momentum vectors of the incoming, diffracted and acoustic beam, while ν_i, ν_d, and f_0 are the frequencies of the incoming, diffracted and acoustic beam.

Following[37], the wave vectors can be expressed as

$$k_i = \frac{2\pi n_i}{\lambda_0}, \quad k_d = \frac{2\pi n_d}{\lambda_0}, \quad \text{and} \quad k_a = \frac{2\pi f_a}{v_a} \tag{2.65}$$

where λ_0 is the wavelength of the diffracted beam in vacuum, n_i and n_d are the refractive indices of the incoming and diffracted light in the diffracted medium, and f_a and v_a are the acoustic frequency

and velocity. Inserting Eq.(2.65) in Eq.(2.63) results in

$$\frac{n_d}{\lambda_0} = \frac{n_i}{\lambda_0} + \frac{f_a}{v_a}. \tag{2.66}$$

Solving Eq.(2.66), assuming extraordinary polarization of the incident beam and extraordinary polarization of the diffracted beam, results in the zero angle output wavelength from the collinear AOTF being

$$\lambda_0 = \frac{\Delta n}{f_a}, \tag{2.67}$$

where $\Delta n = n_d - n_i$ is the birefringence of the AOTF material.

The treatment of an isotropic non-collinear AOTF differs slightly from that of a collinear AOTF. To simplify the calculations the condition Eq.(2.63) may be treated with respect to normal and parallel components of the acoustic wave seperatly.

Evaluating the normal component first, using the fact that $n_i = n_d = n$ in an isotropic medium, leads to

$$\theta_i = \theta_d, \tag{2.68}$$

where θ_i and θ_d are the incident and diffracted angles with respect to the acoustic wave. Using this result when assessing Eq. (2.63) in the direction of the acoustic beam leads to

$$k_d \sin\theta_d = -k_i \sin\theta_i + k_a. \tag{2.69}$$

Inserting the relevant expressions for the respective wave numbers into Eq. (2.69) results in

$$\frac{n}{\lambda_0} \sin\theta_d = -\frac{n}{\lambda_0} \sin\theta_i + \frac{f_a}{v_a}. \tag{2.70}$$

Finally, using Eq.(2.68) leads to

$$\sin\theta_i = \frac{f_a \lambda_0}{2 v_a n}. \tag{2.71}$$

Eq.(2.71) implies that the incident and diffracted beam are no longer parallel in a non-collinear AOTF. Furthermore, the angle of which the incident beam is diffracted dependent on both the wavelength of the incoming EM-wave and the frequency of the acoustic wave.

In the case of a non isotropic medium, the treatment of the condition (2.63) changes once again. Using the law of cosines, the condition transforms to

$$k_a^2 = k_i^2 + k_d^2 - 2 k_i k_d \cos(\theta_i + \theta_d). \tag{2.72}$$

Eq. (2.72) may be solved for θ_i and θ_d. One again inserting the relevant expressions, transforms Eq. (2.72) to

$$\frac{f_a^2}{v_a^2} = \frac{1}{\lambda_0^2}\left[n_d^2 + n_i^2 - 2n_d n_i \cos\left(\theta_i + \theta_d\right)\right].$$

Rearranging this expression and defining $\Lambda = \frac{f_a}{v_a}$ results in

$$\frac{\lambda_0^2}{\Lambda^2} = n_d^2 + n_i^2 - 2n_d n_i[\cos\left(\theta_i\right)\cos\left(\theta_d\right) - \sin\left(\theta_i\right)\sin\left(\theta_d\right)], \tag{2.73}$$

and finally

$$\cos\left(\theta_i\right)\cos\left(\theta_d\right) - \sin\left(\theta_i\right)\sin\left(\theta_d\right) = \frac{n_d^2 + n_i^2}{2n_d n_i} - \frac{\lambda_0^2}{2n_d n_i \Lambda^2}. \tag{2.74}$$

From here, it is possible to substitute $a = k_d \sin\theta_d$, $b = k_i \sin\theta_i$, $c = k_i \cos\theta_i$ and $k_a = a + b$[38] and using that

$$\frac{k_d}{k_i} = \frac{n_d}{n_i} \quad \text{and} \quad \frac{k_a}{k_i} = \frac{f_a \lambda_0}{v n_i}$$

to rearrange Eq. (2.74) to the form

$$\begin{aligned} \sin\left(\theta_d\right) &= \frac{\lambda_0}{2n_d\Lambda}\left[1 - \frac{\Lambda^2}{\lambda_0^2}(n_i^2 - n_d^2)\right], \\ \sin\left(\theta_i\right) &= \frac{\lambda_0}{2n_d\Lambda}\left[1 + \frac{\Lambda^2}{\lambda_0^2}(n_i^2 - n_d^2)\right]. \end{aligned} \tag{2.75}$$

To choose the appropriate acoustic frequency one needs to know the incident angle, and set a desired diffracted angle for which one wants the desired output frequency of the EM-wave and solve for Λ in Eq. (2.75).

2.5 Detectors

Detection of photons is an important part of any measurements in optics and ellipsometry. To achieve this, photo detectors are needed. There are several different types of detectors that are used for such purposes, utilizing various physical phenomena to measure the incident light intensity. Among these are detectors that depend on the *photoconductive effect*. Here, the incident light interacts with a detector material, often a semiconductor such as silicon (Si) or germanium (Ge). If the energy for a given photon is higher than the band gap of the semiconductor, electron-hole pairs are created, thus reducing the resistance over the semiconducting material. Two metal plates with a voltage differential between them are put at either side of the semiconductor connected by circuitry, functioning as an anode and a cathode[39]. This produces a current proportional to the incident irradiance. A downside of this is the existence of a dark current when no light is incident, which must be taken into account when measurements are made. Figure 6 illustrates the basic design of such a photodetector. The effectiveness of the detector may also be enhanced by the *photo-gating effect*. Here, defects and impurities lead to trapped states in the semiconductor, further increasing the conductivity, resulting in a a greater photo current.

A photodetector has several important figures of merit. Firstly, the responsivity of the detector R is the ratio between the photocurrent and the incident optical power. Secondly, the time response

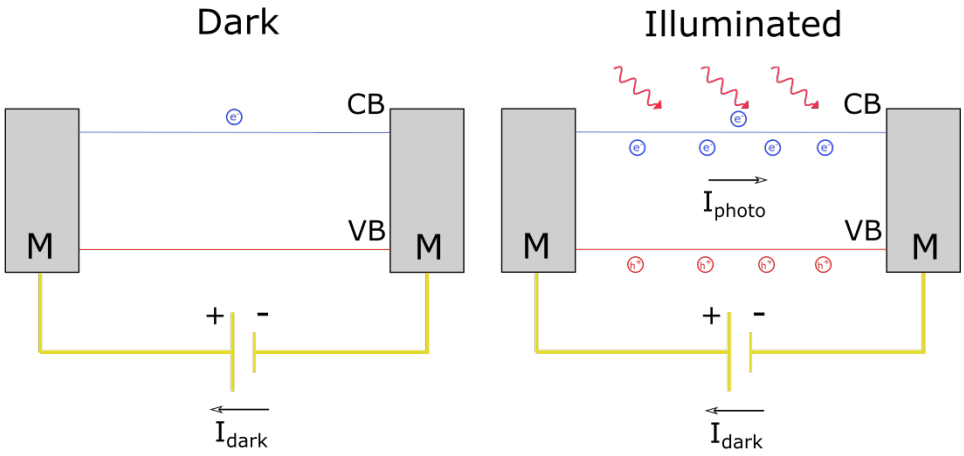

Figure 6: Basic schematic of a photoconductor between two metal contacts (M). CB illustrates the conduction band of the semiconductor while VB is the valence band. The left most image displays the conductor with no EM-radiation with a small dark current I_{dark}. The illustration to the right is the conductor where the incident photons have higher energy than that of the excitation energy of the semiconductor producing electron-hole pairs driving the photo-current. Adapted from[39].

of the detector is the time the generated signal spends between 10% and 90% of the maximum output during modulated input. Related to this is the bandwidth, which is the frequency at which a modulated signal produces a detector response 3 dB lower than that provided by continuous illumination. Lastly, the wavelength range indicating which part of the electromagnetic spectrum may be detected. The bandgap of the semiconductor is often the limiting factor of the wavelength range. All of these are dependent on the material used in the detector as well as the finer design details of the photodetector[40].

Ideally, any given photodiode will produce a current directly proportional to the incident EM-radiation. In reality, howvere, many detectors do not have a perfectly linear response. Rather, the current can be represented by

$$i(t) = P(t)R(a), \tag{2.76}$$

where $P(t)$ is the optical power incident on the diode, $R(a)$ is the nonlinear transfer function while $a = \gamma P(t)$, where γ is a constant[41].

2.6 Integrating Spheres

An integrating sphere is a device for measuring optical intensity. As the name implies, the integrating sphere is a hollow sphere with an internal surface of area A_s covered with a diffuse reflective coating of reflectance ρ. It also have small entrance and exit ports for incoming and outgoing EM waves with area A_i and A_e respectively[42]. It is also common that integrating spheres utilize a small wall, called a *baffle*, to prevent any detector attached to the sphere from acquiring a signal from a directly illuminated spot on the internal surface, as this will provide an incorrect result. A schematic illustration of a general integrating sphere is found depicted in Figure 7.

The main function of an integrating sphere is to spatially integrate light incident on the entrance port. This is done by repeated reflections on the diffuse surface inside of the sphere. The flux Φ_{tot} on the

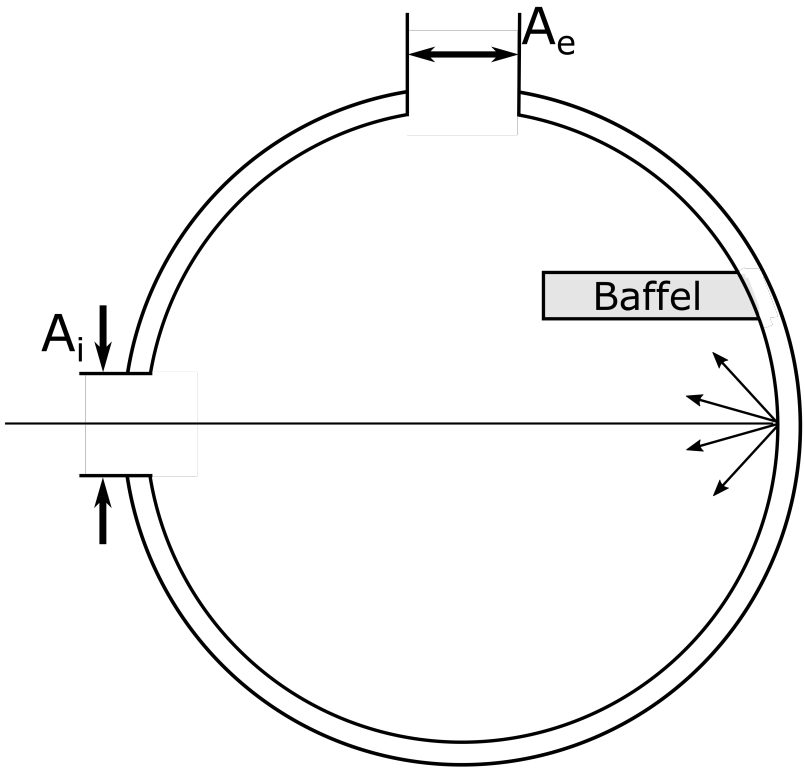

Figure 7: Schematic illustration of an integrating sphere. A_i and A_e are the entrance and exit port areas respectively. Incident EM-radiation enters through the entrance port and is scattered uniformly along the sphere. A baffle is present to ensure appropriate integration taking place through the process of repeated reflections internally in the sphere. The baffle size is exaggerated for illustrative purposes.

entire integrating sphere from the first reflection is related to the incident flux Φ_i as

$$\Phi_{tot} = \Phi_i \rho (1 - f), \tag{2.77}$$

where

$$f = \frac{A_i + A_e}{A_s}. \tag{2.78}$$

For the n-th concurrent reflection on the sphere, the total sphere will be illuminated as

$$\Phi_{tot} = \Phi_i \rho^n (1 - f)^n. \tag{2.79}$$

Assuming a steady illumination over a long enough period, so that the total optical flux in the sphere has reached equilibrium, one finds that the total flux of on the sphere may be expressed as a geometric series. The total sphere surface radiance may then be expressed as

$$L_S = \frac{\Phi_i}{\pi A_s} \frac{\rho}{1 - \rho(1 - f)}. \tag{2.80}$$

This result assumes that the reflectance is uniform at every point of the surface and that the surface contribution of the baffle is negligible. A coating may also be applied to the entrance port to minimize the flux lost through this, though this does also necessarily reflects away some of the incident EM-radiation.

If the incident flux is either pulsed or modulated, the output signal may be stretched in time [43]. This is due to the multiple diffuse reflections in the sphere. The resulting signal may be represented as

$$P_{out}(t) = h(t) * P_{inn}(t), \tag{2.81}$$

where $P_{inn}(t)$ and $P_{out}(t)$ are the incoming and outgoing optical power, and $*$ signifies a convolution integral as described in [44]. Furthermore, $h(t)$ is the response function of the integrating sphere, and may be estimated as

$$h(t) = e^{-\frac{t}{\tau_0}}, \tag{2.82}$$

where

$$\tau_0 = -\frac{2}{3}\frac{D_s}{c}\frac{1}{\ln\bar{\rho}}. \tag{2.83}$$

Here D_s is the diameter if the integrating sphere, c is the velocity in vacuum of light and $\ln\bar{\rho}$ is the average wall reflectance. τ_0 is, for typical integrating spheres, of the order of nanoseconds to tens of nanoseconds.

2.7 Generalised- and Pseudo-inverse

Before exploring the physical principles and the theoretical basis for the methods used to calibrate the ellipsometer, an introduction to the *pseudo inverse* is necessary. From standard linear algebra it is known that the matrix $\mathbf{A}$ is said to be invertible if there exists a matrix $\mathbf{A}^{-1}$ so that

$$\mathbf{A}\mathbf{A}^{-1} = \mathbf{A}^{-1}\mathbf{A} = \mathbf{I}, \tag{2.84}$$

where $\mathbf{I}$ is the identity matrix[17]. This is only the case if the matrix in question is a square matrix and is non-singular, meaning that every row or column is in the matrix is linearly independent. These conditions severely restricts which matrices may be inverted. A problem then arises if one wishes to solve an equation on the form

$$\mathbf{A}\vec{x} = \vec{y}, \tag{2.85}$$

where $\vec{x} \in \mathbf{R}^m$, $\vec{y} \in \mathbf{R}^n$ and $\mathbf{A} \in \mathbf{R}^{m\times n}$, as it is not possible to invert $\mathbf{A}$. A more general inverse is therefore in order. It has been shown that there exists at least one matrix X so that

$$\mathbf{A}\mathbf{X}\mathbf{A} = \mathbf{A} \tag{2.86}$$

for any matrix $\mathbf{A}$ [45]. Finding any $\mathbf{X}$ is not sufficient for solving the problem in Eq. (2.85), as there is no telling what solution is the best from this general, but simple criteria. It is therefore necessary to

introduce conditions that minimize calculation errors. One such set of four conditions was developed by E. H. Moore and later introduced by Roger Penrose. Denoted by † the *Moore-Rose pseudo-inverse*, meets the criteria

$$\begin{aligned} \mathbf{A}\mathbf{A}^\dagger\mathbf{A} &= \mathbf{A}, \\ \mathbf{A}^\dagger\mathbf{A}\mathbf{A}^\dagger &= \mathbf{A}^\dagger, \\ (\mathbf{A}\mathbf{A}^\dagger)^* &= \mathbf{A}\mathbf{A}^\dagger, \\ (\mathbf{A}^\dagger\mathbf{A})^* &= \mathbf{A}^\dagger\mathbf{A}. \end{aligned} \tag{2.87}$$

The Moore-Rose pseudo inverse may be approximated by using the formula

$$\mathbf{A}^\dagger = (\mathbf{A}^T\mathbf{A})^{-1}\mathbf{A}^T. \tag{2.88}$$

To determine $\mathbf{A}^\dagger$ accurately it is however necessary to use a numerical method like *Single Value Decomposition* (SVD).

If $m > n$ in Eq. (2.85), the system is said to be *overdetermined*. In this case, the matrix $\mathbf{A}^\dagger$ that minimizes the euclidean norm

$$\|\mathbf{A}^\dagger\vec{x} - \mathbf{A}\vec{y}\| \tag{2.89}$$

is the Moore-Rose pseudo-inverse. Doing this is equivalent to finding the least square solution of Eq. (2.85). It is also possible to quantify the degree of invertability by introducing the *condition number*, defined as

$$\kappa_A = \|\mathbf{A}\|\|\mathbf{A}^{-1}\|, \tag{2.90}$$

where

$$\|\mathbf{A}\| \equiv \max_{\|\vec{x}\|=1} \|\mathbf{A}\vec{x}\|, \quad \mathbf{A} \in \mathbf{R}^{m\times n}, \quad \vec{x} \in \mathbf{R}^n. \tag{2.91}$$

The condition number may range from 1 to infinity, where 1 implies that the matrix is invertible, while infinity implies that it is singular, meaning it is completely non-invertible.

2.8 Ellipsometry

Ellipsometry is an optical technique that measures the change in polarization of EM waves either reflecting off or transmitted through an object[5]. The main measured quantities are Ψ and Δ as defined in section 2.2. Using these, it is possible to determine the Mueller matrix of any given sample.

A general Mueller matrix ellipsometer is made using five parts, an EM-wave source, a polarisation state generator (PSG), a sample, a polarisation state analyser (PSA) and a detector. The PSG is used to set the incoming polarization state, while the PSA analyzes the resulting polarisation state after being reflected off, or transmitted through the sample. To determine a complete Mueller matrix, 16 intensity measurements per wavelength are necessary, composed of four separate PSG and PSA states.

There are several ways to build a PSG and a PSA. One is to let both be composed of a stationary linear polarizer and a rotating retarder. In the PSG, the polarizer is placed before the retarder, while the opposite is true for the PSA. This setup has been aptly named a dual-rotating-retarder (DRR) polarimeter, and a basic outline can be seen in Figure 8.

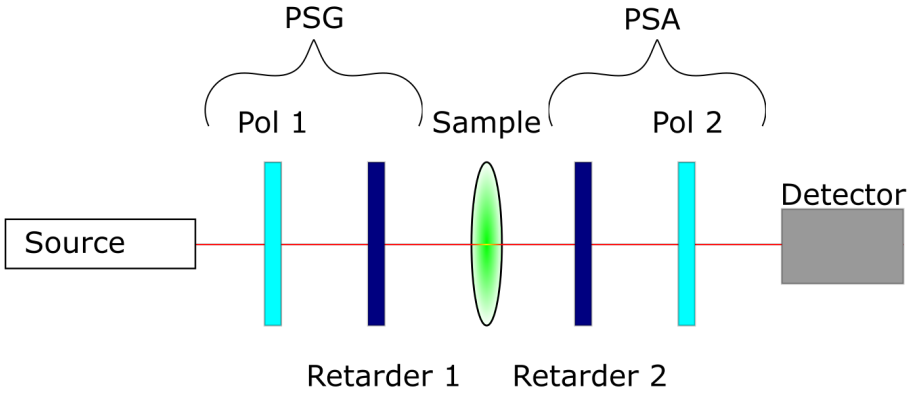

Figure 8: A simplified overview of the optical components of the DRR setup. Here the first polarizer (Pol1) and the subsequent retarder (Retarder 1) constitute the PSG of the system. The same components in reverse order constitute the PSA.

Within this framework of DRR polarimeters, there are still two broad approaches. One is the measurement matrix method, focusing on using linear algebra to isolate the Mueller matrix of the sample. The other is the Fourier method that uses Fourier expansion to determine the Mueller matrix [46]. This thesis will focus on the former.

Taking into consideration that both the PSG and PSA as well as the sample Mueller matrix affects the total intensity, one finds that any given intensity measurement may be expressed as

$$I = \begin{bmatrix} a_{00} & a_{01} & a_{02} & a_{03} \end{bmatrix} \mathbf{M}_{sample} \begin{bmatrix} w_{00} \\ w_{10} \\ w_{20} \\ w_{30} \end{bmatrix}. \tag{2.92}$$

Here, a_{0i} and w_{j0} are elements of the first row and column of the Mueller matrices for the PSA and PSG respectively. It is convenient to define the vectors

$$\vec{a}_n = \begin{bmatrix} a_{00} & a_{01} & a_{02} & a_{03} \end{bmatrix} \quad \text{and} \quad \vec{w}_m = \begin{bmatrix} w_{00} \\ w_{10} \\ w_{20} \\ w_{30} \end{bmatrix}, \tag{2.93}$$

where $\vec{a}_n$ and $\vec{w}_m$ corresponds to the n-th and m-th state of the PSA and PSG respectively. Assuming a total of N PSA and M PSG states, constructing the two *system matrices* $\mathbf{A}$ and $\mathbf{W}$ from the vectors in Eq. (2.93) is possible. These are of shape $N \times 4$ and $4 \times M$ respectively and are constructed as

$$\mathbf{A} = \begin{bmatrix} \vec{a}_0 \\ \vec{a}_1 \\ \vdots \\ \vec{a}_N \end{bmatrix} \quad \text{and} \quad \mathbf{W} = \begin{bmatrix} \vec{w}_0 & \vec{w}_1 & \dots & \vec{w}_M \end{bmatrix}. \tag{2.94}$$

Replacing $\vec{a}_n$ and $\vec{w}_m$ in Eq. (2.92) with $\mathbf{A}$ and $\mathbf{W}$ from Eq. (2.94) leads to

$$\mathbf{B} = \mathbf{A}\mathbf{M}_{sample}\mathbf{W}, \tag{2.95}$$

where $\mathbf{B}$ is a matrix of size $N \times M$ that contains all the intensity measurements I_{nm} as measured in the state n, m. The sample Mueller matrix may from here be found by inverting $\mathbf{A}$ and $\mathbf{W}$

$$\mathbf{M}_{sample} = \mathbf{A}^{-1}\mathbf{B}\mathbf{W}^{-1}, \tag{2.96}$$

The error of $\mathbf{M}_{sample}$ is determined by

$$\frac{\|\Delta\mathbf{M}_{sample}\|}{\|\mathbf{M}_{sample}\|} \leq \kappa_A \frac{\|\Delta\mathbf{A}\|}{\|\mathbf{A}\|} + \kappa_W \frac{\|\Delta\mathbf{W}\|}{\|\mathbf{W}\|} + \kappa_A\kappa_W \frac{\|\Delta\mathbf{B}\|}{\|\mathbf{B}\|} \tag{2.97}$$

where κ_A and κ_W are the condition numbers of $\mathbf{A}$ and $\mathbf{W}$ as defined by Eq.(2.90)[47]. It is therefore imperative that the condition numbers are as low as possible to minimize the error in $\mathbf{M}_{sample}$.It has been shown that the lowest physically possible value of the condition numbers of both $\mathbf{A}$ and $\mathbf{W}$ is $\sqrt{3}$[48].

To minimize the condition numbers of $\mathbf{A}$ and $\mathbf{W}$ it is necessary to determine the optimal rotational positions and retardence of Retarder 1 and Retarder 2. This is done by first finding a suitable model for the analysing and generating matrices and then calculating the condition number and finding the global minimum. In the case where only the 16 minimally required measurements are taken, it has been found that retarders with retardence 132° at the angles of ±51.7° and ±15.1° are optimal[49] for a DRR setup. This leads to the greatest amount of linear independence of the rows and columns of $\mathbf{A}$ and $\mathbf{W}$, which is illustrated in Figure 9.

2.9 Calibration Methods

To acquire satisfactory results for the MME, it is important that $\mathbf{A}$ and $\mathbf{W}$ are known to a great degree of certainty and that their condition numbers are low. It is therefore important to properly calibrate the instrument. In this thesis, two calibration methods will be explored. The first approach utilized intensity measurements and fit a model of the intensities to this directly. The second one utilizes linear algebra to mathematically find the optimal system matrices, called the eigenvalue calibration method (ECM).

2.9.1 Intensity Fit Method

The first calibration method discussed will be the intensity fit method. This is the mathematically simplest method as well as being the one most directly linked to the physics of the system between the two calibration methods presented in this thesis.

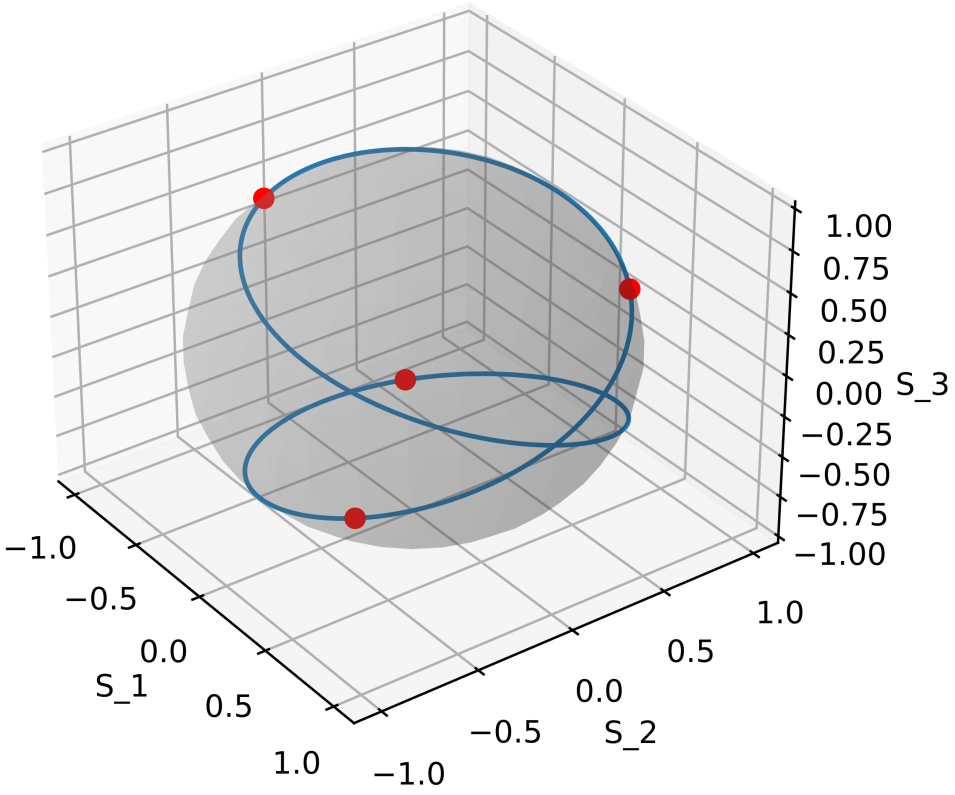

Figure 9: Points reached by a linear polarizer and a rotatable 132° retarder on the Point-Caré sphere as indicated by the blue line. The red dots on the line indicate the ±51.7° and ±15.1° rotations of the retarder, ideal for use in ellipsometry. Inspired by[49]

The method is based on modeling the optical components of the complete ellipsometer with free variables, e.g. rotation of the retarders in a DRR-setup. This model is then used to calculate $\vec{a}$ and $\vec{w}$ and by extension, using Eq.(2.92), the measured intensity. Comparing the model to recorded data makes it possible to find the values of the free variables that optimizes the model. The main benefit of this method is its simple mathematics and therefore ease of implementation. Increasing the complexity of the setup does however necessitate a more complex model. This means that this method is most beneficial if the setup is composed of few optical components, like that of a DRR-setup. If the system is too complex, it will get increasingly harder to model it sufficiently. Another drawback of this method of calibration is that it needs a high degree of precision in the alignment process as even small offsets may lead to appreciable deviations in a given model. Despite these shortcomings, the technique has been utilized to satisfactory results before[50, 51, 52].

2.9.2 The Eigenvalue Calibration Method

The Eigenvalue calibration method (ECM) was developed by Compain et al.[53]. This method has several advantages compared to other methods. Firstly, no assumptions are made about the system except that it is complete, that is to say it can generate and analyze any of the polarizations defined in the Stokes formalism. This automatically lessens the required precision in the alignment of the components of the MME, since these errors will be accounted for by the method. Secondly, the characteristics of the reference samples are determined completely during the calibration itself, meaning external measurements of the reference samples are in principle not necessary. Lastly, the accuracy of the calibration may be determined by the ECM itself.

The ECM is, however, subject to some constraints. First of all, the form of the Mueller matrix of the calibration samples must be known near perfectly in the wavelength-range desired. Secondly, more than one reference sample needs to be used, as the use of only one sample leads to four distinct possible solutions for the system matrices. There are also constraints in what combination of samples may be used, as they need to be sufficiently different from each other to produce an accurate calibration. These samples do not, however, depend on the MME-setup, and work equally well for all viable configurations.

As previously mentioned, the calibration requires several samples, each producing a different intensity matrix $\mathbf{B}_i$. It is convenient to let sample $\mathbf{M}_0$ be air so that $\mathbf{B}_0 = \mathbf{A}\mathbf{M}_0\mathbf{W} = \mathbf{A}\mathbf{W}$ and the rest $\mathbf{B}_i = \mathbf{A}\mathbf{M}_i\mathbf{W}$ were $\mathbf{M}_i$ refers to the i-th calibration sample matrix. These two equations may be used to construct the matrices

$$\begin{aligned} \mathbf{C}_i^W &= \mathbf{B}_0^\dagger \mathbf{B}_i = (\mathbf{A}\mathbf{W})^\dagger \mathbf{A}\mathbf{M}_i\mathbf{W} = \mathbf{W}^\dagger \mathbf{M}\mathbf{W}, \\ \mathbf{C}_i^A &= \mathbf{B}_i \mathbf{B}_0^\dagger = \mathbf{A}\mathbf{M}_i\mathbf{W}(\mathbf{A}\mathbf{W})^\dagger = \mathbf{A}\mathbf{M}\mathbf{A}^\dagger. \end{aligned} \tag{2.98}$$

C_i^W and C_i^A are, as implied by Eqs. (2.98), independent of $\mathbf{A}$ and $\mathbf{W}$ respectively. In the case where $N = M = 4$, the two sets of matrices share the same eigenvalues as M_i, measurement noise not accounted for. The eigenvalues of a general non-depolarizing Mueller matrix from Eq.(2.56) is on the form

$$\begin{aligned} \lambda_{r_1} &= 2\tau\cos^2\Psi, \quad \lambda_{r_2} = 2\tau\sin^2\Psi, \\ \lambda_{c_1} &= 2\tau\sin^2\Psi e^{-i\Delta}, \quad \lambda_{c_2} = 2\tau\sin^2\Psi e^{i\Delta}, \end{aligned} \tag{2.99}$$

where two of the eigenvalues are real and two are complex. Assuming that a total of 4 polarization states are used, it is possible to associate the eigenvalues of $\mathbf{C}_i^W$ and C_i^A with those of M_i.

Manipulating Eqs. (2.99) makes it is possible to determine several characteristics of the calibration samples used. Since the determinant does not depend on the order of matrix multiplication, the choice of which equation in Eqs. (2.98) is used is for the purpose of determining the characteristics of the reference samples, assuming no noise is present. Moving forward, the quantities defined in Eqs. (2.99) will be referred to by C_i as a shorthand[17].

It is easily obtained that the transmission coefficient of the retarder is

$$\tau_{ret} = \frac{1}{2}\left(\lambda_{ret\_r1} + \lambda_{ret\_r2}\right), \tag{2.100}$$

where λ_{ret_r1} and λ_{ret_r2} are the real eigenvalues as calculated for $\mathbf{C}_{ret}$. Likewise, the same quantity may be found for the polarizers using

$$\tau_{pol} = \mathrm{Tr}\{\mathbf{C}_{pol}\}. \tag{2.101}$$

The ellipsometric angle is determined by the relation

$$\Psi = \arctan\sqrt{\frac{\lambda_{r2}}{\lambda_{r1}}}, \tag{2.102}$$

and the retardence is found to be

$$\Delta = \frac{1}{2}\arg\left(\frac{\lambda_{c2}}{\lambda_{c1}}\right). \tag{2.103}$$

To determine the system matrices, it is necessary to first write Eq.(2.98) as

$$\begin{aligned} \mathbf{M}_i\mathbf{W} - \mathbf{W}\mathbf{C}_i^W &= 0, \\ \mathbf{A}\mathbf{M}_i - \mathbf{C}_i^A\mathbf{A} &= 0. \end{aligned} \tag{2.104}$$

From here, by transforming $\mathbf{A}$ and $\mathbf{W}$ to the vectors $\vec{a}^{4N}$ and $\vec{w}^{4N}$, it is possible to rewrite Eqs. (2.104) to

$$\begin{aligned} \mathbf{H}_i^W\vec{w}^{4N} &= 0, \\ \mathbf{H}_i^A\vec{a}^{4N} &= 0. \end{aligned} \tag{2.105}$$

To find $\mathbf{H}_i^A$ and $\mathbf{H}_i^W$, it is necessary to define the set of 4×4 matrices $\{\mathbf{U}\}$ where

$$\mathbf{U}_1 = \begin{bmatrix} 1 & 0 & 0 & 0 \\ 0 & 0 & 0 & 0 \\ 0 & 0 & 0 & 0 \\ 0 & 0 & 0 & 0 \end{bmatrix}, \quad \mathbf{U}_2 = \begin{bmatrix} 0 & 1 & 0 & 0 \\ 0 & 0 & 0 & 0 \\ 0 & 0 & 0 & 0 \\ 0 & 0 & 0 & 0 \end{bmatrix}, \quad \dots \quad \mathbf{U}_{4N} = \begin{bmatrix} 0 & 0 & 0 & 0 \\ 0 & 0 & 0 & 0 \\ 0 & 0 & 0 & 0 \\ 0 & 0 & 0 & 1 \end{bmatrix}. \tag{2.106}$$

Using these, it is possible to define

$$\begin{aligned} \mathbf{G}_i^{W1} &= \mathbf{M}_i\mathbf{U}_1 - \mathbf{U}_1\mathbf{C}_i^W, \quad \dots \quad \mathbf{G}_i^{W4N} = \mathbf{M}_i\mathbf{U}_{4N} - \mathbf{U}_{4N}\mathbf{C}_i^W, \\ \mathbf{G}_i^{A1} &= \mathbf{M}_i\mathbf{U}_1 - \mathbf{U}_1\mathbf{C}_i^A, \quad \dots \quad \mathbf{G}_i^{A4N} = \mathbf{M}_i\mathbf{U}_{4N} - \mathbf{U}_{4N}\mathbf{C}_i^A. \end{aligned} \tag{2.107}$$

Constructing $\vec{g}_i^W$ and $\vec{g}_i^A$ as the vector forms of $\mathbf{G}_i^W$ and $\mathbf{G}_i^A$ from Eqs. (2.107), it is possible to define $\mathbf{H}_i^W$ and $\mathbf{H}_i^A$ seen in Eqs. (2.105) as

$$\begin{aligned} \mathbf{H}_i^W &= \begin{bmatrix} \vec{g}_i^{W1} & \vec{g}_i^{W2} & \dots & \vec{g}_i^{W4N} \end{bmatrix}, \\ \mathbf{H}_i^A &= \begin{bmatrix} \vec{g}_i^{A1} & \vec{g}_i^{A2} & \dots & \vec{g}_i^{A4N} \end{bmatrix}, \end{aligned} \tag{2.108}$$

resulting in $\mathbf{H}_i^W$ and $\mathbf{H}_i^A$ being $4N\times 4N$ matrices. Using Eqs. (2.108), it is possible to construct a total measurement matrix that represents all the calibration samples

$$\begin{aligned} \mathbf{K}^W &= \sum_{i=1}^{N} \left(\mathbf{H}_i^W\right)^T \mathbf{H}_i^W, \\ \mathbf{K}^A &= \sum_{i=1}^{N} \left(\mathbf{H}_i^A\right)^T \mathbf{H}_i^A. \end{aligned} \tag{2.109}$$

Having defined $\mathbf{K}^W$ and $\mathbf{K}^A$, it is possible to find $\mathbf{W}$ and $\mathbf{A}$ by solving the over-determined matrix equations

$$\begin{aligned} \mathbf{K}^W \vec{w}^{4N} &= 0, \\ \mathbf{K}^A \vec{a}^{4N} &= 0. \end{aligned} \tag{2.110}$$

Solving Eqs. (2.110) would not be sufficient to accurately complete the calibration. The reason for this is because it is necessary to consider the azimuthal angle of the components used in the calibration. In contrast to many of the other sample properties, it is not possible to derive these directly from the measured intensity matrices or their eigenvalues. What is possible, however, is to use the fact that the sixteen eigenvalues of $\mathbf{K}^W$ and $\mathbf{K}^A$ should all be positive with a single zero-valued eigenvalue. In a real system with noise, the smallest eigenvalue will in general be non-zero, and their respective eigenvalues may be sorted as

$$\begin{aligned} \lambda_1^W > \lambda_2^W > \ldots > \lambda_{4n}^W \gtrsim 0, \\ \lambda_1^A > \lambda_2^A > \ldots > \lambda_{4n}^A \gtrsim 0. \end{aligned} \tag{2.111}$$

From here, introducing an angle dependency to the calibration samples $\mathbf{M}_i$ using Eq. (2.29) leads to angle dependence in $\mathbf{K}^W = \mathbf{K}^W(\alpha_1, \alpha_2, \ldots, \alpha_j)$ and $\mathbf{K}^A = \mathbf{K}^A(\alpha_1, \alpha_2, \ldots, \alpha_j)$. From here it is possible to estimate the angles θ_i by minimizing the ratios between λ_{4n} and the sum of the larger eigenvalues

$$\begin{aligned} \epsilon_W &= \frac{\lambda_{4n}^W}{\sum_{i=1}^{4n-1} \lambda_i^W}, \\ \epsilon_A &= \frac{\lambda_{4n}^A}{\sum_{i=1}^{4n-1} \lambda_i^A}, \end{aligned} \tag{2.112}$$

which will ensure the solution of Eqs. (2.110) are optimal.

Part II:

Method

Section 3:

Material and Software

Integral to the project was the components and software. In this section, all components and computer programs used in the project are presented.

3.1 Components and Parts

A sizeable part of the project utilized components from previous students and PhD candidates. Some were, however, custom made or ordered for this project.

3.1.1 Laser Source

One of the most important parts of any optical device is the illumination source. In this project, the source consisted of a supercontinuum laser[3] and a custom made wavelength selector.

Super continuum lasers, as discussed in section 2.3, emit a broad spectrum of EM-radiation. The laser used in this thesis emit a spectra between approxiamtly 400 to 2500 nm, as seen in Figure 10[54]. The total power of the source is 8 W, with a pulse width of 6 ps. Beyond this, the supercontinuum source also has a fundamental pulse repetition rate of 80 MHz and supports a range of repetition rates between 100 kHz to 80 MHz.

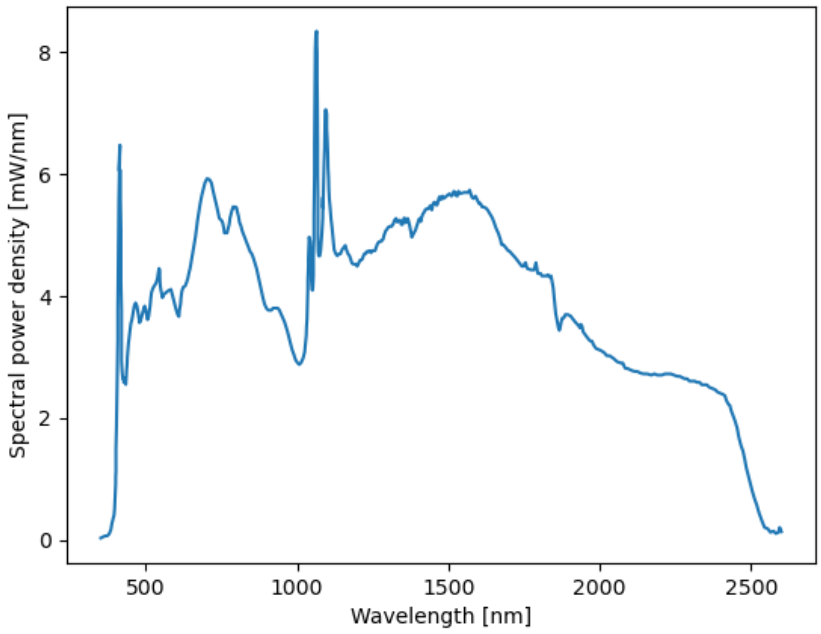

Figure 10: Power spectrum of Fianium WL-SC-400-8 supercontinuum source. The high spike at 1064 nm is due to the pump laser of the source. Credit: *Fianium UK Ltd.*

[3] *WL-SC-400-8 WhiteLase Super Continuum laser*, produced by *Fianium UK Ltd.*

For spectroscopic applications, it is also critical to control the wavelength of the output. To this end, a wavelength selection scheme designed and built by Per Magnus Walmsness was used. This setup, utilizing AOTFs[4], beamsplitters and a polarizer may be seen in Figure 11.

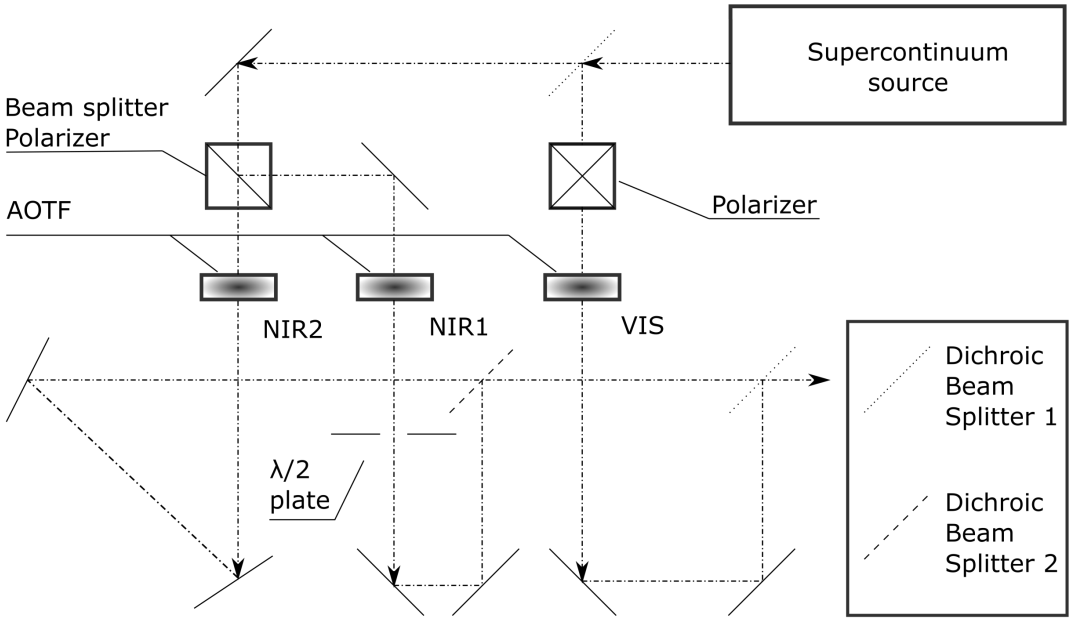

Figure 11: Schematic overview of the source. A supercontinuum laser is split using a dichroic beam splitter to differentiate between NIR radiation and visible light. The NIR portion of the spectrum is further split in two using a beam splitter polarizer. Each portion of the spectrum is then lead through an AOTF to select the desired wavelength and reunited before being sent off. A $\lambda/2$ plate is used to ensure the same polarization for all the beams when recombined. From left to right, the AOTFs have an effective wavelength range of 1100 to 2400 nm (NIR2), 670 to 1100 nm (NIR1) and 400 to 670 nm.(VIS)

The three AOTFs can span the entire spectra of the supercontinuum source and should retain the incoming laser's high spatial and temporal coherence with up to 90% diffraction efficiency, according to the producer. When the AOTFs are in an upright configuration, the outgoing light is horizontally polarized. Corresponding to their respective output wavelengths, the AOTFs will be referred to as NIR2, NIR1 and VIS following from left to right as they appear in Figure 11.

The beam splitters used in the source are dichroic ones, splitting the laser by wavelength[5]. Their transmission spectra are displayed in Figure 12. This ensures that VIS is provided with visible light while NIR1 and NIR2 are supplied with infrared radiation. Dichroic beam splitter 1 has a cutoff at around 662 nm, while beam splitter 2 has a cutoff at approximately 1064 nm.

3.1.2 Detectors

Apart from having a source to produce EM-radiation, it is also essential to have detectors to conduct measurements. Several types of detectors have been utilized in this thesis.

[4]Two sets of AOTFs were used in the design. First of which was a *AOTF-N1-D-FDS-MM Acousto-Optic Tunable Filter system*, similarly supplied by *Fianium UK Ltd.*, as can be seen as the box with two AOTFs in Figure 11. The third and separate AOTF is a *AOMO 3080-120* provided by *Gooch & Housego*. To communicate with the three AOTFs, three *AODS Synth DDS 8 CH* drivers from *Gooch & Housego* were used.

[5]Two models of beams splitters were used. Dichroic beam splitter 1 was a *FF662-FDi02-t3* provided by *Semrock*. Dichroic beam slitter 2 was a *DiO_2-R1064*, also provided by *Semrock*

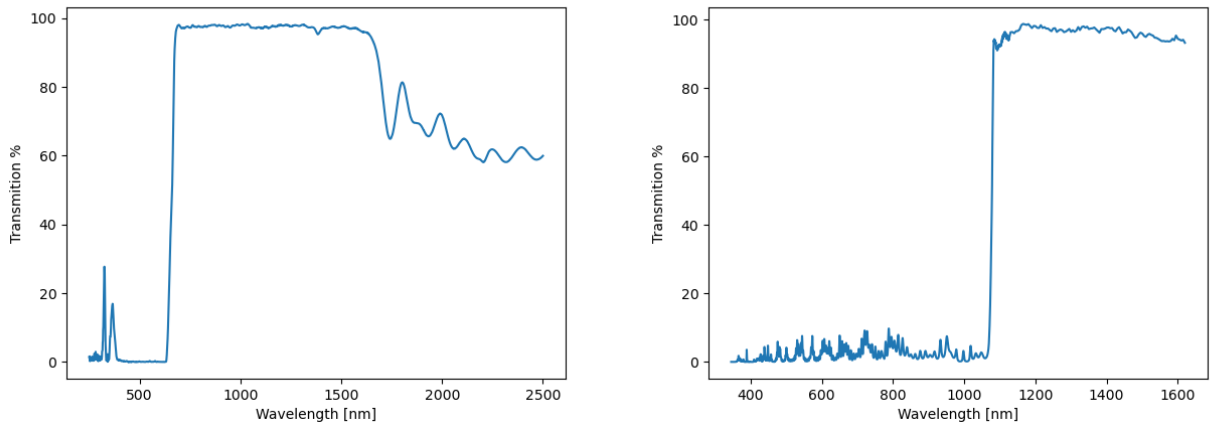

(a) (b)

Figure 12: (a) and (b) are the transmission spectra of dicroic beam splitter 1 and 2 respectively as reported from the producer.

Perhaps the most interesting detector to be used was a custom made pulse detector[6]. This detector was constructed to measure the total energy for a given light pulse of lengths up to 3 ns. The pulse signal is integrated twice, first in the silicon photodiode and then in the internal circuitry of the detector. A pulse shaper then forms an electric output pulse with a pulse height proportional to the number of photons detected and a length of about 11 ns. The output signal is limited to a maximum of 2 V with 4 mV of noise for a BNC-cablle with 50 Ω output impedance. The detector output was further customizable by selecting between different values of τ ranging from 1 to 7, influencing the shape of the emitted pulse.

To supplement the custom detector, a commercial pulse detector was also used[7]. This detector has a 2 GHz bandwidth with an effective wavelength range of 400 to 1100 nm with a maximum output voltage of 2 V.To accurately read out the detector signals, a 100 GHz oscilloscope[8] was utilized for this and the custom detector.

When fast detectors for pulse measurements were not needed, two slower detectors mounted to integrating spheres were used[9]. The response of this detector is displayed in Figure 13.

Finally, two spectrometers were used for calibrating and testing the bandwidth of the source[10]. The two spectrometers had a combined wavelength range of 250 to 1700 nm.

3.1.3 Ellipsometer Components

The ellipsometer setup was to be that of a DRR ellipsometer, as shown in Figure 8. To this end, two custom CaF_2 Fresnel prisms were used as retarders, as they were sufficiently achromatic with a

[6]Made by EMM

[7]*DET025A*-detector from *Thorlabs Inc.*

[8]*Infiniium DCA-X 86100D Wide-Bandwidth Oscilloscope* produced by *Agilent Technologies* borrowed from Erik Wahlstom, head of staff at the institute of physics at NTNU

[9]The detectors used were *UDT Model 221 Radiometric Sensor* coupled to *UDT Model 2500 Integrating Spheres, both provided by Gamma Scientific Inc. The detectors produced a current output so a PDA200C Photodiode Amplifier provided by Thorlabs Inc. was necessary. To record the data from these detectors, a NI SCB-68 shielded I/O connector terminal block connected to a NI PCI 6259 Multifunction I/O Device used as a digital to analogue converter (DAQ).*

[10]The spectrometers used were a *NIRQuest* and *Ocean Optics USB4000-UV-VIS Spectrometer*, both provided by *Ocean Insight.*

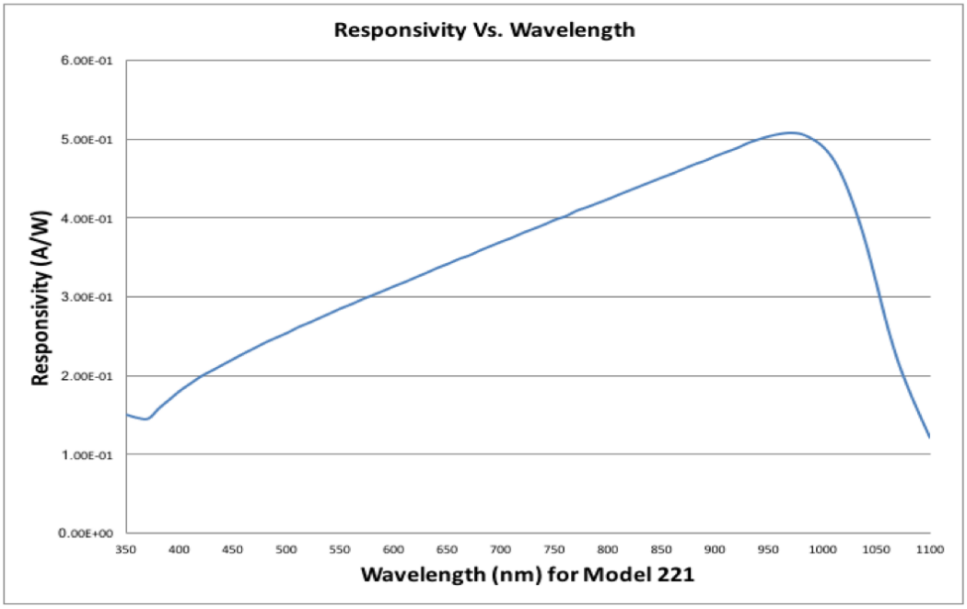

Figure 13: Reported response of the UDT Model 221 Radiometric Sensor. Credit: Gamma Scientific

retardance of approximately 132° in the desired spectral range of 400 to 1100 nm[11]. The prisms were mounted on a custom made holder attached to a step motor[12]. Furthermore, the polarizers[13] were mounted on manually rotatable holders.

3.1.4 Calibration Samples

Two sets of calibration samples were used. Common amongst both of them was the use of air. The first set was previously used in the thesis[56], consisting of two plate polarizers placed at horizontal and vertical positions, and a waveplate with appropriate retardence in the wavelength range of 800 − 1000 nm, aligned at 49°. These were all placed in an automatic filter wheel[14].

The second set of samples consisted of a prism retarder similar to the ones used in the ellipsometer setup and a Glan-Thomson polarizer, both mounted on a rotatable holder. Due to space concerns, these two samples were not mounted on a filter wheel. To ensure that the samples were placed correctly for repeat calibrations a rail system was constructed.

3.2 Software

All instrumentation, including controlling the PR50-motors, the AOTFs in the source, and data recording, was done using *National Instruments LabVIEW 2021*. The calculations associated with the eigenvalue were made using a Matlab program, written by Franz Stabo-Eeg[56], updated to fix compatibility issues with *Matlab R2021b*. Further calculations, as well as all plots, were made using *Python 3.8.8*. Several python libraries were used for this, including *numpy*, *pickle*, *sympy*, *matplotlib*, *scipy* and *lmfit*.

[11] Detailed explanation of the design of these prisms are found in [55]

[12] *PR50motor* provided by *Newport Cor.*, which were controlled using a *ESP301-3N* motion controller, also supplied by Newport.

[13] *Glan Thomson* polarizing prisms supplied by *B.Halle Nachfl. GmbH*, suitable for applications between 250 to 2700 nm

[14] Provided by *Thorlabs Inc.*

The program controlling the calibration for the Eigenvalue method is representative of the GUIs used for most of the programs made for the purpose of this thesis. The GUI of the program is seen in Figure 14. The angle of the prisms in the PSG and the PSA are defined in a). b) describes the data path for the B-measurements, the resultant Mueller matrix location and the graph of this data. c) defines the address for communicating with the step motors, while d) defines the specifics of the wavelength range of a scan. e) shows the error status of the program and is used for debugging when issues arise. f) is the part unique to the calibration program, indicating which sample has been measured and specifying how the calibration calculation should be performed.

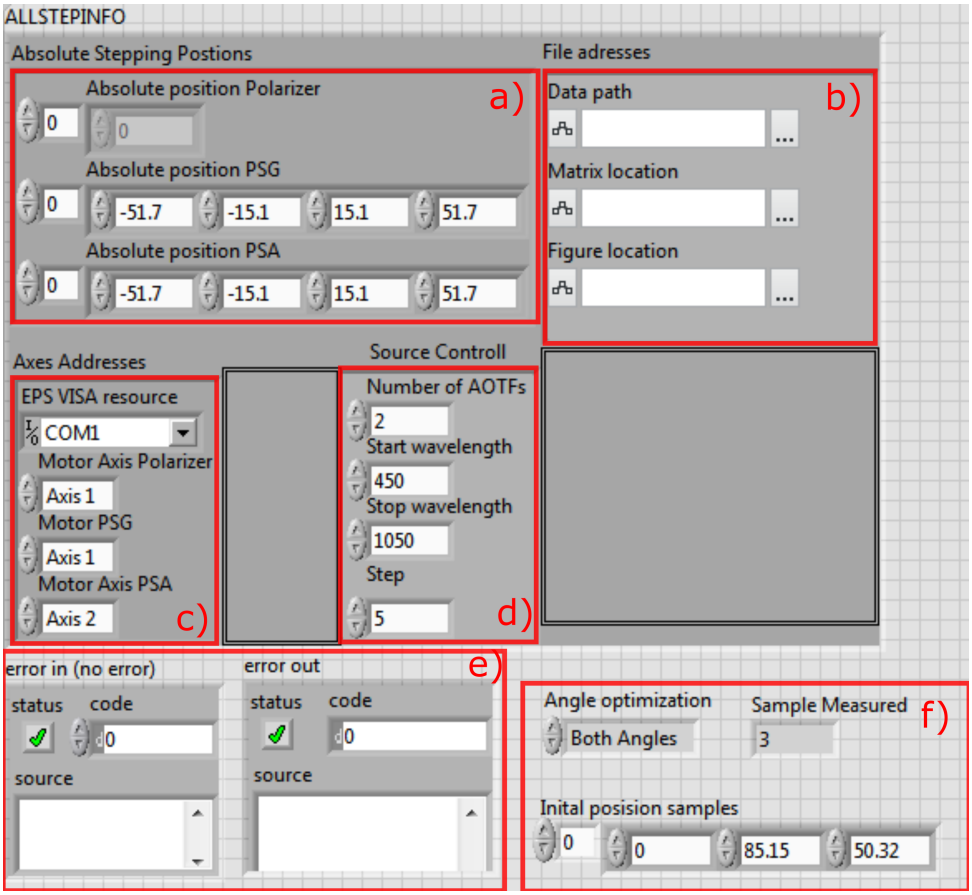

Figure 14: The GUI of the LabVIEW program used to do the calibration measurements.

For designing custom components and parts for the final scatterometer, *Solidworks 2020* was used.

Section 4:

Experimental

A Mueller matrix scatterometer consists of many parts which need to be understood to produce a satisfactory response. In this section, the experiments to determine the best design; and procedure for constructing this device is detailed.

4.1 Calibrating and Testing the Source

The AOTFs were calibrated. This was done by tuning each of the AOTFs to known acoustic frequencies and recording the resulting output spectrum using spectrometers. The wavelength of the output was set to be the wavelength with the highest photon count. Forth order polynomial regressions were then performed based on the results. The results from the calibration were then tested to verify the veracity of the calibrations.

After completing the calibration the relative intensity of the source was investigated for the wavelength range of 400 to 1100 nm. The test was performed, using the integrating spheres as detectors, with a 5 nm step length. The total intensity and the signal to noise ratio as a function of wavelength was found. This was done by performing 2500 measurements at a sampling rate of 250 kHz at every wavelength. The average value of these was set to be the reported measured intensity, while the standard deviation was set to be the uncertainty of the measurement.

The switching speed of the AOTFs was then tested by scanning of a portion of the spectrum as rapidly as possible. The results also served a dual purpose of giving insight into the time needed before the signal became stable after a frequency shift had occurred. This information was used to determine the time delay necessary between the switching of the AOTF taking place and the intensity data being recorded.

Lastly, the source's temporal stability was tested by taking measurements every minute for 9 minutes. There were a total of 4 measurement series, each with different conditions. First and foremost, the stability was tested with and without the laboratory being illuminated. The effect of warm-up of the supercontinuum source was also assessed by performing measurements immediately after being turned on and after 20 minutes of warm-up. Every measurement lasted 5 ms with a sampling rate of 250 kHz.

4.2 Characterization of the Laser Pulses

The use of pulsed sources in a spectroscopic Mueller matrix scatterometer is unconventional as pulsed lasers are associated with noise and non-linear effects in detectors due to the high instantaneous intensities[57, 58]. To evaluate the usage of such a source, the characterisation of the laser pulses was necessary. These tests were all done with a wavelength output of 633 nm from the source.

Pulse measurements were conducted using the two fast detectors. For the custom detector, repetition rates of 5, 10, 20, 40 and 80 MHz with pulse shaper settings of $\tau = 1, 2, 4$ and 7 were explored. Due to limitations in the resolution of the oscilloscope, only repetition rates of 20, 40 and 80 MHz have been considered for the ThorLabs detector.

One proposed way of conducting measurements for the scatterometer was to use the individual laser pulses. Using the custom detector to do this was no problem, as it was designed to measure the total

intensity of an incident laser pulse.

The Thorlabs detector was not constructed with intensity measurements in mind, so two ways of measuring the intensity using this detector were explored. The first exploited the fact that the Thorlabs detector was too slow to resolve the pulses from the source.

The Thorlabs detector was not constructed with intensity measurements in mind, so two ways of measuring the intensity using this detector were explored. The first exploited the fact that the Thorlabs detector was too slow to resolve the pulses from the source. It is known that the response $x(t)$ to a signal $y(t)$ of a measurement system is

$$x(t) = h(t) * y(t), \tag{4.1}$$

where $h(t)$ is the response function of the system[59]. When $y(t) = a\delta(t)$, one finds that the response should be

$$x(t) = ah(t), \tag{4.2}$$

i.e. proportional to the number of photons in the incident pulse. The second proposed way was to integrate the incident laser pulses. To do this, it was necessary to broaden the laser pulses, for which the integrating spheres were used. To measure the broadened pulses, the Thorlabs detector was mounted to a cage system fixed to the exit port of the integrating sphere. The outgoing irradiance from the integrating sphere was focused on the detector seen in Figure 15. To compensate for the cage system not being completely centred with respect to the detector, a makeshift two-axis stage was made internally in the cage system. The same setup was used with the custom detector for the sake of thoroughness.

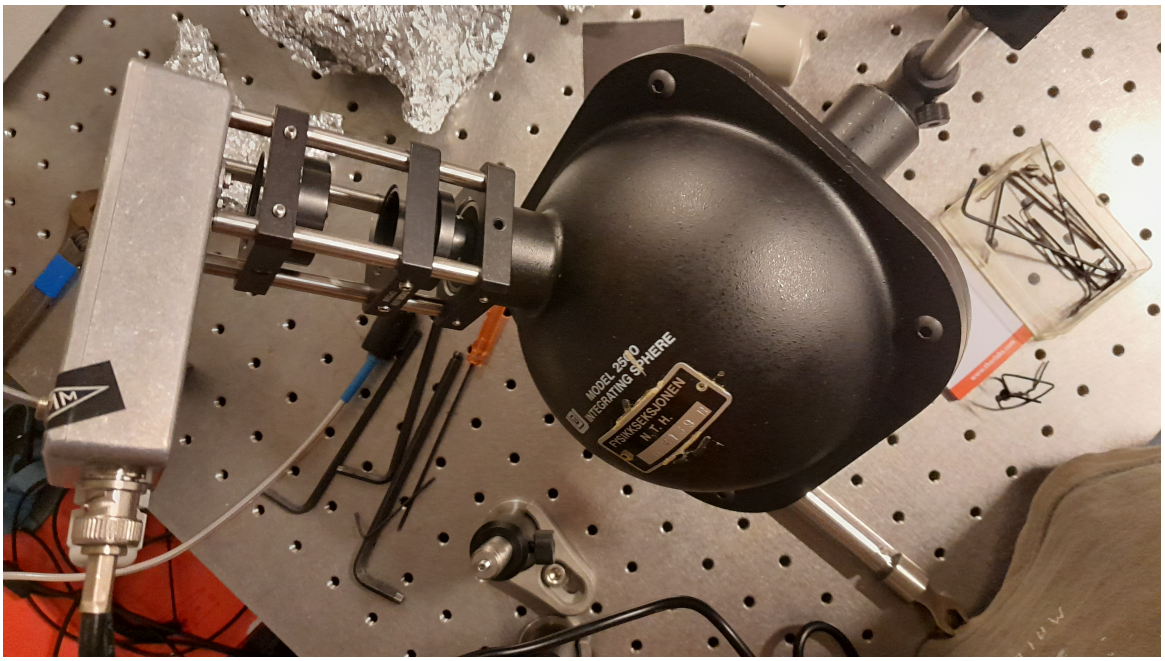

Figure 15: Picture of the custom detector mounted to an integrating sphere using a rail system. Two lenses are also mounted on the sphere as to focus down the beam on the detector.

4.2.1 Non-linearity Measurements

The detectors were now tested for non-linear responses. This was necessary due to the supercontinuum source used being a pulsed laser. The tests were made by using two linear polarizes. The first was set to a stationary azimuthal angle while the second one was rotated at increments of 5°. Using Eq. (2.33), the expected results from such a setup is

$$I \propto \cos^2(2\theta - \phi_0), \tag{4.3}$$

commonly known as Malu's law[60]. ϕ_0 is here a constant phase shift. If the detector response is linear, the relation in Eq.(4.3) will hold, as implied by Eq. (2.76). To determine how closely the measured intensities followed Malu's law, a curve fit was performed, and the coefficient of determination was found.

4.2.2 Transmission Measurements

Finally, to evaluate the viability of using the pulse detectors and the integrating sphere detectors for use in ellipsometry, it was necessary to determine to which degree each of these detectors sets was capable of measuring transmission accurately. In these tests, the transmittance of three neutral density filters (NDF) was measured using direct pulse measurements and the integrating spheres.

For the transmission measurements based on pulse measurements, the standard ThorLabs detector was used as a reference, while the custom detector was used as the main detector. To account for the two detectors being different, it was first necessary to determine the ratio of the output between the two detectors. This lead to the transmission being determined as

$$T = \frac{I}{I_0}\frac{R_0}{R} = \alpha\frac{I}{R}, \tag{4.4}$$

where I and I_0 are the measured intensity with and without the sample for the main detector, while R and R_0 are the corresponding values for the reference detector and T being the transmittance. α is then the relative intensity values between the detectors.

Each measurement of T was performed by measuring 32 separate pulses. The average amplitudes of these laser pulses were used to measure the transmitted intensity. Each sample was measured four times to determine the variation of the results. The measurements were later repeated using the integrating spheres as detectors with an equivalent setup to the pulse detectors, calculating the transmission utilizing Eq. (4.4).

4.3 Mueller Matrix Ellipsometer

Based on the results of the previous test, the ellipsometer setup to be used in the scatterometer was assembled and tested. First, the components of the ellipsometer were assembled along a predefined laser line. Then an NDF was placed before the first polarizer, serving a dual purpose; lowering the intensity to not damage the detectors, in addition to diverting some of the laser beam to a reference detector. Due to the results of the preliminary tests, the integrating spheres were chosen to be the detectors used for the final setup. The integrating spheres were placed at an angle to prevent back reflections into the ellipsometer system.

After the ellipsometer was properly lined up, the intensity fit method outlined in section 3.2 was

attempted 2.9.1.

To achieve the best possible result, it was determined that it was beneficial to survey as many polarization states as possible. To achieve this, the retarders in the PSA and the PSG were rotated at a fixed ratio PSA:PSG. Vap et al. discovered that a PSA:PSG rotation ratio of 37.5:7.5[46] was beneficial for ellipsometry using quarter wave plates, so this ratio was also used for this calibration method. The model to be used was determined using the measurements from a single wavelength (633 nm). When the model seemed satisfactory for this wavelength, a small selection of the total spectrum ($400 - 650$ nm) was evaluated in the same way. For each wavelength, a total of 50 states were evaluated. The best model for describing the system is showcased in section 7.1 in the results part of the thesis. The sample rate and number of samples, and wavelength step were the same here as for the tests of the spectrum in section 4.1.

After this, the eigenvalue calibration technique was performed. First, the pre-made samples installed in the filter wheel were characterized using a separate ellipsometer[15]. The test calibration was then made for a wavelength regime of 800 to 1000 nm, as this was the wavelength range where the samples were expected to give good results. Following the results from this calibration, smaller improvements detailed in the results section were made.

Comparing the results between the two calibration methods led to the conclusion that the eigenvalue calibration was the preferred method. Because of this, the calibration was extended into the visible part of the spectrum using two new calibration samples, detailed in section 3.1.4 with the eigenvalue calibration method.

4.4 Scatterometer Design

The design process of the scatterometer went parallel to that of the rest of the thesis. The basic outline of the design was originally proposed by Per Magnus Walmsness. This design was subsequently improved upon and the results are displayed in Figure 16.

A central dowel constitutes the spine of the scatterometer. Fastened at the base, it allows for simple adjustments in height of the central structure. Mounted to the base is the step motor controlling the arm designed to host the plate holding the PSA optics. This plate is not displayed in Figure 16 , as a preexisting plate was used. Further up, attached to the dowel for adjustable height and independent rotation with respect to the arm is the mounting piece for the sample holder. This sample holder is not shown in Figure 16 either due to the manufacturer not providing a CAD file of the sample holder. The design of the scatterometer is also modular so that adjustments may easily be made should it become necessary in the future.

4.5 Testing the Scatterometer

The scatterometer outlined in the previous section was then assembled. To test it, both beams from a beam splitting polarizer were measured. A square metasurface with sides 650 µm detailed in the thesis of fellow master's student Niklas Schwartz was tested. This surface is intended to split an incident beam into circularly left and right polarized EM-waves at an angel of approximately $\pm 6°$ at 950 nm. The metasurface was highly wavelength dependent, so the scatterometer was calibrated for a wavelength range of 800 to 1050 nm.

As the parts of the scatterometer were delivered close to the deadline of the thesis, the measurements were taken manually, as developing software to automatize these would take too long to complete

[15] *RC-2* provided by *J.A. Woolam*

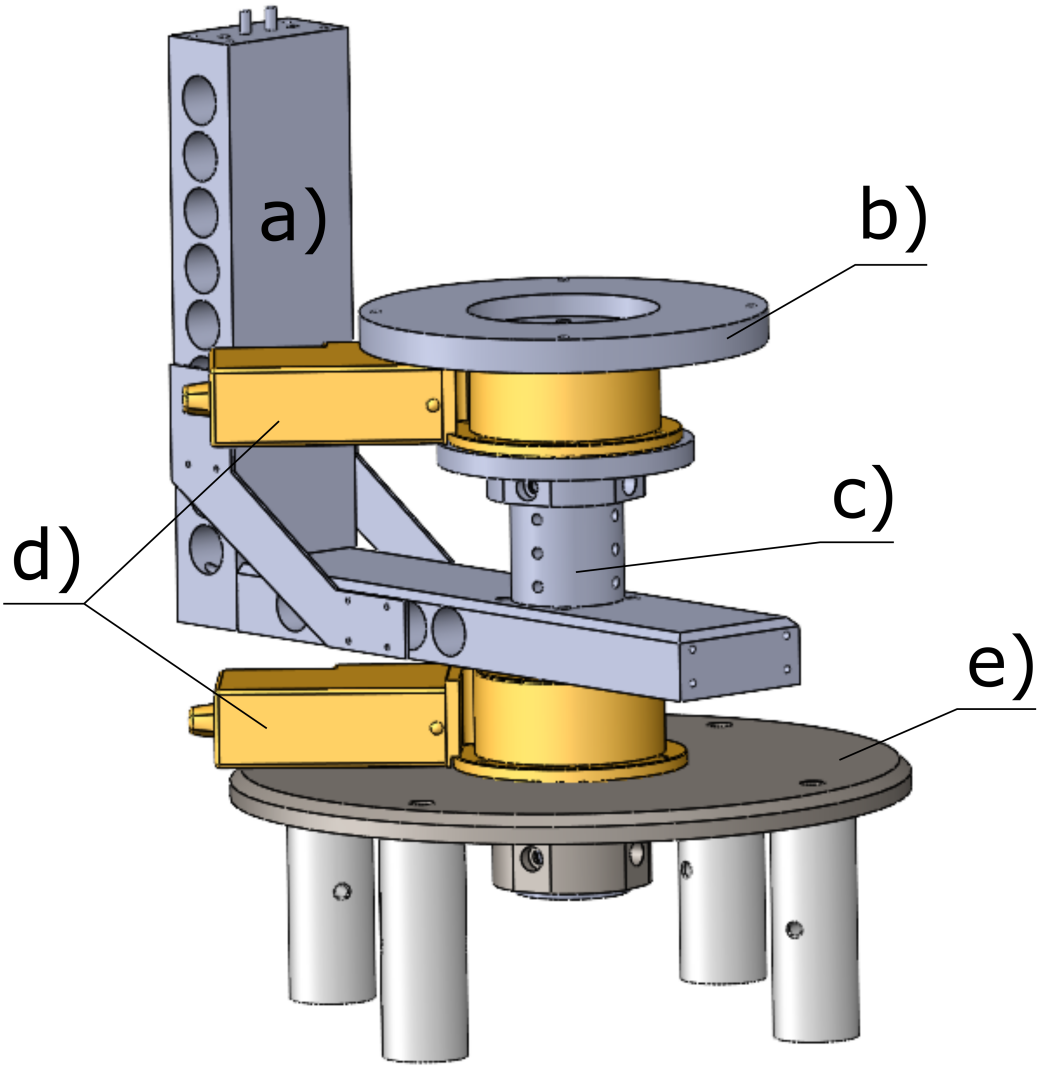

Figure 16: Basic design of the scatterometer. a) is a rotatable arm to which the PSA is planned to be attached. The arm consists of three components, a vertical and horizontal arm as well as bracers to help with stability. b) is the mounting piece for the sample holder, c) is the a adjustable dowel fastened in e). Lastly the scatterometer uses two *RVS80CC* step motor indicated by d).

before the deadline for the thesis.

Part III:

Results and Discussion

Section 5:

Testing the Source

When designing and building a complex system such as a Mueller matrix scatterometer, a fundamental understanding of each component and procedure beforehand is tantamount. This section is committed to showcasing the results from the investigation of the source intended for use in the scatterometer.

5.1 Calibration of AOTFs

The results from the AOTF calibrations are displayed in Figure 17. Here the AOTF frequency and the output wavelength seem to be following an inverse proportional relationship, which is the result predicted in Eqs. (2.75). Encouragingly, one can see that the curve fit for all three AOTFs closely follows the measured values, indicating a good model.

An excerpt of the post-calibration spectroscopic measurements may be seen in Figure 18. The bandwidth of the output from the source ranges from 2 to 5 nm, where the bandwidth of the spectrum is defined to be half or more of the peak intensity. It was found that the peak intensities match well the desired wavelength, all being within the bandwidth of the source. As can be seen, the peaks are not perfectly smooth for the VIS AOTF. Especially for the pulse set at 633 nm. diverge significantly from the expected form. This may indicate some form of defect in this particular AOTF. Further supporting this is the fact that the harmonics are asymmetrical. The harmonics do, however, not expand the bandwidth of the source, indicating this should not be a problem in future measurements.

A sweep of the spectrum from 400 to 1100 nm was conducted, and the results are displayed in Figure 19. The measured intensities in the visible part of the spectrum are higher than in the NIR part of the spectrum. This result was unexpected as the NIR part of the spectrum is reportedly where the intensities were to be highest. A reasonable explanation may be that the beams coming from the NIR1 AOTF and the VIS AOTF are not perfectly aligned. It may also be the case that a difference in beam diameter between the two AOTFs may contribute to an unequal amount of irradiance passing through the system. A final potential reason for this unexplained phenomenon might also be that the half-wave plate used to convert the vertically polarized light from the NIR1 AOTF to horizontally polarized light to match the other two AOTFs' polarizations is not correctly aligned. This explanation seems unlikely, as the orientation of the half-wave plate has been checked and verified several times.

The results in Figure 19 also gave insight into the spectral range of the source. The VIS AOTF was found to effectively be able to produce an output from 430 to 660 nm. NIR1 turned out to have an effective range of 670 to 1060 nm. NIR2 was not tested for two reasons; firstly, the available detectors were not capable of measuring beyond 1100 nm and secondly, problems with the AOTF itself occurred during testing. The results then indicate a final effective output range of the source to be between 430 and 1060 nm with a small unaccounted for gap in the spectral range between 660 nm and 670 nm. This was not unexpected, as one of the dichroic beam splitters used in the source had a cutoff around this wavelength area. It was therefore necessary to extend VIS to accommodate this wavelength range to not have any holes in the spectrum. Measurements in this range are then expected to be inaccurate due to low intensities, making the system more susceptible to random noise. This is corroborated by the findings in section 7. A potential solution to remedy the problems caused by this gap in the spectrum is presented in section 7.2.

The inverted signal to noise ratio of the source is shown in Figure 20. The signal to noise ratio is

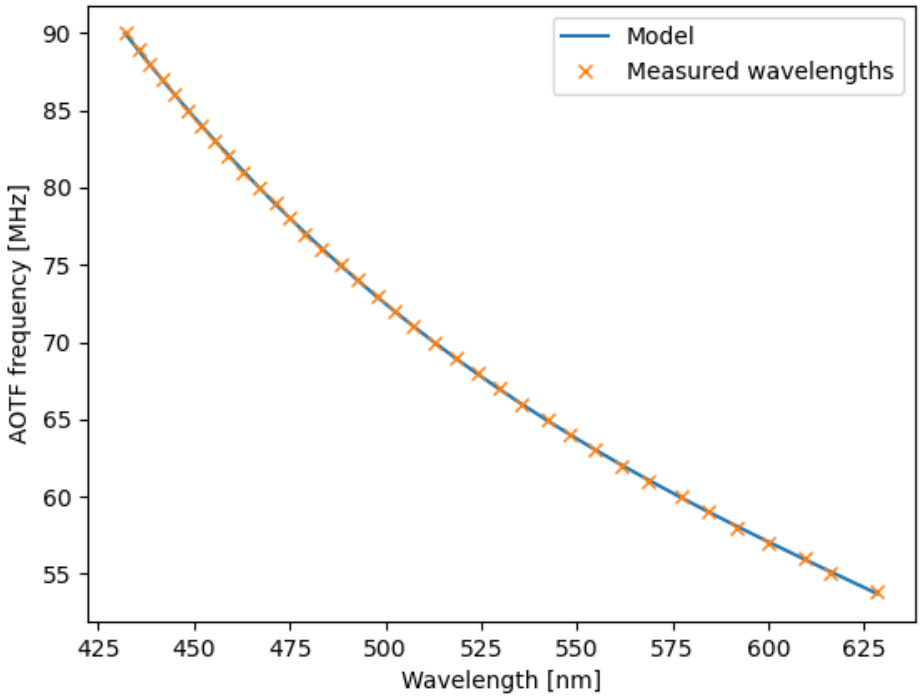

(a) VIS AOTF.

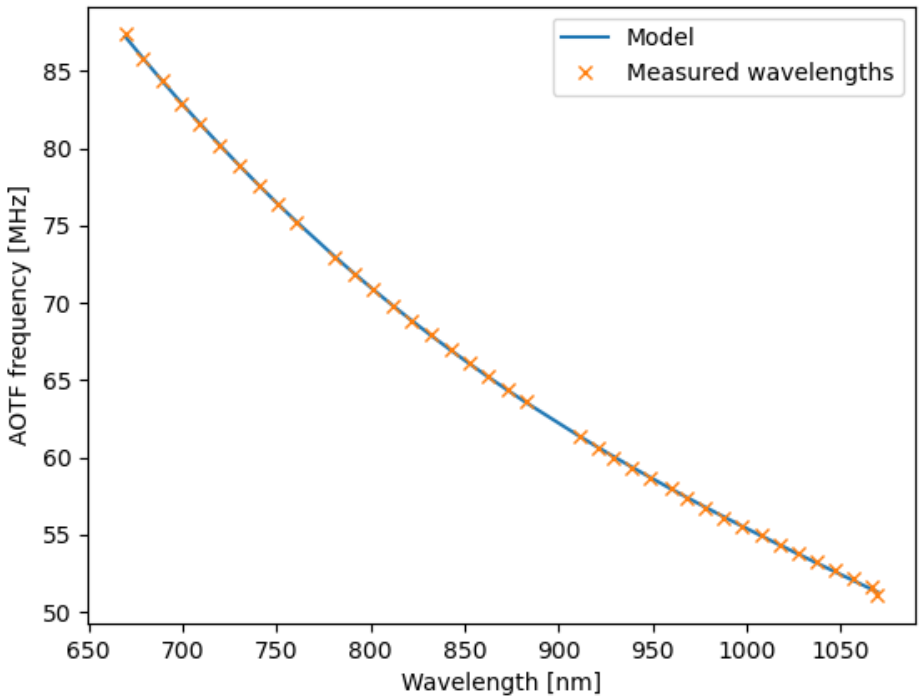

(b) NIR1 AOTF

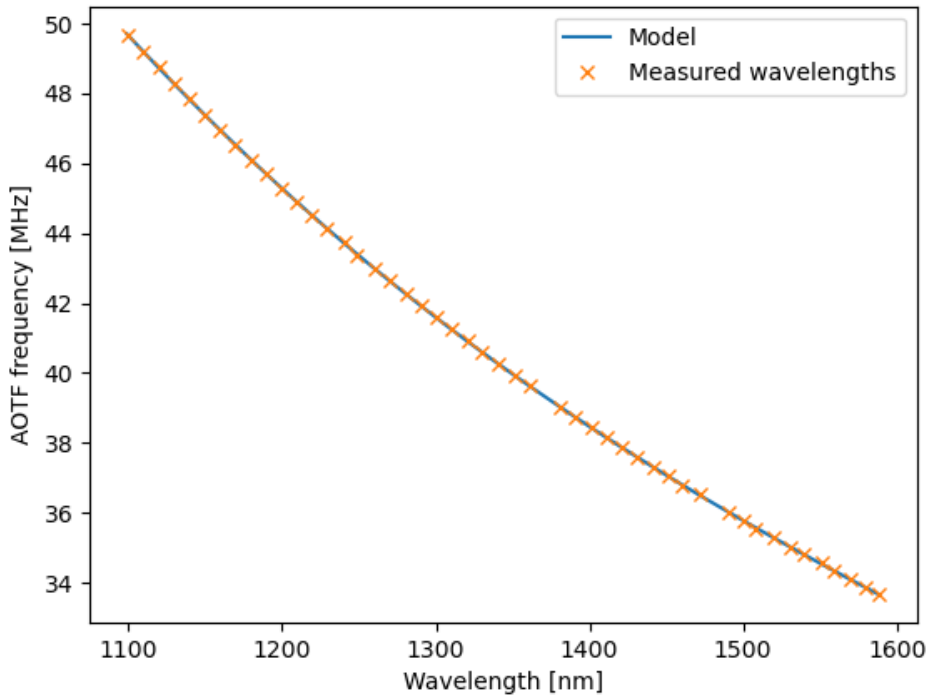

(c) NIR2 AOTF.

Figure 17: Measured wavelength output from the three AOTFs plotted against the acoustic frequency plotted using yellow crosses. The curve fitted model derived from these measurements are indicated by the blue lines.

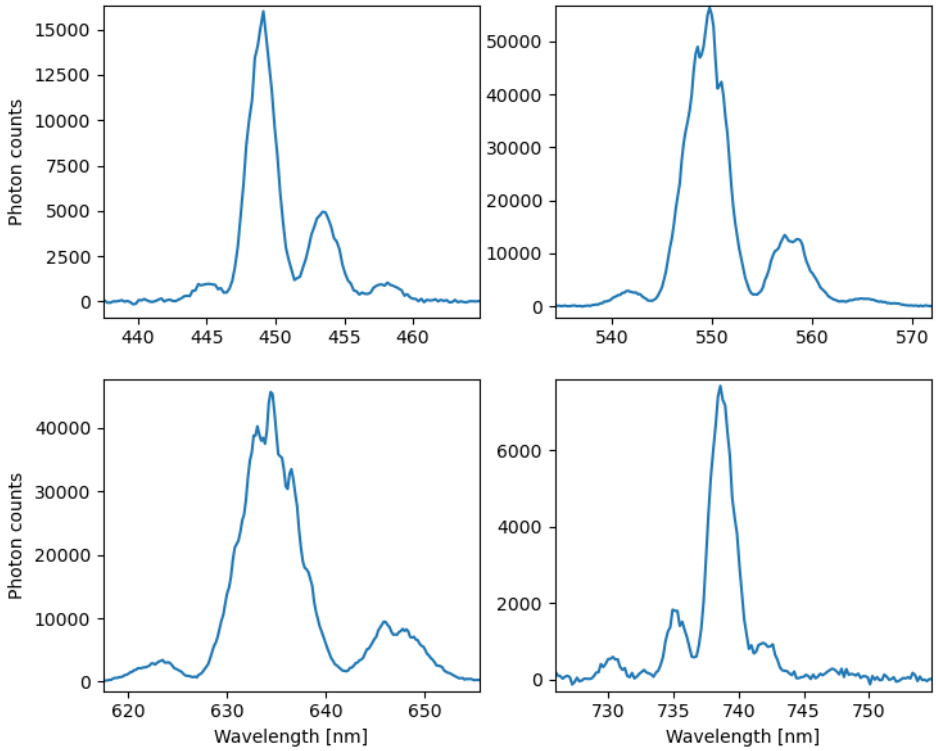

Figure 18: Measured spectrum of select wavelength output from the AOTFs.

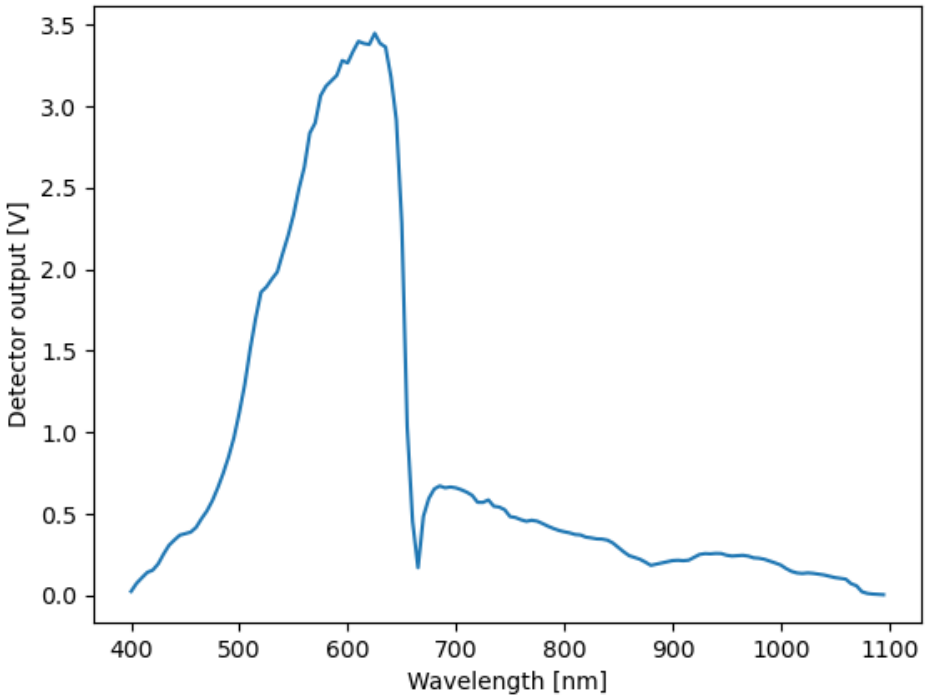

Figure 19: The measured intensity of the source.

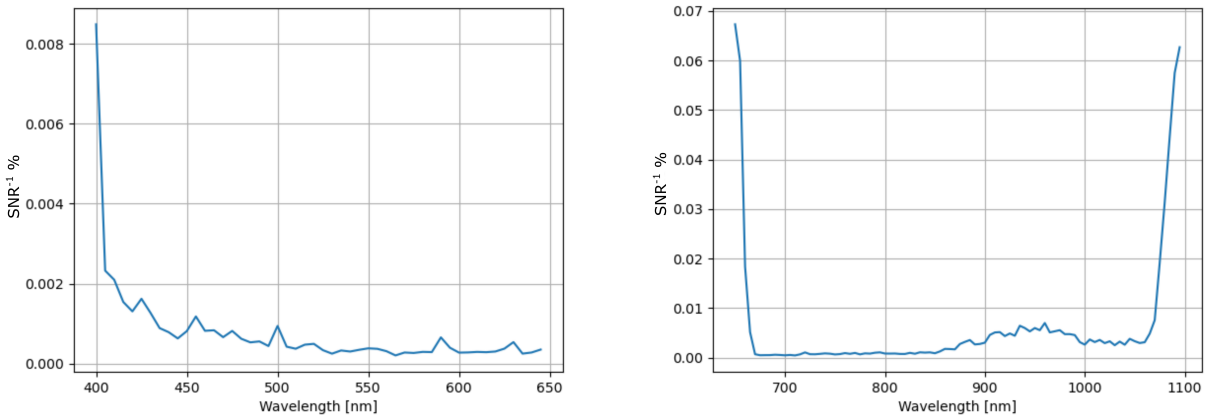

(a) (b)

Figure 20: The inverted signal to noise ratio for (a) the visible portion of the spectrum, and (b) the NIR part of the spectrum.

an order of magnitude greater in the visible region compared to the NIR region. Considering the relative difference between the two regions makes these results expected, as a higher intensity reduces the impact of thermal noise, which is assumed to be dominant. It is, however, clear that neither of these regimes has an unacceptable level of noise associated with them. This difference is, however, not irrelevant as can be seen by results from section 7.

The AOTF switching speed was determined to be approximately 80 ms as seen in Figure 21. This meant that scanning through the entire spectra would take tens of seconds, which was an unacceptable amount of time, as this would make the scatterometer excruciatingly slow to the point of non-usability due to the necessity of scanning through the spectra several times. An appreciable amount of time and effort was put into improving the switching speed with little luck without producing any results. The attempt to make the scanning was therefore abandoned for a long time to focus on other parts of the project. It was not until near the end of the project before an inefficiency in the code was found and fixed, which sped up the switching speed by an order of magnitude to around 4 ms. When switching between different AOTFs, a delay of 20 ms was found between the first AOTF being turned off and the second AOTF activating.

The stabilization speed of the AOTFs was determined to be less than 1 ms. Despite this, however, it was found that a delay of 10 ms between the switching signal being sent from the computer to the AOTF driver and intensity data being recorded was ideal. This is most likely due to communication between the computer and the driver controlling the AOTFs taking some additional time.

5.2 Source Stability and Warm-Up Time

Table 1: Intensity stability of supercontinuum source at 633 nm.

	Dark room	**Illuminated room**
No warm-up	$3.320 \pm 0.014 (0.428\%)$	$3.277 \pm 0.034 (1.30\%)$
20 min warm-up	$3.427 \pm 0.005 (0.153\%)$	$3.372 \pm 0.011 (0.323\%)$

Table 1, displays the results from the temporal stability tests. It is clear from these that the source needs to be warmed up before it reaches maximum stability. This finding is corroborated in Figure

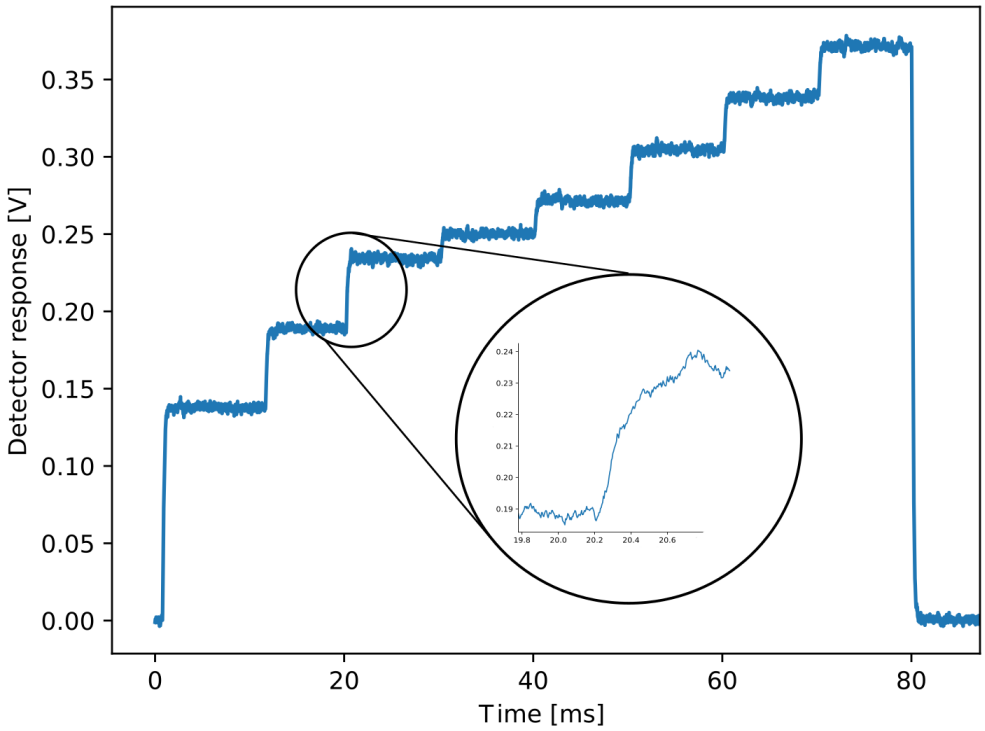

Figure 21: Intensity signal plotted against time during switching between frequencies of the AOTFs for various frequencies

22, showing the graph of one of the measurements made without warm-up. Here, one can observe that the output intensity increases steadily over time. Having the room illuminated during measurements more than doubles the relative variance in intensity. The warm-up of the source decreases the relative instability of the measurements in two ways; increasing the incident intensity and minimizing the insecurity in said intensity. The most surprising finding from these tests is that the measured intensity went down when the room the experiments were conducted in was illuminated. This finding would ordinarily suggest a measurement error, but repeat measurements confirm these findings.

Comparing the results from Table 1 to Figure 20 illustrates that the drift of the source power over time is a greater source of error than that of the random noise on a moment to moment basis. There may be several explanations for this. Firstly, having a powerful laser source directed at the AOTFs could lead to warming, changing the phonon momenta and energies, potentially causing changes in the diffraction efficiency or the wavelength diffracted forward. General changes in temperature in the room may also affect both the supercontinuum source and the detectors used. Implementing temperature corrections in the AOTFs might be beneficial for these reasons, and would be worth investigating for a potential lowering of the noise level. A statistical factor might also be to blame. It is known that the variance of the expectation value of a stochastic signal decrease as a function of $1/\sqrt{N}$, where N is the number of samples taken[61]. Taking this into account there is still an order of magnitude discrepancy between the measured variance of the separate tests, implying that the intensity of the source varies with time. To compensate for this variation, a reference detector is necessitated in the design of the scatterometer.

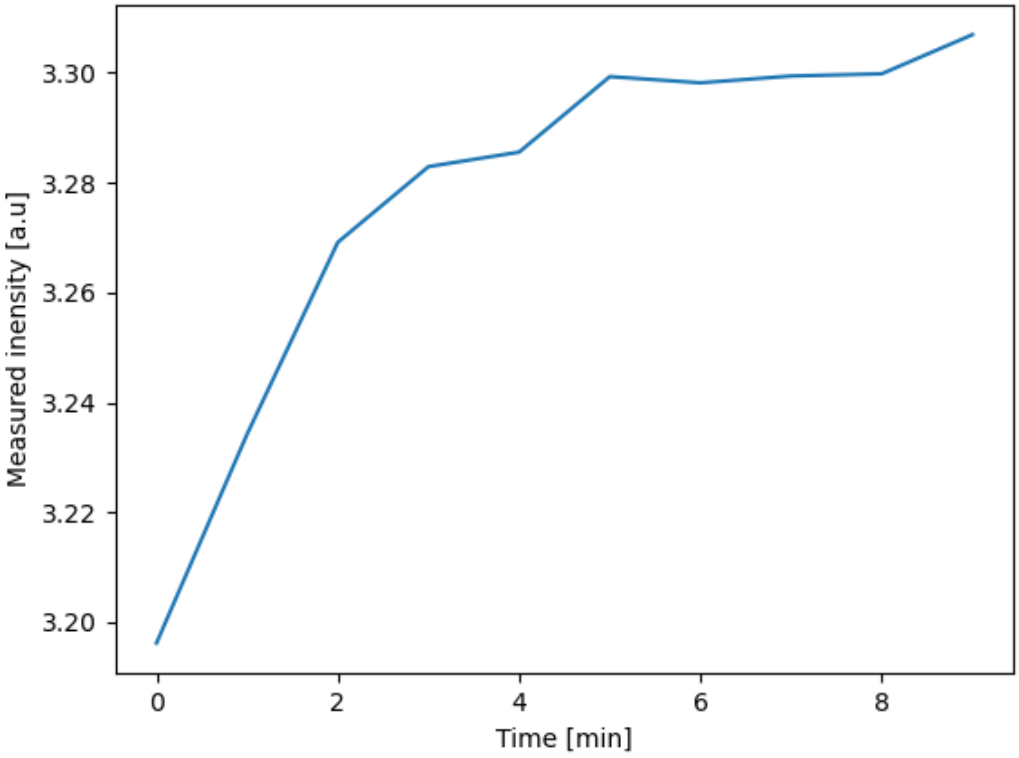

Figure 22: Intensity measurements of source without warm-up time at 633 nm over 9 minutes.

Section 6:

Laser Pulses

The pulse properties of the source were also an object of great interest for the thesis. Not only do they represent a challenge to be overcome with regard to measurement accuracy and non-linear effects, but also a potentially novel way of performing ellipsometry and time-resolved measurements. In this section, the results from three distinct ways of measuring the intensity of a pulsed source are showcased.

6.1 Pulse Measurements

The detector signal produced by the Thorlabs detector is shown in Figure 23. As predicted in section 4.2, the resultant output from the detector is not the resolved pulse of the laser source, but rather the pulse response of the detector itself.

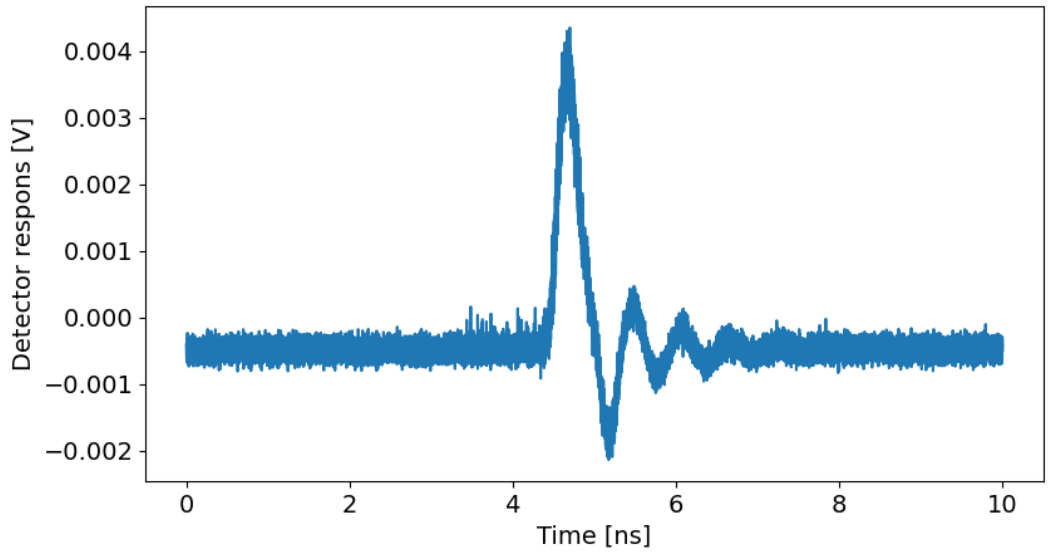

Figure 23: Pulse response of Thorlabs detector.

The pulse shapes of the custom detector can be seen in Figure 24. One can observe that for $\tau = 1, 2, 4$, the pulses have a base at approximately the same value, a little under 0 V. For $\tau = 7$ the base is at 0 V, but a dip after the initial wave that goes below that of the base level of the other settings is present. The total voltage difference between the peak and minimum voltage is lower for $\tau = 7$ compared to other values of τ, making it more sensitive to the noise created in the coupling between the detector and the oscilloscope. Furthermore, the pulse width of the custom detectors does not seem to be substantially affected by which τ is chosen, being a constant width of approximately 11 ns.

As seen in Figure 25, the custom detector is unable to resolve each laser pulse individually when the pulse repetition rate becomes too high. This effect was observed with repetition rates of 20 MHz or above. The repetition rate of the source is then evidently crucial for the quality of the results and should be set to 10 MHz or less to resolve the output pulses from the custom detector.

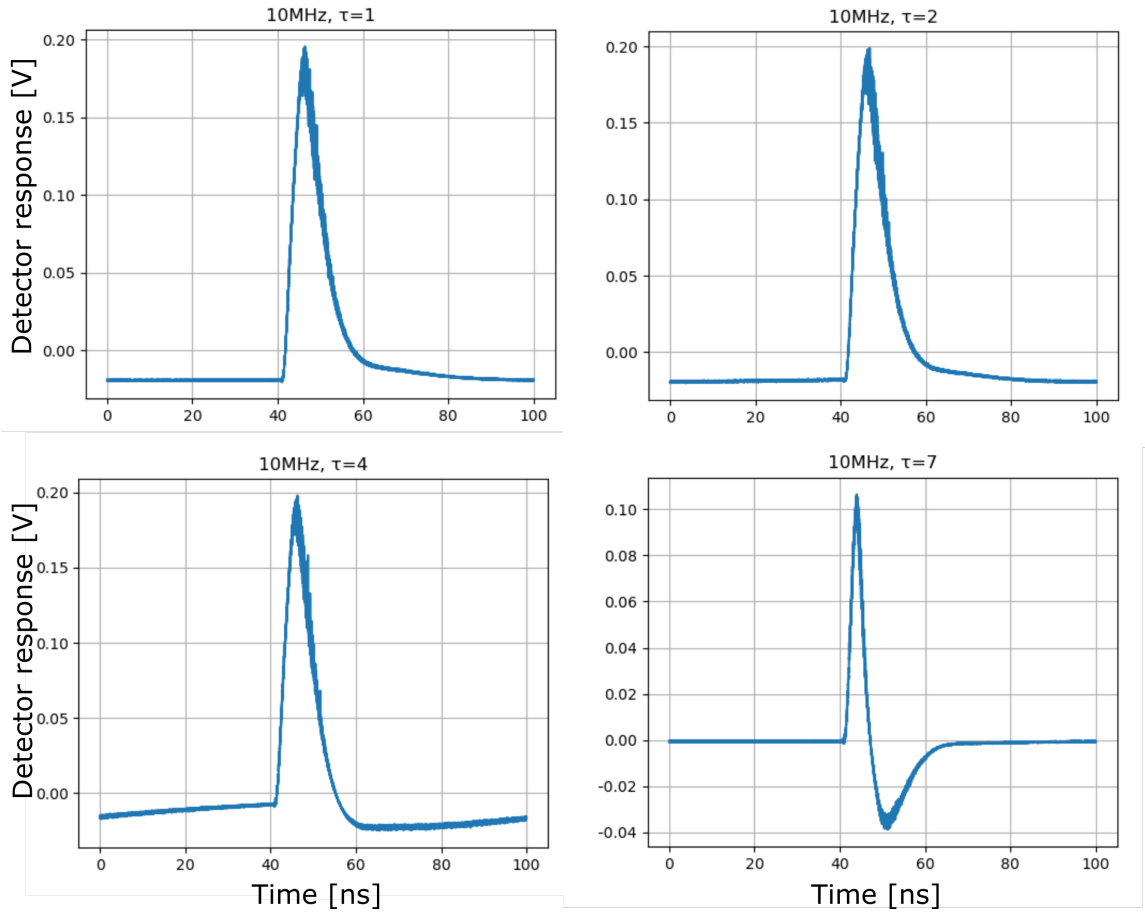

Figure 24: Output of the custom detector for source output at 633 nm with a repetition rate of 10 MHz.

The amplitudes and variation in amplitudes of the pulses measured are displayed in Table 2. The lowest observed relative variation was the custom detector for $\tau = 1$ with a pulse repetition rate of 10 MHz, outperforming $\tau = 7$ by an order of magnitude for all repetition rates. There was no significant difference in relative variation between $\tau = 1$ and the other integration times tested. The Thorlabs detector also performed well in these tests but did not outperform the custom detector with respect to stability for any repetition rate. This low variation in pulse amplitudes are consistent with the findings for other supercontinuum sources [62]

Table 2: Pulse amplitude and stability measured with custom and Thorlabs detector for a selection of repetition rates at 633 nm.

Detector settings	$\tau = 1$	$\tau = 7$	ThorLabs Detector
5 MHz	$0.2053 \pm 0.0010(0.48\%)$	$0.0423 \pm 0.0009(2.12\%)$	N/A
10 MHz	$0.2114 \pm 0.0003(0.14\%)$	$0.03826 \pm 0.0021(5.49\%)$	N/A
20 MHz	$0.2094 \pm 0.0007(0.34\%)$	$0.0409 \pm 0.0021(5.13\%)$	$0.0181 \pm 0.0004118(2.28\%)$
40 MHz	$0.2054 \pm 0.0030(1.46\%)$	$0.0466 \pm 0.0027(5,79\%)$	$0.0184 \pm 0.0006760(3.67\%)$
80 MHz	$0.1518 \pm 0.0194(12.87\%)$	$0.03631 \pm 0.0020(5,51\%)$	$0.0175 \pm 0.0026412(15.09\%)$

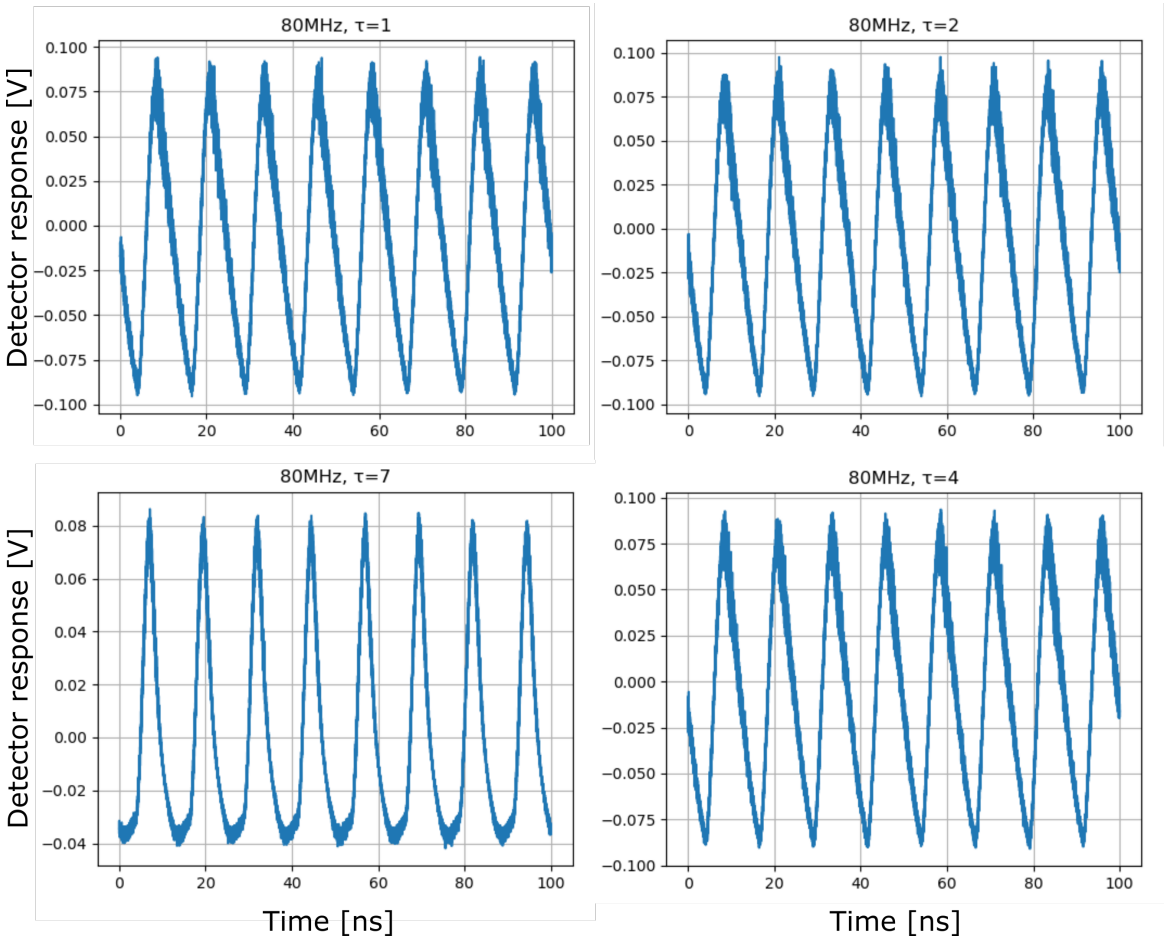

Figure 25: Output of the custom detector for source output at 633 nm with a repetition rate of 80 MHz.

6.2 Pulse Measurements using Integrating Spheres

The attempts to stretch the laser pulses using the integrating spheres did not succeed, as neither of the pulse detectors was sensitive enough to register a signal. In hindsight, the attempt at stretching the laser pulses would not produce the desired result. As stated in section 2.6, the response time of a typical integrating sphere is, similar to the Thorlabs detector, much longer than the width of the laser pulse.This means that the signal recorded would be the response function of the integrating sphere and not the original pulse. This does, of course, not preclude integrating the measured pulse as a way of measuring the total intensity of the pulse, but will give no insight into the shape of the original pulses.

6.3 Linearity Measurements

The detectors were then tested for non-linear effects, and the results are displayed in Figure 26. Both the integrating spheres and the Thorlabs detector performed well with a coefficient of determination $R^2 > 0.99$. The custom detector did not performer as well with $R^2 = 0.6939$.

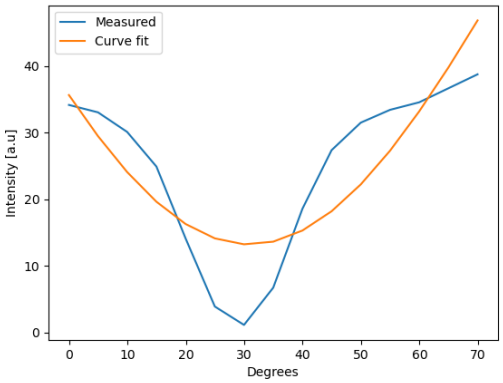

(a) Custom-detector

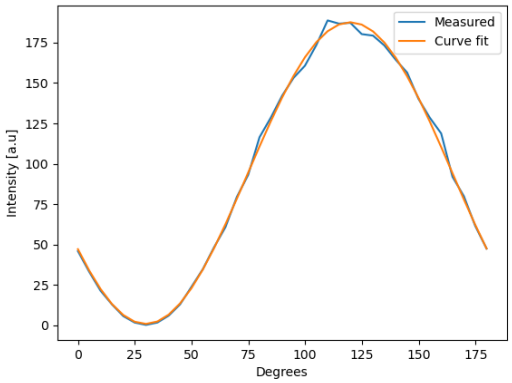

(b) Thorlabs-detector

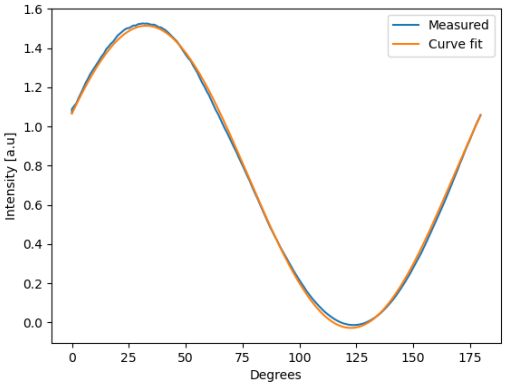

(c) Integrating sphere

Figure 26: Non-linearity measurements of (a) the custom detector, (b) the Thorlabs detector, and (c) the integrating spheres.

There is reason to believe that the results for the custom detector are not accurate. A screen dump of this from the oscilloscope may be seen in Figure 27. indicating that the recorded pulse was distorted. The reason for this was first thought to be reflections in the internal circuitry of the detector. To confirm this, the detector was sent back to the manufacturer, who could not find any issues. This meant that the fault had to lie in the coupling between the oscilloscope and the detector since the oscilloscope was operating normally. This issue was not resolved.

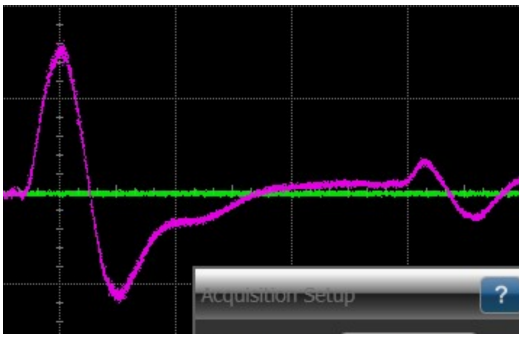

Figure 27: Screen dump from the oscilloscope showcasing the disfigured pulse in purple.

6.4 Transmission Measurements

The results from the transmission tests are displayed in Table 3. These indicate that the integrating spheres and the pulse detectors provide results close to the manufacturer's reported transmittance values of the measured NDFs. The standard deviation of the results obtained differs significantly between the two. Despite the measurements taken with the pulse detectors generally being closer to the reported values of the NDFs, the integrating spheres provided results with significantly lower uncertainty. The NDFs used were worn, and a deviation in the actual transmittance compared to the reported ones from the manufacturer is to be expected. From these results, combined with the previous results of this section, it is clear that the detector best suited for use in the final scatterometer is the integrating sphere. In addition to not being as sensitive to beam wobble, it has proved to be the most consistent and simplest to implement detector among the two alternatives presented in this thesis.

Table 3: Transmission measurements of neutral density filters direct pulse measurements and integrating spheres

NDF **T%**	**Pulse detectors** **T%**	**Integrating spheres** **T%**
5.7	$5.575 \pm 0.47(8.43\%)$	$5.72 \pm 0.075(1.31\%)$
20.9	$20.725 \pm 2.11(10.18\%)$	$21.4 \pm 0.071(0.33\%)$
62.7	$62.3 \pm 1.50(2.41\%)$	$63.63 \pm 0.083(0.13\%)$

What is also interesting is that the standard deviation of the transmittance values found with the integrating spheres appears to be independent of the transmittance of the NDF measured, compared to the measurements using the pulse detectors, whose standard deviation varies significantly with which NDF is measured. The significance of this is not known but may suggest an error in the way the transmittance was measured with the pulse detectors.

Several measures may be taken to improve the results of the pulse measurements. The simplest would be to replace the Thorlabs detector with another custom detector to reduce the measurement inaccuracies. Secondly, when measuring the transmittance of the NDF, the same pulse was intended to be measured in the reference detector and the main detector. If this is not the case, errors in the measured transmittance should be expected. Therefore, verifying that the correct pulses are compared might lead to a significant reduction in measurement uncertainty. Lastly, addressing the problem contributing to the warped shape of the output pulse from the custom detector is likely to improve the result. The results do therefore not discredit the usage of individual pulse to do measurements in general. Improvements do need to be made before it becomes a viable alternative, however.

Section 7:

Realisation of Complete Mueller Matrix Scatterometer

In this section, the results from the assembly and calibration of the ellipsometer for use in the final scatterometer are showcased, as well as results from tests of the said scatterometer.

7.1 Intensity Fit Calibration

The model for the intensity fit method that provided the best results modeled the Muller matrix for the polarizer as

$$\mathbf{M}_{pol} = \begin{bmatrix} 1 & a & 0 & 0 \\ a & 1 & 0 & 0 \\ 0 & 0 & 0 & 0 \\ 0 & 0 & 0 & 0 \end{bmatrix}, \tag{7.1}$$

where a is a real constant. The prism retarders were modelled using Eq. (2.56).. All four components were additionally given an azimuthal angle dependency.To improve the model further, an attempt at introducing optical rotation into the model was made. This attempt was, however, unsuccessful. Despite this, however, it is clear from Figure 28 that the model found from this method seems to align quite well with the recorded intensities, though with some minor discrepancies. It was found that the fit had a coefficient of determination of $R^2 = 0.9962$.

Using the results from the calibration to reproduce the Muller matrix of air for 633 nm resulted in

$$\mathbf{M} = \begin{bmatrix} 1.000 & 0.0033 & -0.0087 & -0.0011 \\ 0.0078 & 1.0075 & 0.0305 & 0.03353 \\ 0.0011 & -0.0421 & 1.0235 & -0.0253 \\ -0.0090 & -0.0192 & -0.0010 & 0.9544 \end{bmatrix}. \tag{7.2}$$

As can be seen in Eq. (7.2), the results from this calibration were not encouraging. Several elements, like m_{33}, showed deviation from the expected values of up to 5%. This is not an acceptable amount of difference for a Mueller matrix but does not necessarily imply that the approach should be abandoned. If a more accurate model is found, a more precise result ought to be obtained. Furthermore, it has also been shown that it is possible to filter Mueller matrices to reduce their error[63, 64]. Implementing such filtering may be sufficient to reduce the deviation from the expected values to an acceptable level.

Despite the calibration for 633 nm proving limitedly successful, attempts to extend the calibration to the rest of the spectrum proved to be difficult. The $\sqrt{3}$ for physical condition numbers were found to be broken for several of the wavelengths, and the optimized values used in the model were found to be nonphysical. For instance, the polarizer used in the PSG was found to be

$$\mathbf{M}_{pol} = \begin{bmatrix} 1 & -1.3 & 0 & 0 \\ -1.3 & 1 & 0 & 0 \\ 0 & 0 & 0 & 0 \\ 0 & 0 & 0 & 0 \end{bmatrix}. \tag{7.3}$$

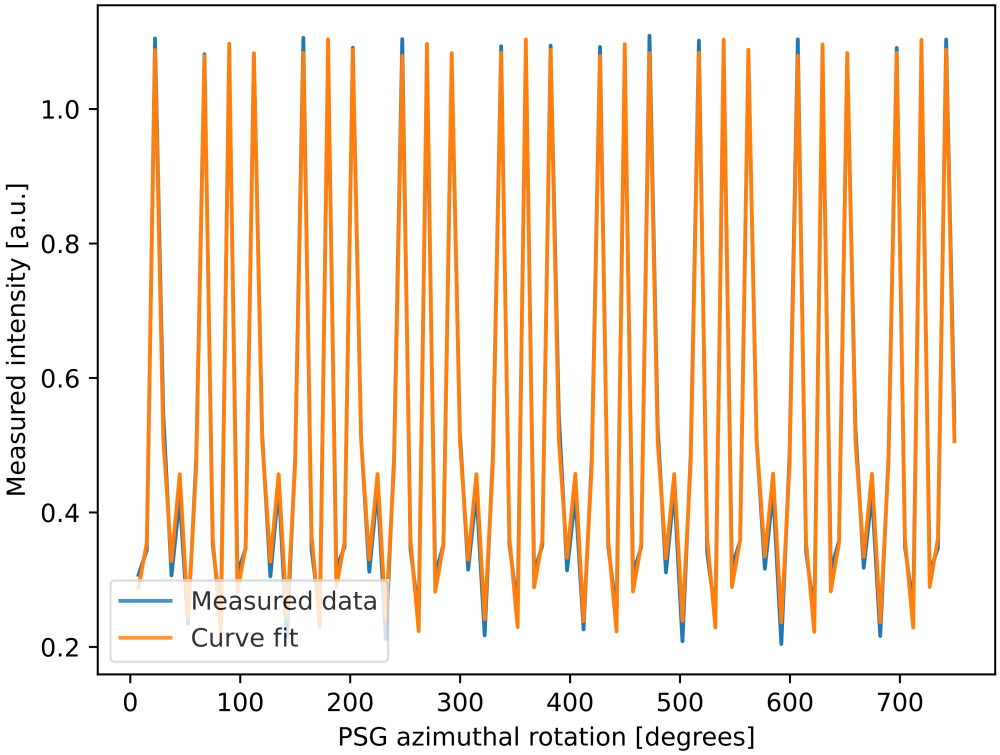

Figure 28: Measured and calculated intensities for the ellipsometer for a PSA:PSG rotation ration of 37.5 to 7.5 for 633 nm.

Several attempts were made to improve the results of the spectroscopic calibration, including adjusting the optical components of the system. No solution was found that improved the results, however. It was concluded that the problem lay in a minute mathematical error in the program performing the calibration. This fault was not discovered and further attempts at using this method were subsequently abandoned in favour of proceeding to the next calibration method.

7.2 Eigenvalue calibration

The next step was to test the efficacy of the eigenvalue calibration method. The preliminary test results using the filter wheel with appropriate samples did not immediately turn out well, with deviations in the order of 1%. This problem was corrected by eliminating the use of a reference detector and correcting errors in the data-gathering program. After this, the results in the 800 to 1000 nm range showed promising results with deviations from the expected values $< 0.01\%$.

Knowing that the instrumentation and calculation parts of the setup were now functioning properly, the spectral width of the calibration was widened. As can be seen in Figure 29,, the resultant condition numbers from the eigenvalue calibration method are promising, being consistently close to the ideal $\sqrt{3}$ mark for both $\mathbf{A}$ and $\mathbf{W}$. This excludes 665 nm, where a clear spike in the condition numbers may be observed for the system matrices for both the PSA and the PSG. This was not unexpected due to the particularly low intensity for this wavelength, as discussed in section 5.1. It is also encouraging that the otherwise consistently good results across the spectrum exceed the performance of other ellipsometers made with the same supercontinuum laser by previous master's students[65].

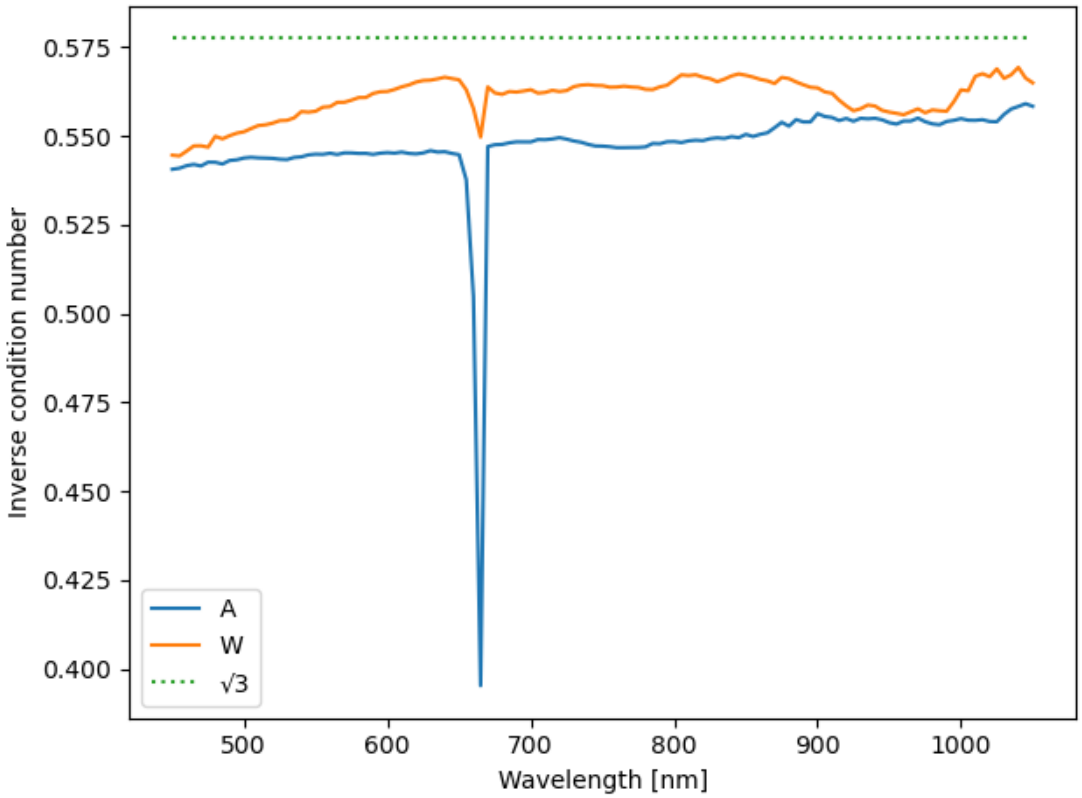

Figure 29: Inverse condition numbers of **A** and **W** obtained using the eigenvalue calibration method.

The Mueller matrices in Figure 30 are constructed from the calibration measurements. The elements of the Mueller matrix for air deviate from the expected values by less than 1% across the recorded spectral range of the ellipsometer. This is a good result even compared to traditional, and modern, professionally made, ellipsometers using continuous-wave illumination[66, 67]. Beyond this, it is also observable that the Mueller matrix elements exceed unity, which is most likely due to calculation errors in the system matrices. These errors may be mitigated by multiplying any measured MM with the inverse of the MM for air[68].

The Mueller matrices of the polarizer display deviation from expected values approaching and exceeding 1%, or several matrix elements, even outside of 665 nm. They are, however, in the correct form for a linear polarizer with elements m_{00}, m_{01}, m_{10} and m_{11} approaching positive or negative unity, while other elements are close to zero (see Eq. (2.33)). The measured deviation increases for longer wavelengths, as is expected from the low intensities. Another feature of the results is what appears to be wavelength-dependent oscillation in the NIR regime. This may be random noise inducing an increased deviation due to the relatively low intensity of the incident. It is also possible that Fabry Pero interference from the retarder prisms plays a part in this, as the source is both highly temporally and spatially coherent. Another contributing factor might be that the calibration polarizer used not function properly, as it was selected without prior testing.

The final sample produces a Mueller matrix consistent with an azimuthally rotated retarder with a slight wavelength-dependent retardance. Like the results from the air and the linear polarizer, deviations from the expected value increase with wavelength. The drop in intensity for 665 nm is pronounced for this sample, leading to dominant value spikes for this wavelength.

The observed sensitivity of the system to low intensities presents a potential challenge for the implementation of the ellipsometer in the planned scatterometer when measuring weakly scattered beams.

This may be mitigated slightly by removing the NDF that sends a portion of the laser beam to the reference. The best solution would, however, be to increase the intensity output in the NIR spectrum of the source to be at the level of the visible light portion of the spectrum.

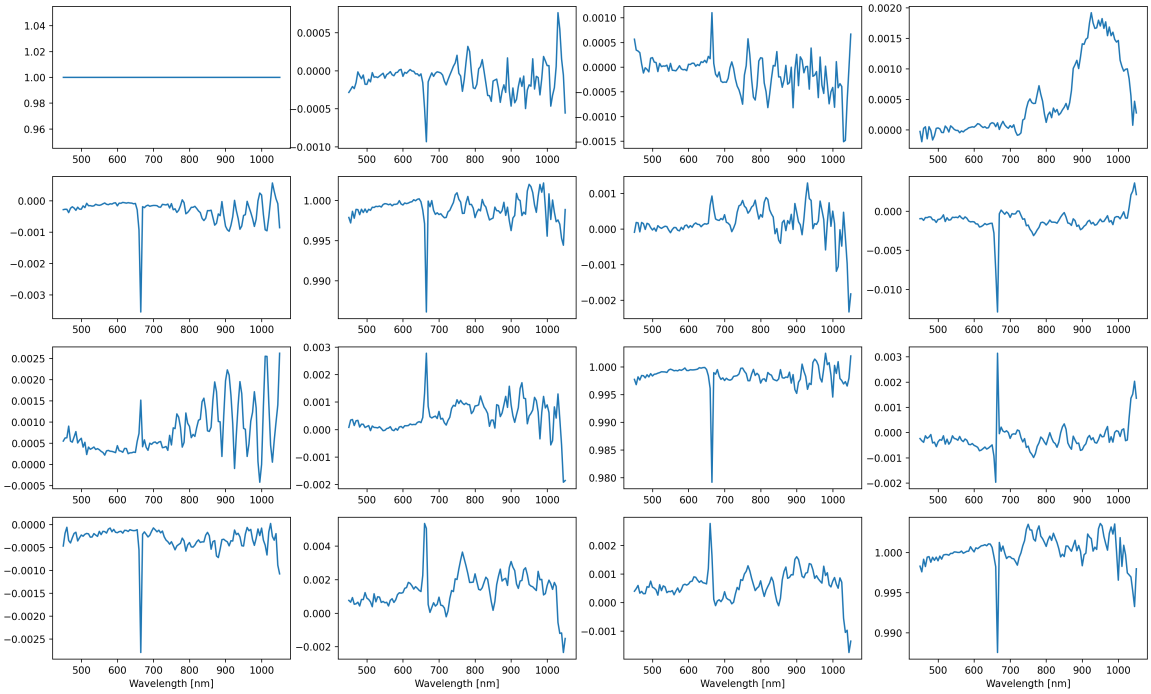

(a) Air

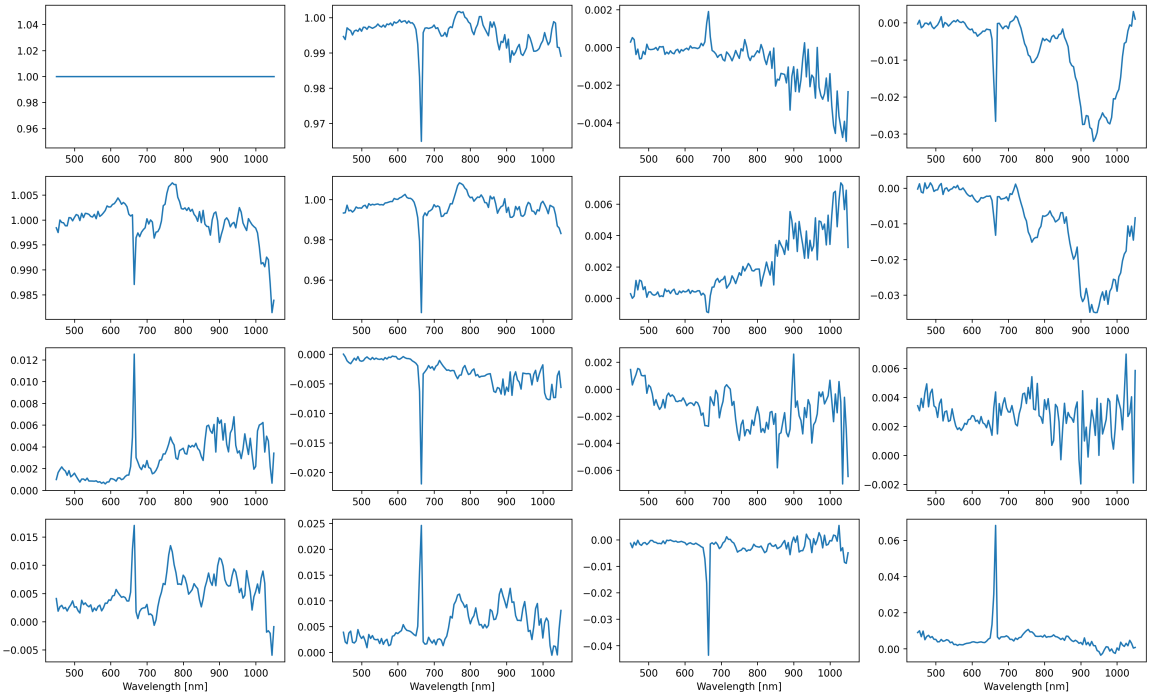

(b) Polarizer, vertical transmission axis

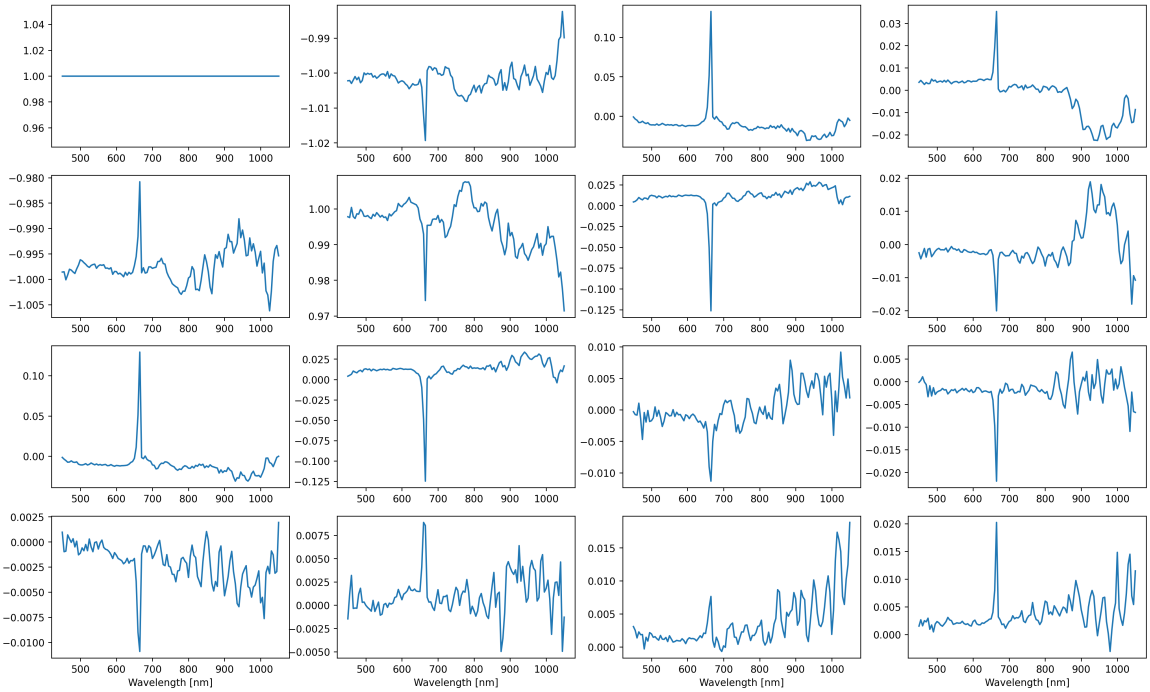

(c) Polarizer, horizontal transmission axis

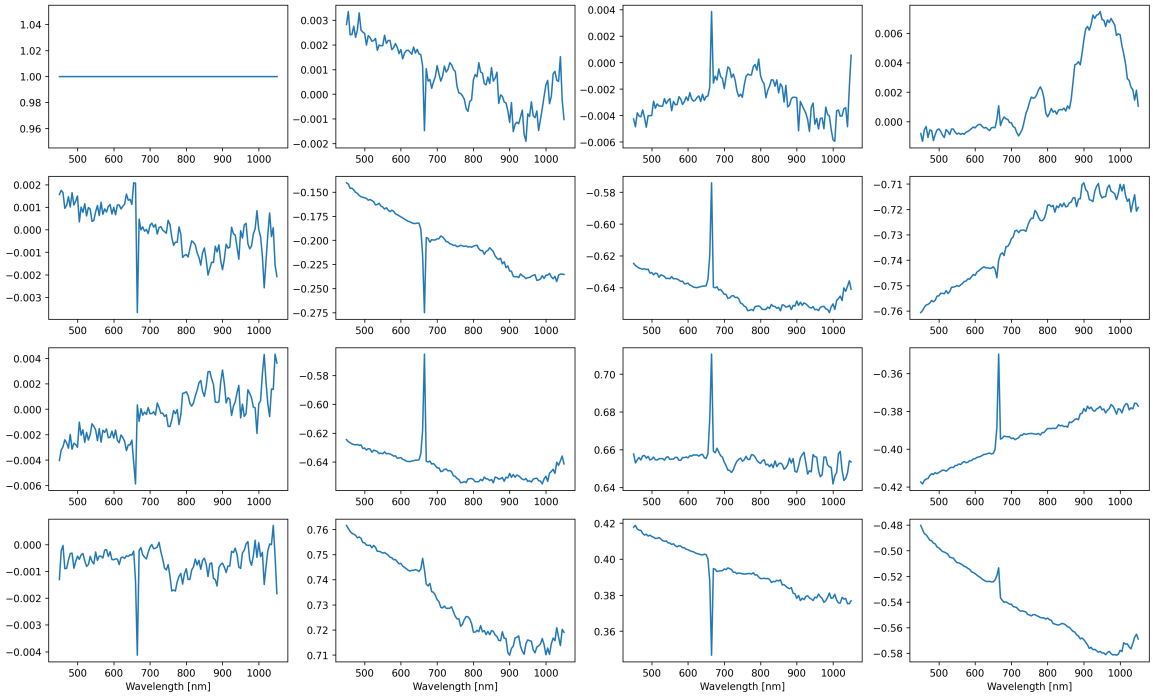

(d) Rotated prism retarder

Figure 30: Normalized Mueller matrices of the calibration samples

A measurement of the Mueller matrix of air independent of the calibration measurements is displayed in Figure 31. It is possible to observe a greater deviation in the matrix elements compared to the results from the calibration. The reason for this is probably the drift of the source intensity over time, as found during the preliminary tests. A potential solution to this problem is to reintroduce a reference detector to the setup, as to correct for the drift in the intensity from the source. This would necessitate finding a way to implement the reference that does not introduce the level of noise seen previously. One simple way of doing this would be to use a superior photodiode amplifier for the reference, though it is not clear if this would reduce the noise signal sufficiently. Another alternative is naturally to overcome the issues with using pulse detectors and using these instead of the integrating spheres, as this would provide real-time corrections for variations in the source as the measurements are taken.

As pointed out repeatedly, a reoccurring problem with all the Mueller matrices recorded is the reduction of measurement accuracy at 665 nm. This error is caused by the low-intensity output of the source at this wavelength, due to the dichroic beam splitter used. This issue is, however, not fixable by simple modifications to the wavelength selection scheme, as any other dichroic beam splitter would induce the same problem at another wavelength. A more realistic solution would be to utilize the fact that the elements of the Mueller matrix should be smooth when plotted as a function of wavelength. It should therefore be possible to use interpolation to extract an estimate for this value with greater certainty than direct measurements may provide with the current setup.

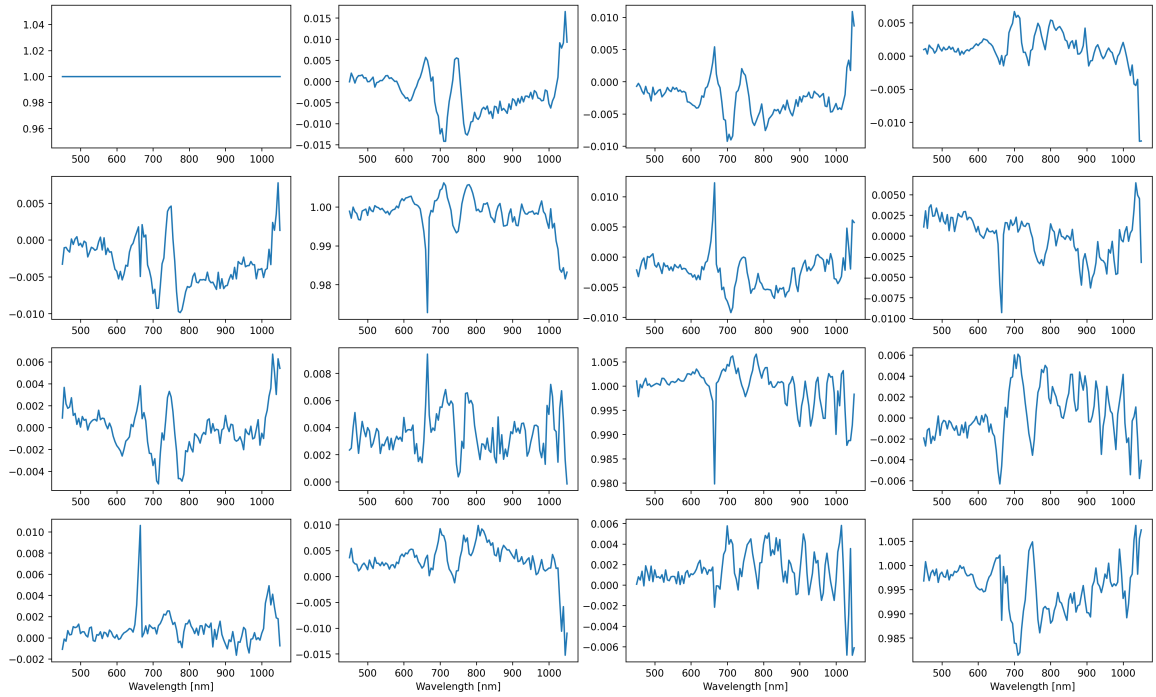

Figure 31: Normalized Mueller matrices of air measured separately from the calibration.

7.3 Building and Testing of the Scatterometer

When designing the scatterometer, doubts regarding the motors selected for the design were sufficient and whether the design was stable enough were raised. Assembling the scatterometer did suggest that neither of these concerns was warranted, as the design was sufficiently stable and the motors seemed to be able to handle the necessary load and torque.

The test of the beam splitting polarizer indicated that the scatterometer was working as intended, and the resulting Mueller matrices may be seen in Figure 32. The polarizer used does not resemble any conventional polarizer, however, if one applies the measured matrices on a depolarized beam and utilizes Eq. (2.26) to evaluate the resultant Stokes vector, one finds that the beam splitter is a polarizer with a polarizance of $> 99\%$ for both angles at all wavelengths. At some wavelengths, the polarizance exceed 1, which should not physically not be possible. This was not surprising, however, as the calibration was made in haste, as to be able to meet the deadline of the thesis, in addition to the fact that the ellipsometer has been shown to be prone to measurement errors in the NIR portion of the spectrum in prior experiments.

The measurements of the metasurface did however not yield any results, as the detectors did not detect any scattered light. A simple explanation for this is that the metasurface was defective due to damage or other reasons. Another compounding factor for this is that the beam was much wider than the metasurface, and an insufficient amount of the incident flux was scattered. This can potentially be remedied by shrinking the beam diameter using lenses. Another explanation may be that the sample was not placed in the rotation centre of the scatterometer, resulting in the scattered beams not being incident on the integrating sphere. Finally, it is possible that the integrating spheres were not sensitive enough to acquire a signal.

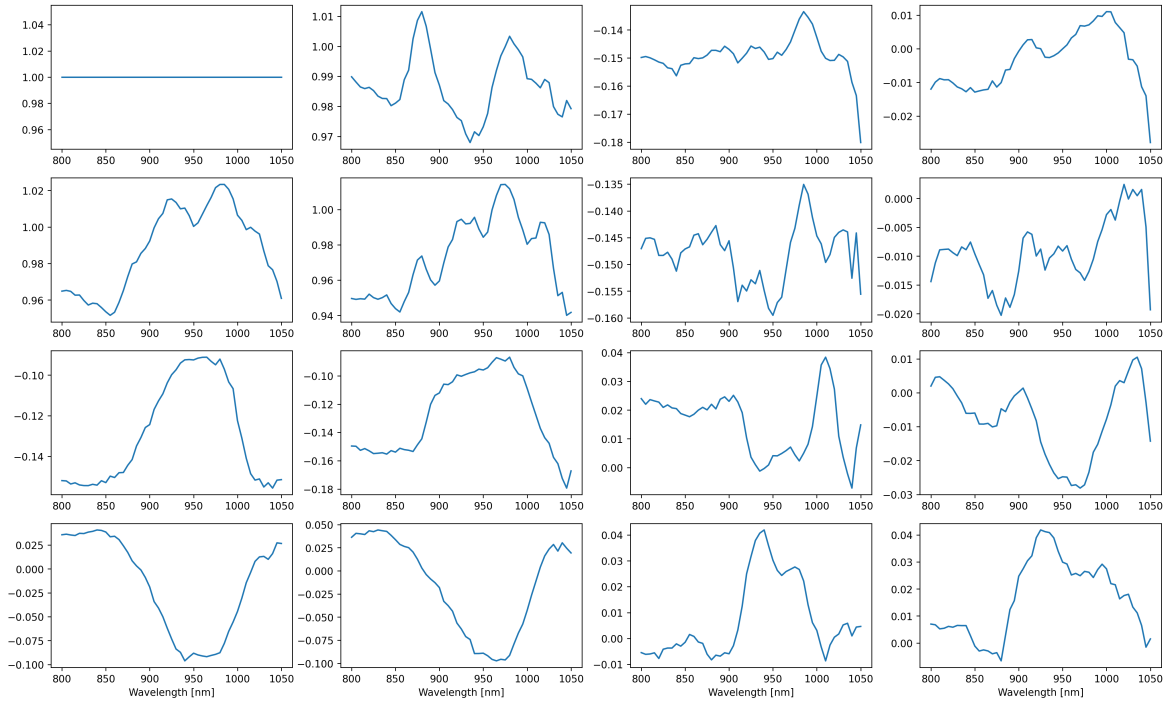

(a)

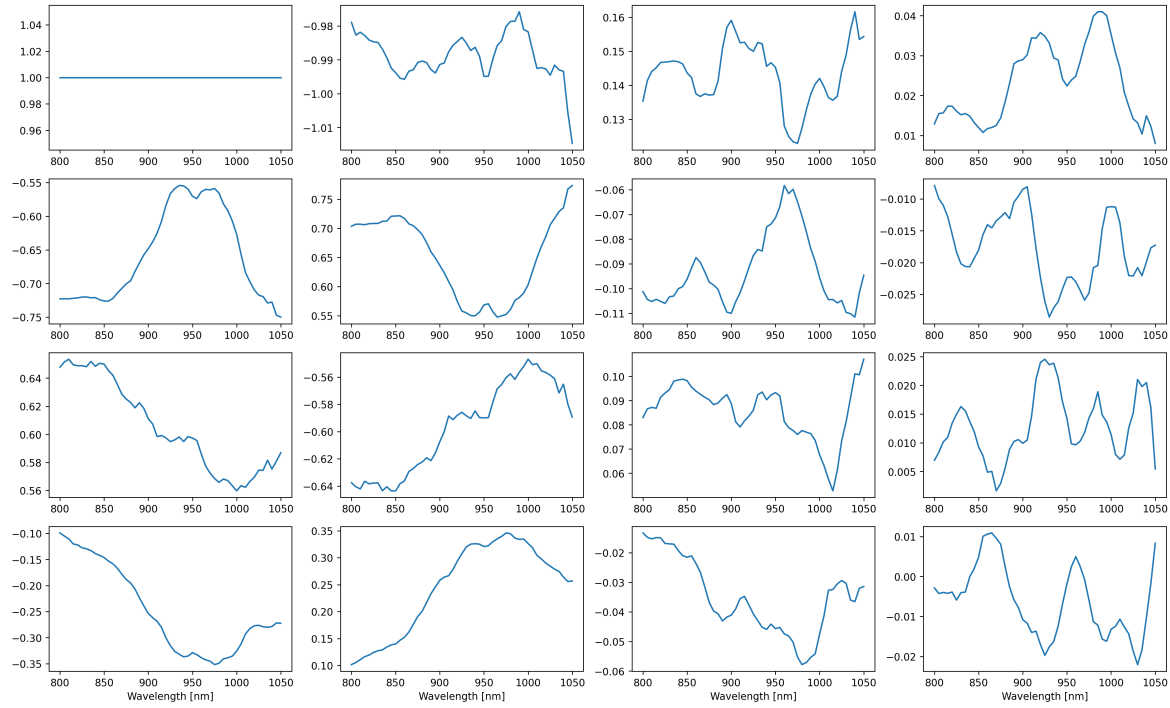

(b)

Figure 32: The measured normalized Mueller matrices of a beam splitting polarizer with horizontal transmission axis measured with the constructed scatterometer. a) displays the Mueller matrix of the beam propagating through the polarizer without refraction, while b) is the Mueller matrix of the beam refracted at a 5° angle.

7.4 Comments on the Code

The final code seems to be working well for the purposes of ellipsometry. Both the calibration and the Mueller matrix measurement programs ran quickly and produce satisfactory results. To perform a spectroscopic Mueller matrix measurement took a little over a minute. Most of the run time was due to the rotation of the prisms, taking about 3 to 5 s, depending on the distance. The remaining runtime was used to scan through the spectrum for each polarization state. Considering the calibration samples had to be manually put into the correct position, the calibration time was acceptable, only lasting approximately 8 minutes.

There were, however, some problems with the code. Most notably, it tended to crash after a certain amount of intensity measurements. It was determined that the problem was due to the RAM used for the programs saturating, as evidenced by the fact that other computer programs could not be used simultaneously, lest the said program crash. This issue was alleviated slightly by actively deleting arrays when no longer needed in the program. This was not sufficient to fix the problem entirely, however. A temporary solution was to close and open the software every few measurements. This is of course not an ideal solution if this software is to be adopted into the final scatterometer, as many Mueller matrices need to be measured for each sample. Increasing the RAM of the computer and implementing clearing of buffers may therefore provide a more permanent solution to the problems faced.

Further improvements to the code may be made by increasing the functionality and user friendliness. Functionality may be improved by implementing analysis of the measured Mueller matrices, as detailed in section 2.1.6. As for unfriendliness, further automating the the calibration process by implementing a filter wheel for the calibration samples and automating the process of switching these is recommended. This would also increase the repeatability of the calibrations.

Part IV:

Conclusions

A spectroscopic Mueller matrix ellipsometer in the wavelength range 450 to 1100 nm for use in a scatterometer, was designed, built, and calibrated. The system used rotating prism retarders to generate the desired polarization states of the PSG and the PSA. To illuminate the samples, a supercontinuum source with AOTFs for the selection of wavelengths was utilized. It was found that the source output intensity was stable from moment to moment, but fluctuated over time. Furthermore, it was also found that the intensity output was not equal between the AOTFs, where the intensities recorded for the NIR part of the spectrum were significantly lower than that of the visible part.

The challenges of using a pulsed laser source for use in ellipsometry have been assessed through the exploration of different measurement methods, including direct measurements of the pulses and through the use of integrating spheres. It was determined that integrating spheres was the detectors to be used in the ellipsometer constructed in the thesis. The usage of pulse measurements was however found to have some promise as a measurement technique, given the appropriate setup. Of particular interest is the prospect of using these to do time-resolved measurements for rapid processes.

Two calibration methods were attempted and assessed. It was determined that the eigenvalue calibration method was superior among the two calibration methods in terms of accuracy. The system matrices $\mathbf{A}$ and $\mathbf{W}$, found using the eigenvalue calibration method, had low condition numbers, approaching the ideal $\sqrt{3}$ limits for most of the desired wavelength range. The Mueller matrices measured support these results with deviations below 1%. rom the expected values. Repeat measurements of samples display an increase in inaccuracies. The largest deviations were found in the vicinity of 633 nm and in the NIR region.

Software for controlling the measurements was also made. This ensured swift measurements despite mechanically moving parts used in the ellipsometer. Problems with crashing did occur despite the underlying cause being identified.

A basic design for a scatterometer has also been improved upon and constructed in the thesis. This was used to measure a simple beam splitting polarizer and a beam splitting meta-surface. The polarizer provided results that were slightly nonphysical for some wavelengths, while the beam splitting meta-surface did not produce a strong enough signal to be measured by the scatterometer.

Further developments for the project, should focus on improving the software controlling the ellipsometry functions of the scatterometer as well as improving intensity output from the source in the NIR part of the spectrum. Furthermore, automation of the calibration process should also be prioritized to save time. Alternatively, a more sensitive detector could be used. Software for controlling the scatterometer will also need to be developed. Finally, implementing filtering for improvements to the measured Mueller matrices should be considered and a routine to compensate for errors at 665 nm should be developed.

Bibliography

[1] A. Mark SMITH. 'Ptolemy's Theory of Visual Perception: An English Translation of the "Optics" with Introduction and Commentary'. eng. In: *Transactions of the American Philosophical Society* 86.2 (1996). ISSN: 0065-9746.

[2] Shastra Pratibha. 'Shastra Pratibha 2015 Seniors Booklet'. In: (2015).

[3] Rasmus Bartholin. *Experiments on birefringent Icelandic crystal*. mul;eng;lat. Vol. 40. Acta historica scientiarum naturalium et medicinalium. Copenhagen: Danish National Library of Science and Medicine, 1991. ISBN: 8777090101.

[4] Gábor Horváth et al. 'Imaging polarimetry of the fogbow: polarization characteristics of white rainbows measured in the high Arctic'. In: *Appl. Opt.* 50.28 (Oct. 2011), F64–F71. DOI: 10.1364/AO.50.000F64.

[5] Hans Arwin. *Thin Film Optics and Polarized Light*. 6th ed. 2016.

[6] John William Strutt. 'On the Light from the Sky, its Polarization and Colour'. In: *Scientific Papers*. Vol. 1. Cambridge Library Collection - Mathematics. Cambridge University Press, 2009, pp. 87–103. DOI: 10.1017/CBO9780511703966.009.

[7] M. S Longair. *Theoretical concepts in physics : an alternative view of theoretical reasoning in physics*. eng. 2nd ed. Cambridge: Cambridge University Press, 2003. ISBN: 0521821266.

[8] James Clerk Maxwell. *A treatise on electricity and magnetism*. eng. New York, 1954.

[9] P Drude. 'Ueber Oberflächenschichten. I. Theil'. ger. In: *Annalen der Physik* 272.2 (1889), pp. 532–560. ISSN: 0003-3804.

[10] Harland G. Tompkins and James N. Hilfiker. *Spectroscopic Ellipsometry : Practical Application to Thin Film Characterization*. Materials Characterization and Analysis Collection. Momentum Press, 2016. ISBN: 9781606507278.

[11] Ari Sihvola. 'Metamaterials in electromagnetics'. eng. In: *Metamaterials* 1.1 (2007), pp. 2–11. ISSN: 1873-1988.

[12] Nanfang Yu and Federico Capasso. 'Flat optics with designer metasurfaces'. eng. In: *Nature materials* 13.2 (2014), pp. 139–150. ISSN: 1476-1122.

[13] Federico Capasso. 'The future and promise of flat optics: a personal perspective'. In: *Nanophotonics* 7.6 (2018), pp. 953–957. DOI: doi:10.1515/nanoph-2018-0004. URL: https://doi.org/10.1515/nanoph-2018-0004.

[14] Donald R. Huffman Craig F. Bohren. 'Absorption and Scattering by an Arbitrary Particle'. In: *Absorption and Scattering of Light by Small Particles*. John Wiley & Sons, Ltd, 1998. Chap. 3, pp. 57–81. ISBN: 9783527618156. DOI: https://doi.org/10.1002/9783527618156.ch3.

[15] David J. Griffiths. *Introduction to Electrodynamics*. Cambridge University Press, 2017. ISBN: 9781108420419.

[16] Eugine Hecht. *Optics*. Pearson Education, 2017. ISBN: 9781292096933.

[17] Gilbert Strang. *Introduction to Linear Algebra*. Wellesley Cambridge Press, 2016. ISBN: 9780980232776.

[18] Born Max and Wolf Emil. *Principles of Optics : Electromagnetic Theory of Propagation, Interference and Diffraction of Light*. Pergamon, 1980. ISBN: 9780080264820. URL: https://search.ebscohost.com/login.aspx?direct=true%5C&db=nlebk%5C&AN=1283881%5C&site=ehost-live.

[19] R. Clark Jones. 'A New Calculus for the Treatment of Optical SystemsI. Description and Discussion of the Calculus'. In: *J. Opt. Soc. Am.* 31.7 (July 1941), pp. 488–493. DOI: 10.1364/JOSA.31.000488.

[20] George Gabriel Stokes. 'On the Composition and Resolution of Streams of Polarized Light from different Sources'. In: *Mathematical and Physical Papers*. Vol. 3. Cambridge Library Collection - Mathematics. Cambridge University Press, 2009, pp. 233–258. DOI: 10.1017/CBO9780511702266.010.

[21] Zhaozhong Chen et al. 'Complete shaping of optical vector beams'. eng. In: *Optics express* 23.14 (2015), pp. 17701–17710. ISSN: 1094-4087.

[22] Kenneth Järrendahl and Bart Kahr. 'Hans Mueller (1900-1965)'. In: *Wollam annual newsletter* 12 (Jan. 2011), p. 8.

[23] Hans Mueller. 'Memorandum on the polarization optics of the photoelastic shutter'. In: *OSRD project OEMsr-576* Report No. 2 (Nov. 1943).

[24] Shih-Yau Lu and Russell A. Chipman. 'Interpretation of Mueller matrices based on polar decomposition'. In: *J. Opt. Soc. Am. A* 13.5 (May 1996), pp. 1106–1113. DOI: 10.1364/JOSAA.13.001106.

[25] Augustin-Jean Fresnel and Gavin Richard (tr./ed.) Putland. 'On the calculation of the tints that polarization develops in crystalline plates, & postscript'. Version 3. In: (Feb. 2021). DOI: 10.5281/zenodo.4561712.

[26] Sune Dupont et al. 'IR microscopy utilizing intense supercontinuum light source'. In: *Opt. Express* 20.5 (Feb. 2012), pp. 4887–4892. DOI: 10.1364/OE.20.004887.

[27] Amanda J Wright et al. 'Transfer of orbital angular momentum from a super-continuum, white-light beam'. In: *Opt. Express* 16.13 (June 2008), pp. 9495–9500. DOI: 10.1364/OE.16.009495.

[28] M. Guillon, K. Dholakia and D. McGloin. 'Optical trapping and spectral analysis of aerosols with a supercontiuum laser source'. In: *Opt. Express* 16.11 (May 2008), pp. 7655–7664. DOI: 10.1364/OE.16.007655.

[29] Valerii Viktorovich Tuchin. 'Optical Properties of Tissues with Strong (Multiple) Scattering'. In: *Tissue Optics Light Scattering Methods and Instruments for Medical Diagnosis*. SPIE, 2021, pp. 1–103.

[30] A. Dubietis and A. Couairon. *Ultrafast Supercontinuum Generation in Transparent Solid-State Media*. Vol. 7. 18. IOP Publishing, 2019, pp. 2490–2500. DOI: 10.1088/0022-3727/7/18/308.

[31] Lei Zhang. *Ultra-Broadly Tunable Light Sources Based on the Nonlinear Effects in Photonic Crystal Fibers*. eng. 1st ed. 2016. Springer Theses, Recognizing Outstanding Ph.D. Research. Berlin, Heidelberg: Springer Berlin Heidelberg : Imprint: Springer, 2016. ISBN: 3-662-48360-2.

[32] Irina T. Sorokina et al. 'Mid-IR Ultrashort Pulsed Fiber-Based Lasers'. eng. In: *IEEE journal of selected topics in quantum electronics* 20.5 (2014), pp. 99–110. ISSN: 1077-260X.

[33] J. Dudley J. & Taylor. *Supercontinuum Generation in Optical Fibers*. Cambridge University Press, 2010. DOI: 10.1017/CBO9780511750465.

[34] F. author. Poli. *Photonic Crystal Fibers Properties and Applications /*. 1st ed. 2007. Dordrecht : Springer Netherlands : 2007, p. 239. ISBN: 1-4020-6325-3.

[35] Ling Bei et al. 'Acousto-optic tunable filters: fundamentals and applications as applied to chemical analysis techniques'. In: *Progress in Quantum Electronics* 28.2 (2004), pp. 67–87. ISSN: 0079-6727. DOI: https://doi.org/10.1016/S0079-6727(03)00083-1.

[36] I. C. Chang. 'Noncollinear acousto-optic filter with large angular aperture'. In: *Applied Physics Letters* 25.7 (1974), pp. 370–372. DOI: 10.1063/1.1655512. URL: https://doi.org/10.1063/1.1655512.

[37] R.W. Dixon. 'Acoustic Diffraction of Light in Anisotropic Media'. In: *IEEE Journal of Quantum Electronics* 3.6 (1967), pp. 85–93. URL: https://www.proquest.com/scholarly-journals/acoustic-diffraction-light-anisotropic-media/docview/28249104/se-2?accountid=12870.

[38] V. A. Sømnes. 'Evaluation of Acousto-Optic Tunable Filter for Wavelength Dependent Measurements of Waveguides'. MA thesis. Norges Teknisknaturvitenskaplige Universitet-NTNU, 2016, p. 85.

[39] Emma P. Mukhokosi et al. 'Device Architecture for Visible and Near-Infrared Photodetectors Based on Two-Dimensional SnSe2 and MoS2: A Review'. In: *Micromachines* 11.8 (2020). ISSN: 2072-666X. DOI: 10.3390/mi11080750. URL: https://www.mdpi.com/2072-666X/11/8/750.

[40] Michele Buscema et al. 'Photocurrent generation with two-dimensional van der Waals semiconductors'. eng. In: *Chemical Society reviews* 44.11 (2015), pp. 3691–3718. ISSN: 0306-0012.

[41] Meredith N. Draa, Alexander S. Hastings and Keith J. Williams. 'Comparison of photodiode nonlinearity measurement systems.' In: *Optics express* 19 13 (2011), pp. 12635–45.

[42] Chun-Lun Wang et al. 'High-performance 1–10THz integrating sphere'. In: *Appl. Opt.* 60.13 (May 2021), pp. 3784–3790. DOI: 10.1364/AO.420311.

[43] Labsphere Inc. *Technical guide: integrating sphere theory and applications*. 2017. URL: https://www.pro-lite.co.uk/File/LAB%5C%20TechGuide%5C%20-%5C%20Integrating%5C%20Sphere%5C%20Radiometry%5C%20%5C&%5C%20Photometry.pdf.

[44] E. Kreyszig. *Advanced Engeneering Mathematics, tenth edition*. John Wiley & Sons Ltd, 2011.

[45] Thomas N. E. Ben-Israel Adi; Greville. 'Introduction'. In: *Generalized Inverses: Theory and Applications*. New York, NY: Springer New York, 2003, pp. 1–5. ISBN: 978-0-387-21634-8. DOI: 10.1007/0-387-21634-0_1.

[46] J C Vap, S E Nauyoks and M A Marciniak. 'Optimization of a dual-rotating-retarder polarimeter as applied to a tunable infrared Mueller-matrix scatterometer'. eng. In: *Measurement science & technology* 24.5 (2013), pp. 55901–1-8. ISSN: 0957-0233.

[47] Lars M.S. Aas et al. 'Dynamic response of a fast near infra-red Mueller matrix ellipsometer'. In: *Journal of Modern Optics* 57.17 (2010), pp. 1603–1610. DOI: 10.1080/09500340.2010.515750. URL: https://doi.org/10.1080/09500340.2010.515750.

[48] J. Scott Tyo. 'Noise equalization in Stokes parameter images obtained by use of variable-retardance polarimeters'. eng. In: *Optics letters* 25.16 (2000), pp. 1198–1200. ISSN: 0146-9592.

[49] D. S. Sabatke et al. 'Optimization of retardance for a complete Stokes polarimeter'. In: *Opt. Lett.* 25.11 (June 2000), pp. 802–804. DOI: 10.1364/OL.25.000802.

[50] Chih-Jen Yu, Haw-Min Lin and Kai-Qun Peng. 'Calibration of a simple heterodyne interferometric ellipsometer'. eng. In: *Optics communications* 439 (2019), pp. 244–250. ISSN: 0030-4018.

[51] Randall C. Thompson, Jerold R. Bottiger and Edward S. Fry. 'Measurement of polarized light interactions via the Mueller matrix'. In: *Appl. Opt.* 19.8 (Apr. 1980), pp. 1323–1332. DOI: 10.1364/AO.19.001323.

[52] P. S. Hauge. 'Mueller matrix ellipsometry with imperfect compensators'. eng. In: *Journal of the Optical Society of America (1930)* 68.11 (1978), p. 1519. ISSN: 0030-3941.

[53] Eric Compain, Stéphane Poirier and Bernard Drevillon. 'General and self-consistent method for the calibration of polarization modulators, polarimeters, and Mueller-matrix ellipsometers'. In: *Appl. Opt.* 38.16 (June 1999), pp. 3490–3502. DOI: 10.1364/AO.38.003490.

[54] Fianium Ltd. *WhiteLase SC Series Blue & UV enhanced Supercontinuum Fiber Lasers*. 2021. URL: https://www.forc-photonics.ru/data/files/WhiteLase_SC400_UV_v1(1).pdf.

[55] Frantz Stabo-Eeg et al. 'Design and characterization of achromatic 132° retarders in CaF2 and fused silica'. eng. In: 55.14 (2008), pp. 2203–2214. ISSN: 0950-0340.

[56] Frantz Stabo-Eeg. 'Development of instrumentation for Mueller matrix ellipsometry'. eng. PhD thesis. Trondheim, 2009. ISBN: 9788247114322.

[57] Mikkel Jensen et al. 'Noise of supercontinuum sources in spectral domain optical coherence tomography'. eng. In: *Journal of the Optical Society of America. B, Optical physics* 36.2 (2019), A154–A160. ISSN: 0740-3224.

[58] Silje Skeide Fuglerud et al. 'Feasibility of supercontinuum sources for use in glucose sensing by absorption spectroscopy'. eng. In: (2019). ISSN: 0277-786X. URL: http://hdl.handle.net/11250/2606493.

[59] A. Stenger G. Girod R.Rabenstein. *Signals and Systems*. John Wiley & Sons Ltd, 2001.

[60] Daniel L Carr et al. 'Measuring the Faraday effect in olive oil using permanent magnets and Malus' law'. eng. In: *European journal of physics* 41.2 (2020), p. 25301. ISSN: 0143-0807.

[61] Ronald E. Walpole. *Probability & statistics for engineers and scientists*. eng. 9th ed. Harlow: Pearson Education, 2016. ISBN: 978-1-292-16136-5.

[62] Abubakar I. Adamu et al. 'Noise and spectral stability of deep-UV gas-filled fiber-based supercontinuum sources driven by ultrafast mid-IR pulses'. eng. In: *Scientific reports* 10.1 (2020), pp. 4912–4912. ISSN: 2045-2322.

[63] Shane R. Cloude. 'Conditions For The Physical Realisability Of Matrix Operators In Polarimetry'. In: *Polarization Considerations for Optical Systems II*. Ed. by Russell A. Chipman. Vol. 1166. International Society for Optics and Photonics. SPIE, 1990, pp. 177–187. DOI: 10.1117/12.962889.

[64] Diana M. Hayes. 'Error propagation in decomposition of Mueller matrices'. In: *Polarization: Measurement, Analysis, and Remote Sensing*. Ed. by Dennis H. Goldstein and Russell A. Chipman. Vol. 3121. International Society for Optics and Photonics. SPIE, 1997, pp. 112–123. DOI: 10.1117/12.278963.

[65] S. A.. Borstad. 'Polarimetry using classical polarizing components and nanostructured beam splitting surfaces'. MA thesis. Norges Teknisknaturvitenskaplige Universitet-NTNU, 2018, p. 85.

[66] Dennis H. Goldstein. 'Mueller matrix dual-rotating retarder polarimeter'. eng. In: *Applied Optics* 31.31 (1992), pp. 6676–6683. ISSN: 1559-128X.

[67] J.A. Woolam inc. *RC2*. 2017. URL: https://www.jawoollam.com/download/pdfs/rc2-brochure.pdf.

[68] Nathan J. Pust and Joseph A. Shaw. 'Dual-field imaging polarimeter using liquid crystal variable retarders'. In: *Appl. Opt.* 45.22 (Aug. 2006), pp. 5470–5478. DOI: 10.1364/AO.45.005470.

Appendix A:

Code used for Intensity fit method

```
import numpy as np
import pickle
from sympy.matrices import Matrix, eye, zeros, ones, diag, GramSchmidt
from sympy import *
import matplotlib.pyplot as plt
from scipy.optimize import curve_fit
import lmfit


theta,theta_2, theta_3, theta_4 = symbols('theta theta_2 theta_3 theta_4')
delta, delta_2=symbols('delta delta_2')
a,b,c,d,e,f,g=symbols('a b c d e f g')
e_1,e_2=symbols('e_1 e_2')


Rot=Matrix([[1,0,0,0],[0, cos(2*theta_3),
    ↪  sin(2*theta_3),0],[0,-sin(2*theta_3),cos(2*theta_3),0], [0,0,0,1]])

Neg_Rot=Matrix([[1,0,0,0],[0, cos(2*theta_3),
    ↪  sin(-2*theta_3),0],[0,-sin(-2*theta_3),cos(2*theta_3),0], [0,0,0,1]])

Rot2=Matrix([[1,0,0,0],[0, cos(2*theta),
    ↪  sin(2*theta),0],[0,-sin(2*theta),cos(2*theta),0], [0,0,0,1]])

Neg_Rot2=Matrix([[1,0,0,0],[0, cos(2*theta),
    ↪  sin(-2*theta),0],[0,-sin(-2*theta),cos(2*theta),0], [0,0,0,1]])

Rot3=Matrix([[1,0,0,0],[0, cos(2*theta_2),
    ↪  sin(2*theta_2),0],[0,-sin(2*theta_2),cos(2*theta_2),0], [0,0,0,1]])

Neg_Rot3=Matrix([[1,0,0,0],[0, cos(2*theta_2),
    ↪  sin(-2*theta_2),0],[0,-sin(-2*theta_2),cos(2*theta_2),0], [0,0,0,1]])

Rot4=Matrix([[1,0,0,0],[0, cos(2*theta_4),
    ↪  sin(2*theta_4),0],[0,-sin(2*theta_4),cos(2*theta_4),0], [0,0,0,1]])

Neg_Rot4=Matrix([[1,0,0,0],[0, cos(2*theta_4),
    ↪  sin(-2*theta_4),0],[0,-sin(-2*theta_4),cos(2*theta_4),0], [0,0,0,1]])

Ret= Matrix([[1,0,0,0],
             [0, (cos(2*theta))**2+(sin(2*theta))**2*cos(delta),
              ↪  cos(2*theta)*sin(2*theta)*(1-cos(delta)), sin(2*theta)*sin(delta)],

              ↪  [0,cos(2*theta)*sin(2*theta)*(1-cos(delta)),(sin(2*theta))**2+(cos(2*theta))*
```

```
35              [0,-sin(2*theta)*sin(delta),cos(2*theta)*sin(delta),cos(delta)]])
36
37  Ret_2= Matrix([[1,0,0,0],
38              [0, (cos(2*theta_2))**2+(sin(2*theta_2))**2*cos(delta_2),
                ↪  cos(2*theta_2)*sin(2*theta_2)*(1-cos(delta_2)),
                ↪  sin(2*theta_2)*sin(delta_2)],
39
                ↪  [0,cos(2*theta_2)*sin(2*theta_2)*(1-cos(delta_2)),(sin(2*theta_2))**2+(cos(2*
40
                ↪  [0,-sin(2*theta_2)*sin(delta_2),cos(2*theta_2)*sin(delta_2),cos(delta_2)]])
41  LP= Matrix([[1,-1,0,0],[c, 1, 0, 0],[0,0,b,0], [0,0,0,d]])
42
43  LP_2= Matrix([[1,e,0,0],[-1, 1, 0, 0],[0,0,f,0], [0,0,0,g]])
44
45  S=Matrix([[1],[0],[0],[0]])
46
47  I=Matrix([[1,0,0,0],[0,1,0,0],[0,0,1,0],[0,0,0,1]])
48
49  Out=Matrix([[1],[0],[0],[0]])
50
51  def writematixtofile(Location,matrix):
52      Location='C:/Users/Bruker/Desktop/Masterting/Matrices/' + str(Location)
53      with open(Location, 'wb') as outf:
54          outf.write(pickle.dumps(matrix))
55
56  def readmatixfromfile(Location):
57      Location='C:/Users/Bruker/Desktop/Masterting/Matrices/' + str(Location)
58      with open(Location, 'rb') as inf:
59          test = pickle.loads(inf.read())
60      return test
61
62
63
64  def makeAW():
65      #Makes A and W matrix for the different wavelengths and save them in the correct
        ↪  pickle file
66      Ret=np.loadtxt('C:/Users/Bruker/Desktop/Masterting/Opsett MM/CaF2.txt',
        ↪  usecols=(2,3,4,5,6,7,8,9,10,11,12,13,14,15,16))
67      Ret_2=np.loadtxt('C:/Users/Bruker/Desktop/Masterting/Opsett
        ↪  MM/CaF2_2.txt',usecols=(2,3,4,5,6,7,8,9,10,11,12,13,14,15,16))
68      LP=np.loadtxt('C:/Users/Bruker/Desktop/Masterting/Opsett MM/Polariser_B1.txt',
        ↪  usecols=(2,3,4,5,6,7,8,9,10,11,12,13,14,15,16))
69      LP_2=np.loadtxt('C:/Users/Bruker/Desktop/Masterting/Opsett MM/Polariser_B2.txt',
        ↪  usecols=(3,4,5,6,7,8,9,10,11,12,13,14,15,16,17))
70      Deg=np.loadtxt('C:/Users/Bruker/Desktop/Masterting/Opsett MM/Polariser_B2.txt',
        ↪  usecols=(2))
71      Meas_Deg=np.loadtxt('C:/Users/Bruker/Desktop/Masterting/All
        ↪  wavelengths/testing2.txt',max_rows=1)
72
73      Ret=np.delete(Ret, [0,1,2,3,4,5,6,7,8,9,10,11,-1,-2,-3],0)
74      Ret_2=np.delete(Ret_2, [0,1,2,3,4,5,6,7,8,9,10,11,-1,-2,-3],0)
```

```
75      LP=np.delete(LP, [0,1,2,3,4,5,6,7,8,9,10,11,-1,-2,-3],0)
76
77      Rot=Matrix([[1,0,0,0],[0, cos(2*theta_3),
        ↪  sin(2*theta_3),0],[0,-sin(2*theta_3),cos(2*theta_3),0], [0,0,0,1]])
78
79      Neg_Rot=Matrix([[1,0,0,0],[0, cos(2*theta_3),
        ↪  sin(-2*theta_3),0],[0,-sin(-2*theta_3),cos(2*theta_3),0], [0,0,0,1]])
80
81      Rot=lambdify(theta_3,Rot, "numpy")
82      Neg_Rot=lambdify(theta_3,Neg_Rot, "numpy")
83
84      Rot=Matrix(Rot(0.11301712))
85      Neg_Rot=Matrix(Neg_Rot(0.11301712))
86
87      ang=np.array([-51.7,-15.1,15.1,51.7])/180*np.pi-0.00537283
88      ang2=np.array([-51.7,-15.1,15.1,51.7])/180*np.pi+0.00255963
89      for degree in Meas_Deg:
90          i, = np.where(np.isclose(Deg, degree))
91          i=int(i)
92          OE1=Matrix(np.reshape(np.concatenate(([1.0], LP[i,:])),(4,4)))
93          OE2=Matrix(np.reshape(np.concatenate(([1.0], Ret[i,:])),(4,4)))
94          OE3=Matrix(np.reshape(np.concatenate(([1.0], Ret_2[i,:])),(4,4)))
95          OE4=Matrix(np.reshape(np.concatenate(([1.0], LP_2[i,:])),(4,4)))
96
97          W=Neg_Rot2*OE2*Rot2*OE1*S
98          W=lambdify(theta,W[:], "numpy")
99          W=Matrix(W(ang2))
100         print(W)
101
102
103         A=transpose(S)*Neg_Rot*OE4*Rot*Neg_Rot3*OE3*Rot3
104
105         A=lambdify(theta_2,A[:], "numpy")
106         A=transpose(Matrix(A(ang)))
107
108         writematixtofile('A/'+str(degree)+'.pickle', A)
109         writematixtofile('W/'+str(degree)+'.pickle', W)
110
111 def loadandarrangeB(i, path):
112     #Load text file with the intensity matrix and arrange it correctly
113     B=np.loadtxt(path, usecols=i)
114     B=B[1:]
115     A=np.zeros((4,4))
116     PSG=[1,1,2,2,3,3,3,2,1,0,0,0,0,1,2,3]
117     PSA=[1,2,2,1,1,2,3,3,3,3,2,1,0,0,0,0]
118     for j in range(len(B)):
119         A[PSA[j],PSG[j]]=B[j]
120     return Matrix(A)
121
122 def findMMandsave(load_path, save_path):
123     #Finner Muellermatrisa tilsvarende målingene tatt
```

```
    Meas_Deg=np.loadtxt(load_path,max_rows=1)
    i=0
    for degree in Meas_Deg:
        A=readmatixfromfile('A/'+str(degree)+'.pickle')
        G=readmatixfromfile('W/'+str(degree)+'.pickle')
        B=loadandarrangeB(i, load_path)
        A_inv=Matrix(np.linalg.pinv(np.array(A).astype(np.float64)))
        G_inv=Matrix(np.linalg.pinv(np.array(G).astype(np.float64)))
        M=np.array(A_inv*B*G_inv).astype(np.float64)
        M=np.reshape(M,16)
        np.savetxt(str(save_path) + str(degree)+'.txt', [M])
        i+=1

def plottM(load_path, load_path_MM, save_path):
    #Plotter matrisene

    ↪ M_11,M_12,M_13,M_14,M_21,M_22,M_23,M_24,M_31,M_32,M_33,M_34,M_41,M_42,M_43,M_44=[],[],
    Meas_Deg=np.loadtxt(load_path,max_rows=1)
    for degree in Meas_Deg:
        MM=np.loadtxt(str(load_path_MM) + str(degree)+'.txt')

        ↪ M_11.append(MM[0]),M_12.append(MM[1]),M_13.append(MM[2]),M_14.append(MM[3]),M_21.a

    ↪ M_11,M_12,M_13,M_14,M_21,M_22,M_23,M_24,M_31,M_32,M_33,M_34,M_41,M_42,M_43,M_44=np.arr

    ↪ M_11,M_12,M_13,M_14,M_21,M_22,M_23,M_24,M_31,M_32,M_33,M_34,M_41,M_42,M_43,M_44=M_11/M
    fig, ((ax1, ax2, ax3, ax4), (ax5, ax6, ax7, ax8),(ax9, ax10, ax11, ax12),(ax13,
    ↪ ax14, ax15, ax16)) = plt.subplots(4, 4, figsize=(12,10))

    ax1.plot(Meas_Deg,M_11, label='M_11')
    ax1.legend()

    ax2.plot(Meas_Deg,M_12, label='M_12')
    ax2.legend()

    ax3.plot(Meas_Deg,M_13, label='M_13')
    ax3.legend()

    ax4.plot(Meas_Deg,M_14, label='M_14')
    ax4.legend()

    ax5.plot(Meas_Deg,M_21, label='M_21')
    ax5.legend()

    ax6.plot(Meas_Deg,M_22, label='M_22')
    ax6.legend()

    ax7.plot(Meas_Deg,M_23, label='M_23')
    ax7.legend()

    ax8.plot(Meas_Deg,M_24, label='M_24')
```

```
    ax8.legend()

    ax9.plot(Meas_Deg,M_31, label='M_31')
    ax9.legend()

    ax10.plot(Meas_Deg,M_32, label='M_32')
    ax10.legend()

    ax11.plot(Meas_Deg,M_33, label='M_33')
    ax11.legend()

    ax12.plot(Meas_Deg,M_34, label='M_34')
    ax12.legend()

    ax13.plot(Meas_Deg,M_41, label='M_41')
    ax13.set_xlabel('Wavelength [nm]')
    ax13.legend()

    ax14.plot(Meas_Deg,M_42, label='M_42')
    ax14.set_xlabel('Wavelength [nm]')
    ax14.legend()

    ax15.plot(Meas_Deg,M_43, label='M_43')
    ax15.set_xlabel('Wavelength [nm]')
    ax15.legend()

    ax16.plot(Meas_Deg,M_44, label='M_44')
    ax16.set_xlabel('Wavelength [nm]')
    ax16.legend()
    fig.savefig(r'C:\Users\Bruker\Desktop\MM.png',bbox_inches='tight', dpi=250)

def MakebaseAW():

    A=transpose(Out)*Neg_Rot*LP_2*Rot*Ret_2
    G=Ret*Neg_Rot4*LP*Rot4*S
    W=A*G
    writematixtofile('A/A.pickle', A)
    writematixtofile('W/W.pickle', G)
    writematixtofile('I/I.pickle', W)

def Calibration():
    #Callibrates the the sample
    Int=readmatixfromfile('I/I.pickle')
    Int=Int[0,0]
    Int=Int.subs(theta, theta-e_1)
    Int=Int.subs(theta_2, theta_2-e_2)
    Int=a*Int
    I=lambdify(list(Int.free_symbols), Int)
    List=[]


```

```
221
222     t,t_2=np.loadtxt(r'C:\Users\Bruker\Desktop\Masterting\All
        ↪  wavelengths\calib_degrees7.txt', unpack=True)
223     Meas_Deg=np.loadtxt(r'C:\Users\Bruker\Desktop\Masterting\All
        ↪  wavelengths\calib7.txt', max_rows=1)
224     t=t/180*np.pi
225     t_2=t_2/180*np.pi
226
227
228     param_values = dict(e_2=0, theta_4=0, delta=128/180*np.pi, e=1, a=0.81,
        ↪  theta_3=0, c=-1, e_1=0, theta=t, theta_2=t_2, delta_2=128/180*np.pi)
229
230     for i in range(len(Meas_Deg)):
231         D=np.loadtxt(r'C:\Users\Bruker\Desktop\Masterting\All
            ↪  wavelengths\calib7.txt', skiprows=1, usecols=i)
232         mod=lmfit.Model(I,independent_vars=['theta', 'theta_2'])
233         mod=mod.fit(data=-D, **param_values)
234         o=[]
235         for name, param in mod.params.items():
236             f=param.value
237             o.append(f)
238         List.append(o)
239
        ↪  np.savetxt(r'C:\Users\Bruker\Desktop\Masterting\Matrices\Coefficients\Coeff.txt',
        ↪  List)
240
241 def makeAWnew():
242     A=readmatixfromfile('A/A.pickle')
243     W=readmatixfromfile('W/W.pickle')
244     One=np.ones(4)
245     A=lambdify((e,delta_2,theta_2,theta_3), A[:], 'numpy')
246     W=lambdify((c,delta,theta,theta_4), W[:], 'numpy')
247     Meas_Deg=np.loadtxt(r'C:\Users\Bruker\Desktop\Masterting\All
        ↪  wavelengths\calib7.txt', max_rows=1)
248     for i in range(len(Meas_Deg)):
249
            ↪  L=np.loadtxt(r'C:\Users\Bruker\Desktop\Masterting\Matrices\Coefficients\Coeff.txt'
250         #må dele opp L manuelt etter rekkefølgen definert i calibration
251         ang=np.array([-51.7,-15.1,15.1,51.7])/180*np.pi-L[7]
252         ang2=np.array([-51.7,-15.1,15.1,51.7])/180*np.pi-L[0]
253         N=A(L[3],L[8], ang, L[5])
254         N[0]=One
255         N=np.transpose(np.array(N))
256
257         P=W(L[6],L[2], ang2, L[1])
258         P[0]=One
259         P=np.array(P)
260         writematixtofile('A/'+str(Meas_Deg[i])+'.pickle', N)
261         writematixtofile('W/'+str(Meas_Deg[i])+'.pickle', P)
262
263
```

```
264 def main(data_path, matrix_location,figure_location):
265     findMMandsave(data_path,matrix_location)
266     plottM(data_path, matrix_location,figure_location)
267
268
269
270
271
272
273
274
275
276
277
278
279
280
281
282
283
284
285
286
287
288
289
290
291
292
293
294
295
296
297
298
```

Appendix B:

Results from Unsuccessful Calibration using the Intensity Fit Method

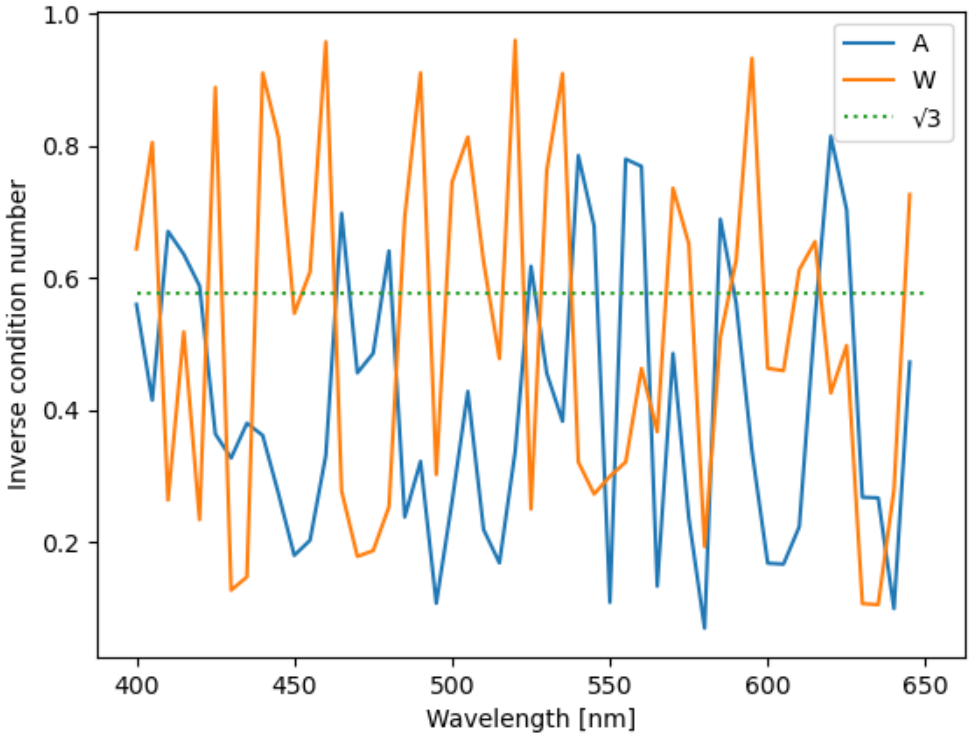

Figure 33: Inverse condition numbers of **A** and **W** obtained using the intensity fit method.

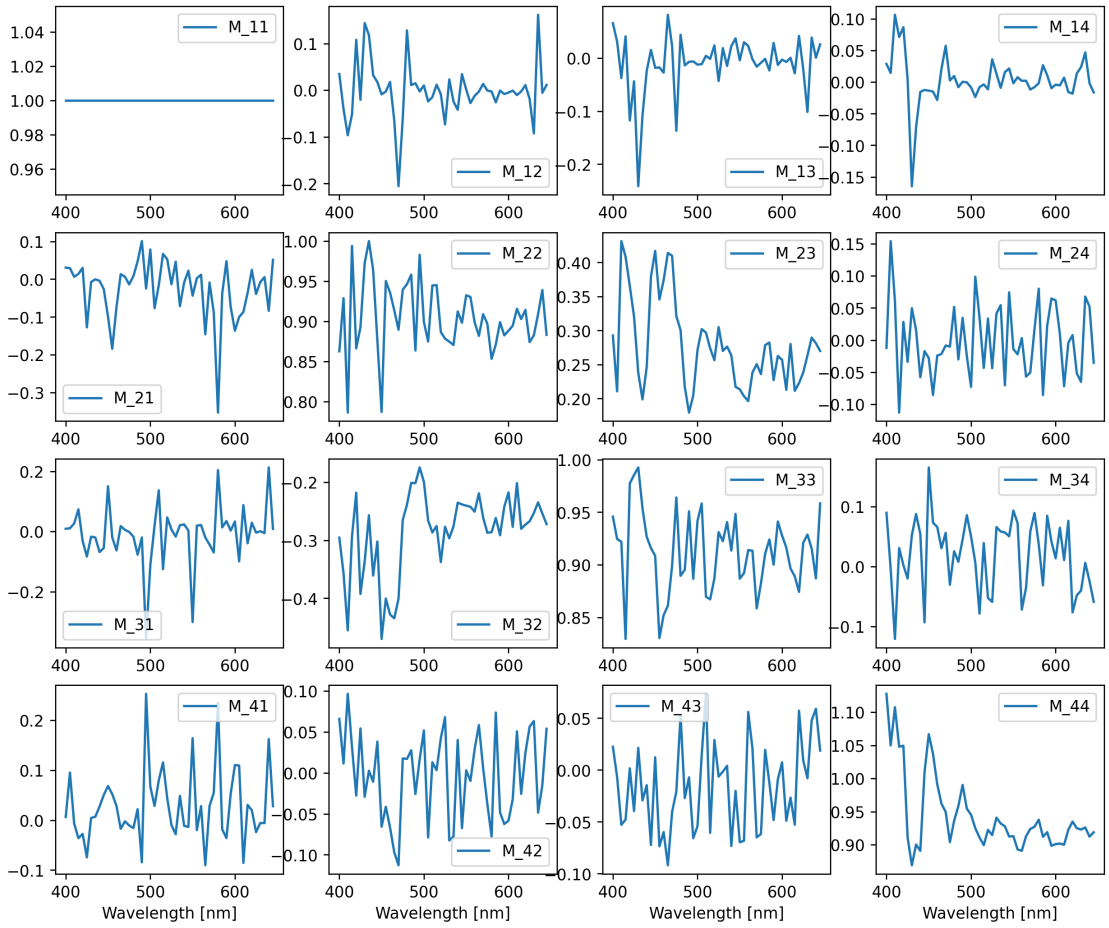

Figure 34: Measured Mueller matrix of air using the intensity fit calibration.

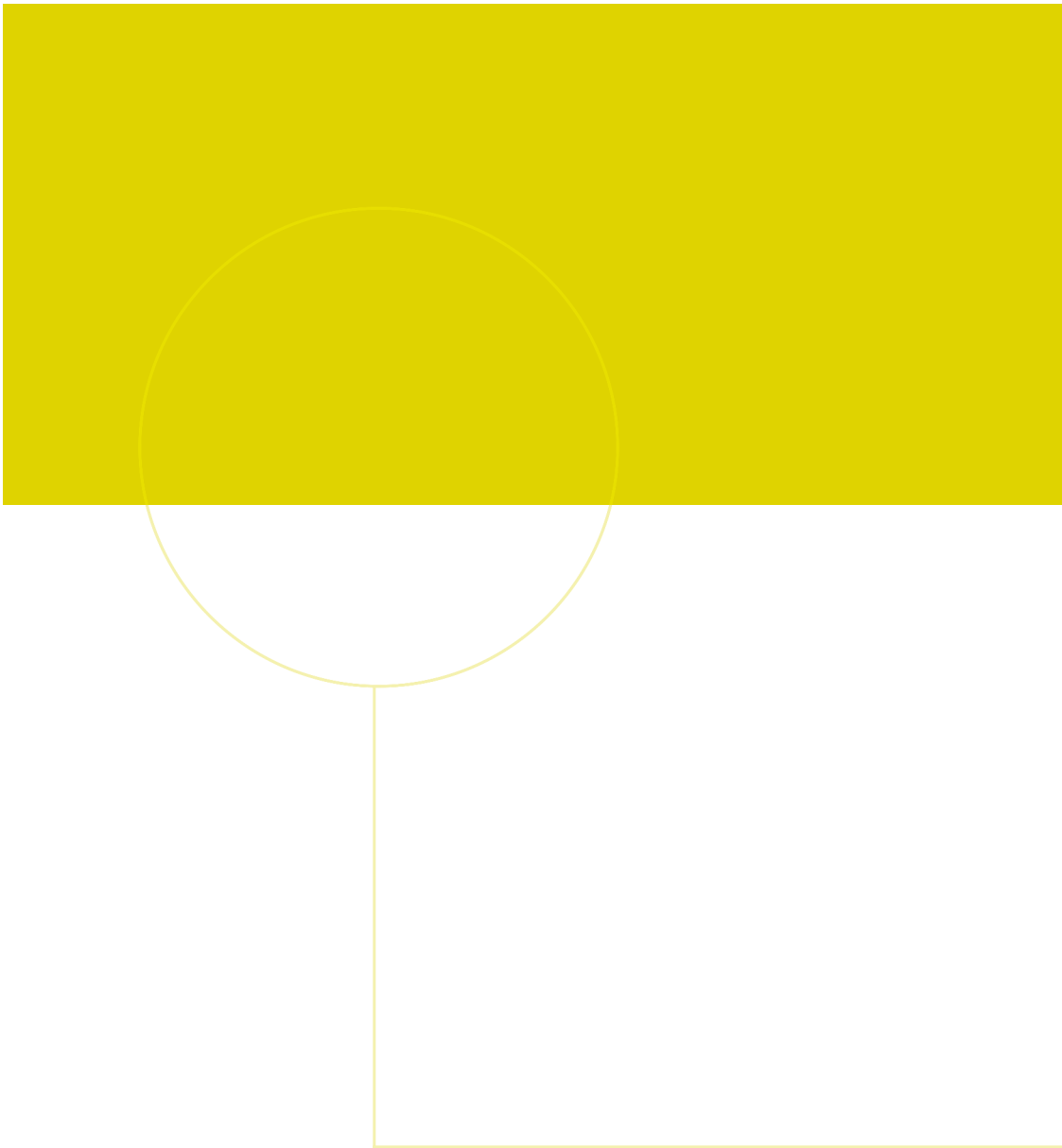

NTNU

Norwegian University of
Science and Technology